NEUTRON SCATTERING - MAGNETIC AND QUANTUM PHENOMENA

Edited by
FELIX FERNANDEZ-ALONSO
DAVID L. PRICE

VOLUME 48
EXPERIMENTAL METHODS IN THE PHYSICAL SCIENCES

Treatise Editors
THOMAS LUCATORTO
KENNETH BALDWIN
JOHN T. YATES

Experimental Methods in the Physical Sciences

Volume 48

Neutron Scattering - Magnetic and Quantum Phenomena

Experimental Methods in the Physical Sciences

Thomas Lucatorto, John T. Yates,
and Kenneth Baldwin
Editors in Chief

Experimental Methods in the Physical Sciences

Volume 48

Neutron Scattering - Magnetic and Quantum Phenomena

Edited by

Felix Fernandez-Alonso
ISIS Facility
Rutherford Appleton Laboratory
Chilton, Didcot, Oxfordshire
United Kingdom

and

Department of Physics and Astronomy
University College London
London
United Kingdom

David L. Price
Synchrotron Radiation and Neutron Research Group, CEMHTI
Centre National de la Recherche Scientifique
Orléans
France

ELSEVIER

AMSTERDAM • BOSTON • HEIDELBERG • LONDON
NEW YORK • OXFORD • PARIS • SAN DIEGO
SAN FRANCISCO • SINGAPORE • SYDNEY • TOKYO

Academic Press is an imprint of Elsevier

Academic Press is an imprint of Elsevier
125 London Wall, London EC2Y 5AS, UK
525 B Street, Suite 1800, San Diego, CA 92101-4495, USA
225 Wyman Street, Waltham, MA 02451, USA
The Boulevard, Langford Lane, Kidlington, Oxford OX5 1GB, UK

Notices

Knowledge and best practice in this field are constantly changing. As new research and experience broaden our understanding, changes in research methods, professional practices, or medical treatment may become necessary.

Practitioners and researchers must always rely on their own experience and knowledge in evaluating and using any information, methods, compounds, or experiments described herein. In using such information or methods they should be mindful of their own safety and the safety of others, including parties for whom they have a professional responsibility.

To the fullest extent of the law, neither the Publisher nor the authors, contributors, or editors, assume any liability for any injury and/or damage to persons or property as a matter of products liability, negligence or otherwise, or from any use or operation of any methods, products, instructions, or ideas contained in the material herein.

ISBN: 978-0-12-802049-4
ISSN: 1079-4042

Contents

5. Multiferroics

William D. Ratcliff II, Jeffrey W. Lynn

6. Neutron Scattering in Nanomagnetism

Boris P. Toperverg, Hartmut Zabel

This page intentionally left blank

List of Contributors

Bryan C. Chakoumakos, Quantum Condensed Matter Division, Oak Ridge National Laboratory, Oak Ridge, Tennessee, USA

Pengcheng Dai, Department of Physics and Astronomy, Rice University, Houston, Texas, USA

Bela Farago, Institut Laue-Langevin, Grenoble, France

V. Ovidiu Garlea, Quantum Condensed Matter Division, Oak Ridge National Laboratory, Oak Ridge, Tennessee, USA

Bruce D. Gaulin, Department of Physics and Astronomy, McMaster University, Hamilton, Ontario, Canada; Canadian Institute for Advanced Research, Toronto, Ontario, Canada; Brockhouse Institute for Materials Research, McMaster University, Hamilton, Ontario, Canada

Sara Haravifard, Department of Physics, Duke University, Durham, North Carolina, USA; The James Franck Institute and Department of Physics, The University of Chicago, Chicago, Illinois, USA; Advanced Photon Source, Argonne National Laboratory, Argonne, Illinois, USA

Jeffrey W. Lynn, NIST Center for Neutron Research, National Institute of Standards and Technology, Gaithersburg, Maryland, USA

Janos Major, Max-Planck-Institut für Metallforschung, Stuttgart, Germany

Ferenc Mezei, European Spallation Source ERIC, Lund, Sweden; HAS Wigner Research Center, Budapest, Hungary

William D. Ratcliff II, NIST Center for Neutron Research, National Institute of Standards and Technology, Gaithersburg, Maryland, USA

Konrad Siemensmeyer, Helmholtz Zentrum Berlin, Berlin, Germany

Yu Song, Department of Physics and Astronomy, Rice University, Houston, Texas, USA

Michael Steiner, Helmholtz Zentrum Berlin, Berlin, Germany

Boris P. Toperverg, Institute for Experimental Condensed Matter Physics, Ruhr-University Bochum, Bochum, Germany; Petersburg Nuclear Physics Institute, St Petersburg, Russia

Zahra Yamani, Canadian Neutron Beam Centre, Chalk River Laboratories, Chalk River, Ontario, Canada

Hartmut Zabel, Institute for Experimental Condensed Matter Physics, Ruhr-University Bochum, Bochum, Germany; Johannes Gutenberg-Universität Mainz, Mainz, Germany

This page intentionally left blank

Volumes in Series

Experimental Methods in the Physical Sciences (Formerly Methods of Experimental Physics)

Volume 1. Classical Methods
Edited by lmmanuel Estermann

Volume 2. Electronic Methods, Second Edition (in two parts)
Edited by E. Bleuler and R. O. Haxby

Volume 3. Molecular Physics, Second Edition (in two parts)
Edited by Dudley Williams

Volume 4. Atomic and Electron Physics - Part A: Atomic Sources and Detectors; Part B: Free Atoms
Edited by Vernon W. Hughes and Howard L. Schultz

Volume 5. Nuclear Physics (in two parts)
Edited by Luke C. L. Yuan and Chien-Shiung Wu

Volume 6. Solid State Physics - Part A: Preparation, Structure, Mechanical and Thermal Properties; Part B: Electrical, Magnetic and Optical Properties
Edited by K. Lark-Horovitz and Vivian A. Johnson

Volume 7. Atomic and Electron Physics - Atomic Interactions (in two parts)
Edited by Benjamin Bederson and Wade L. Fite

Volume 8. Problems and Solutions for Students
Edited by L. Marton and W. F. Hornyak

Volume 9. Plasma Physics (in two parts)
Edited by Hans R. Griem and Ralph H. Lovberg

Volume 10. Physical Principles of Far-Infrared Radiation
Edited by L. C. Robinson

Volume 11. Solid State Physics
Edited by R. V. Coleman

Volume 12. Astrophysics - Part A: Optical and Infrared Astronomy
Edited by N. Carleton
Part B: Radio Telescopes; Part C: Radio Observations
Edited by M. L. Meeks

Volume 13. Spectroscopy (in two parts)
Edited by Dudley Williams

Volume 14. Vacuum Physics and Technology
Edited by G. L. Weissler and R. W. Carlson

Volume 15. Quantum Electronics (in two parts)
Edited by C. L. Tang

Volume 16. Polymers - Part A: Molecular Structure and Dynamics; Part B: Crystal Structure and Morphology; Part C: Physical Properties
Edited by R. A. Fava

Volume 17. Accelerators in Atomic Physics
Edited by P. Richard

Volume 18. Fluid Dynamics (in two parts)
Edited by R. J. Emrich

Volume 19. Ultrasonics
Edited by Peter D. Edmonds

Volume 20. Biophysics
Edited by Gerald Ehrenstein and Harold Lecar

Volume 21. Solid State Physics: Nuclear Methods
Edited by J. N. Mundy, S. J. Rothman, M. J. Fluss, and L. C. Smedskjaer

Volume 22. Solid State Physics: Surfaces
Edited by Robert L. Park and Max G. Lagally

Volume 23. Neutron Scattering (in three parts)
Edited by K. Skold and D. L. Price

Volume 24. Geophysics - Part A: Laboratory Measurements; Part B: Field Measurements
Edited by C. G. Sammis and T. L. Henyey

Volume 25. Geometrical and Instrumental Optics
Edited by Daniel Malacara

Volume 26. Physical Optics and Light Measurements
Edited by Daniel Malacara

Volume 27. Scanning Tunneling Microscopy
Edited by Joseph Stroscio and William Kaiser

Volume 28. Statistical Methods for Physical Science
Edited by John L. Stanford and Stephen B. Vardaman

Volume 29. Atomic, Molecular, and Optical Physics - Part A: Charged Particles; Part B: Atoms and Molecules; Part C: Electromagnetic Radiation
Edited by F. B. Dunning and Randall G. Hulet

Volume 30. Laser Ablation and Desorption
Edited by John C. Miller and Richard F. Haglund, Jr.

Volume 31. Vacuum Ultraviolet Spectroscopy I
Edited by J. A. R. Samson and D. L. Ederer

Volume 32. Vacuum Ultraviolet Spectroscopy II
Edited by J. A. R. Samson and D. L. Ederer

Volume 33. Cumulative Author lndex and Tables of Contents, Volumes 1-32

Volume 34. Cumulative Subject lndex

Volume 35. Methods in the Physics of Porous Media
Edited by Po-zen Wong

Volume 36. Magnetic Imaging and its Applications to Materials
Edited by Marc De Graef and Yimei Zhu

Volume 37. Characterization of Amorphous and Crystalline Rough Surface: Principles and Applications
Edited by Yi Ping Zhao, Gwo-Ching Wang, and Toh-Ming Lu

Volume 38. Advances in Surface Science
Edited by Hari Singh Nalwa

Volume 39. Modern Acoustical Techniques for the Measurement of Mechanical Properties
Edited by Moises Levy, Henry E. Bass, and Richard Stern

Volume 40. Cavity-Enhanced Spectroscopies
Edited by Roger D. van Zee and J. Patrick Looney

Volume 41. Optical Radiometry
Edited by A. C. Parr, R. U. Datla, and J. L. Gardner

Volume 42. Radiometric Temperature Measurements. I. Fundamentals
Edited by Z. M. Zhang, B. K. Tsai, and G. Machin

Volume 43. Radiometric Temperature Measurements. II. Applications
Edited by Z. M. Zhang, B. K. Tsai, and G. Machin

Volume 44. Neutron Scattering − Fundamentals
Edited by Felix Fernandez-Alonso and David L. Price

Volume 45. Single-Photon Generation and Detection
Edited by Alan Migdall, Sergey Polyakov, Jingyun Fan, and Joshua Bienfang

Volume 46. Spectrophotometry: Accurate Measurement of Optical Properties of Materials
Edited by Thomas A. Germer, Joanne C. Zwinkels, and Benjamin K. Tsai

Volume 47. Optical Radiometry for Ocean Climate Measurements
Edited by Giuseppe Zibordi, Craig J. Donlon, and Albert C. Parr

Volume 48. Neutron Scattering - Magnetic and Quantum Phenomena
Edited by Felix Fernandez-Alonso and David L. Price

Preface

Just over 80 years ago, a brief letter from James Chadwick to *Nature* [1,2] presented conclusive experimental evidence unveiling the existence of a neutral particle (nearly) isobaric with the proton. The discovery of the henceforth-to-be-known-as "neutron" had profound consequences for both scientific research and the destiny of humankind, as it led to the unleashing of the might of nuclear power in less than a decade [3].

The first use of these "neutral protons" to probe the microscopic underpinnings of the material world around us also dates back to those early years, with pioneering neutron-diffraction experiments at Oak Ridge National Laboratory (USA) in the mid-1940s, and the subsequent development of neutron spectroscopy at Chalk River (Canada) in the 1950s. Since then, neutron-scattering techniques have matured into a robust and increasingly versatile toolkit for physicists, chemists, biologists, materials scientists, engineers, or technologists. At the turn of the last century, the 1994 Nobel Prize in Physics awarded to C.G. Shull and B.N. Brockhouse recognized their ground-breaking efforts toward the development and consolidation of neutron science as a discipline in its own right [4]. This milestone also served to define neutron scattering as the technique *par excellence* to investigate *where atoms are* (structure) and *what atoms do* (dynamics), a popular motto across generations of neutron-scattering practitioners.

Sustained and continued developments in experimental methods over the past few decades have greatly increased the sensitivity and range of applications of neutron scattering. While early measurements probed distances on the order of interatomic spacings (fractions of a nanometer) and characteristic times associated with lattice vibrations (picoseconds), contemporary neutron-scattering experiments can cover length scales from less than 0.01 to 1000s of nanometers, and time scales from the attosecond to the microsecond. These advances have been made possible via a significant expansion of the range of neutron energies available to the experimenter, from micro-electron-volts (particularly at cold sources in research reactors) to hundreds of electron-volts (at pulsed spallation sources), as well as by unabated progress in the implementation of a variety of novel and ingenious ideas such as position- and polarization-sensitive detection or back-scattering and spin-labeling methods. As a result, neutron science has grown beyond traditional research areas, from the conventional determination of crystal structures and lattice dynamics of half-a-century ago (not to forget their magnetic analogs), to high-resolution

structural studies of disordered thin films, liquid interfaces, biological structures, macromolecular and supramolecular architectures and devices, or the unraveling of the dynamics and energy-level structure of complex molecular solids, nanostructured materials and surfaces, or magnetic clusters and novel superconductors. Along with these scientific and technical developments, the community of neutron scientists has also expanded and diversified beyond recognition. Whereas the early stages of neutron scattering had its roots in condensed-matter physics and crystallography, present-day users of central neutron-scattering facilities include chemists, biologists, ceramicists, and metallurgists, to name a few, as well as physicists with an increasingly diverse range of transdisciplinary interests, from the foundations of quantum mechanics to soft matter, food science, biology, geology, or archeometry.

This book series seeks to cover in some detail the production and use of neutrons across the aforementioned disciplines, with a particular emphasis on technical and scientific developments over the past two decades. As such, it necessarily builds upon an earlier and very successful three-volume set edited by K. Sköld and D.L. Price, published in the 1980s by *Academic Press* as part of *Methods of Experimental Physics* (currently *Experimental Methods in the Physical Sciences*). Furthermore, with the third-generation spallation sources recently constructed in the US and Japan, or in the advanced construction or planning stage in China and Europe, there has been an increasing interest in time-of-flight and broadband neutron-scattering techniques. Correspondingly, the improved performance of cold moderators at both reactors and spallation sources has extended long-wavelength capabilities to such an extent that a sharp distinction between fission- and accelerator-driven neutron sources may no longer be of relevance to the future of the discipline.

On a more practical front, the chapters that follow are meant to enable you to identify aspects of your work in which neutron-scattering techniques might contribute, conceive the important experiments to be done, assess what is required to carry them out, write a successful proposal to a user facility, and perform these experiments under the guidance and support of the appropriate facility-based scientist. The presentation is aimed at professionals at all levels, from early career researchers to mature scientists who may be insufficiently aware or up-to-date with the breadth of opportunities provided by neutron techniques in their area of specialty. In this spirit, it does not aim to present a systematic and detailed development of the underlying theory, which may be found in superbly written texts such as those of Lovesey [5] or Squires [6]. Likewise, it is not a detailed hands-on manual of experimental methods, which in our opinion is best obtained directly from experienced practitioners or, alternatively, by attending practical training courses at the neutron facilities. As an intermediate (and highly advisable) step, we also note the existence of neutron-focused thematic schools, particularly those at Grenoble [7] and Oxford [8], both of which have been running on a regular basis since the 1990s. With these primary objectives in mind, each chapter focuses on

well-defined areas of neutron science and has been written by a leading practitioner or practitioners of the application of neutron methods in that particular field.

In the previous volume, *Neutron Scattering − Fundamentals* [9], we gave a self-contained survey of the theoretical concepts and formalism of the technique and established the notation used throughout the series. Subsequent chapters reviewed neutron production and instrumentation, respectively, areas which have profited enormously from recent developments in accelerator physics, materials research and engineering, or computing, to name a few. The remaining chapters treated several basic applications of neutron scattering including the structure of complex materials, large-scale structures, and dynamics of atoms and molecules. The appendix went back to some requisite fundamentals linked to neutron−matter interactions, along with a detailed compilation of neutron scattering lengths and cross sections across the periodic table.

The present volume is dedicated to the applications of neutron scattering techniques to magnetic and quantum phenomena. The first chapter deals with neutron optics and spin-labeling methods and also gives a broad introduction to the interaction of neutrons with electronic spins in condensed matter. The following chapters discuss recent developments in the use of neutron scattering to investigate quantum phase transitions, high-temperature superconductors, magnetic structures, multiferroics, nanomagnetism, and nuclear magnetism. A third volume will cover applications in biology, chemistry, and materials science.

In closing this preface, we wish to thank all authors for taking time out of their busy schedules to be part of this venture, Drs T. Lucatorto, A.C. Parr, and K. Baldwin for inviting us to undertake this work, and the staff of *Academic Press* for their encouragement, diligence, and forbearance along the way.

Felix Fernandez-Alonso
David L. Price

REFERENCES

[1] J. Chadwick, Nature 129 (1932) 312.
[2] URL: www.nobelprize.org/nobel_prizes/physics/laureates/1935/ (last accessed on 12.08.15).
[3] A. MacKay, The Making of the Atomic Age, Oxford University Press, Oxford, 1984.
[4] URL: www.nobelprize.org/nobel_prizes/physics/laureates/1994/ (last accessed on 12.08.15).
[5] S.W. Lovesey, Theory of Neutron Scattering from Condensed Matter, vols. I and II, Oxford University Press, Oxford, 1986.
[6] G.L. Squires, Introduction to the Theory of Thermal Neutron Scattering, third ed., Cambridge University Press, Cambridge, 2012.
[7] URL: hercules-school.eu/ (last accessed on 12.08.15).
[8] URL: www.oxfordneutronschool.org/ (last accessed on 12.08.15).
[9] F. Fernandez-Alonso, D.L. Price (Eds.), Neutron Scattering − Fundamentals, Experimental Methods in the Physical Sciences, vol. 44, Academic Press, Amsterdam, 2013.

This page intentionally left blank

Eulogy

Janos Major

During the preparation of this book, we were saddened by the news of the premature death of Janos Major, a prominent member of the neutron scattering community and coauthor of the first chapter of this volume.

Janos spent the majority of his career in the Max Planck Institute in Stuttgart, working with Directors Alfred Seeger and then Helmut Dosch. Janos organized essentially all the neutron works in the Dosch department with a focus on the original development of the SERGIS concept together with Gian Felcher and Roger Pynn. This instrument approach exploits neutron spin echo for encoding the momentum transfer of neutrons.

Janos was a wonderful person and an exquisite scientist. Those who worked with him enjoyed his spirited experimental and technical skills, his dedication to science, and his steadfast loyalty to his colleagues and students.

Helmut Dosch
Felix Fernandez-Alonso
David L. Price

This page intentionally left blank

Symbols

Note: Other symbols may be used that are unique to the chapter where they occur.

a	Scattering length in center-of-mass frame
b	Bound scattering length
A	Atomic mass (or nucleon) number
$\overline{b}$	Coherent scattering length
b^+	Scattering length for $I + \frac{1}{2}$ state
b^-	Scattering length for $I - \frac{1}{2}$ state
b_i	Incoherent scattering length
b_N	Spin-dependent scattering length
c	Speed of light in vacuum = 299792458 m s^{-1} [1]
$\mathbf{D}$	Dynamical matrix
$\mathbf{D}_\perp(\mathbf{Q})$	Magnetic interaction operator
d	Mass density
$\mathbf{d}$	Equilibrium position of atom in unit cell
$\mathrm{d}\sigma/\mathrm{d}\Omega$	Differential scattering cross section
$\mathrm{d}^2\sigma/\mathrm{d}\Omega\ \mathrm{d}E_\mathrm{f}$	Double differential scattering cross section
E	Neutron energy transfer ($E_\mathrm{i} - E_\mathrm{f}$)
E_n	Neutron energy
E_i,E_f	Initial, final (scattered) neutron energy
e	Elementary charge = 1.602176565 × 10^{-19} C
$\mathbf{e}^k(\mathbf{q})$	Polarization vector of normal mode k [$\mathbf{e}_d^k(\mathbf{q})$ for a non-Bravais crystal]
$F(\boldsymbol{\tau})$	Unit cell structure factor
f	Force constant
$f(\mathbf{Q})$	Form factor
$G(\mathbf{r},t)$	Space−time (van Hove) correlation function [$G_\mathrm{d}(\mathbf{r},t) + G_\mathrm{s}(\mathbf{r},t)$]
$G_\mathrm{d}(\mathbf{r},t)$	"Distinct" space−time correlation function
$G_\mathrm{s}(\mathbf{r},t)$	"Self" space−time correlation function
$g(\mathbf{r})$	Pair distribution function
g_e	Electron g factor = −2.00231930436153
g_n	Neutron g factor = −3.82608545
h	Planck constant = 6.62606957 × 10^{-34} J s
$\hbar$	Planck constant over 2π ($h/2\pi$) = 1.054571726 × 10^{-34} J s
$\mathbf{I}$	Angular momentum operator for nucleus
$I(\mathbf{Q},t)$	Intermediate scattering function
$I_\mathrm{s}(\mathbf{Q},t)$	Self intermediate scattering function
k_B	Boltzmann constant = 1.3806488 × 10^{-23} J K^{-1}
$\mathbf{k}_\mathrm{i}$,$\mathbf{k}_\mathrm{f}$	Initial, final (scattered) neutron wave vector
$\mathbf{k}_\mathrm{n}$	Neutron wave vector ($\mathbf{k}_\mathrm{n} = 2\pi/\lambda_\mathrm{n}$)

L_i,L_f	Initial (primary), final (secondary) flight path
$\mathbf{l}$	Unit cell position vector (lowercase "L")
M	Atom mass
$\mathbf{M}$	Magnetization operator
m_e	Electron mass = $9.10938291 \times 10^{-31}$ kg
m_n	Neutron mass = $1.674927351 \times 10^{-27}$ kg
m_p	Proton mass = $1.672621777 \times 10^{-27}$ kg
N	Number of atoms in sample
N_A	Avogadro constant = $6.02214129 \times 10^{23}$ mol^{-1}
N_c	Number of unit cells in crystal
$\mathbf{R}_j$	Position vector for particle j
$\mathbf{Q}$	Scattering vector ($\mathbf{k}_\mathrm{i} - \mathbf{k}_\mathrm{f}$)
$\mathbf{q}$	Reduced wave vector ($\mathbf{Q} - \boldsymbol{\tau}$)
r_0	Classical electron radius $(e^2/4\pi\varepsilon_0 m_\mathrm{e} c^2) = 2.8179403267 \times 10^{-15}$ m
$\mathbf{S}$	Atomic spin operator
$S(\mathbf{Q})$	Static structure factor $I(\mathbf{Q},0)$
$S(\mathbf{Q},E)$	Dynamic structure factor or scattering function
$S_\mathrm{c}(\mathbf{Q},E)$	Coherent dynamic structure factor or scattering function
$S_\mathrm{i}(\mathbf{Q},E)$	Incoherent dynamic structure factor or scattering function
$\mathbf{s}$	Electron spin operator
T	Temperature
u	Unified atomic mass unit = $1.660538921 \times 10^{-27}$ kg
$\mathbf{u}^l$	Vibrational amplitude ($\mathbf{u}_d^l$ for non-Bravais crystals)
V	Volume of sample
v_i,v_f	Initial, final (scattered) neutron velocity
v_n	Neutron velocity
v_0	Unit cell volume
$2W$	Exponential argument in the Debye−Waller factor
Z	Atomic (or proton) number
$Z(E)$	Phonon density of states
Γ	Spectral linewidth
γ	Neutron magnetic moment to nuclear magneton ratio ($\mu_\mathrm{n}/\mu_\mathrm{N}$) = -1.91304272
γ_n	Neutron gyromagnetic ratio = 1.83247179×10^8 s^{-1} T^{-1}
$\boldsymbol{\Theta}$	Debye temperature
θ	Bragg angle
λ_i,λ_f	Initial, final (scattered) neutron wavelength
$\boldsymbol{\mu}$	Atomic magnetic moment
μ_N	Nuclear magneton $(e\hbar/2m_\mathrm{p}) = 5.05078353 \times 10^{-27}$ J T^{-1}
μ_B	Bohr magneton $(e\hbar/2m_\mathrm{e}) = 927.400968 \times 10^{-26}$ J T^{-1}
μ_n	Neutron magnetic moment = $-0.96623647 \times 10^{-26}$ J T^{-1}
ν	Frequency ($\omega/2\pi$)
$\rho(\mathbf{r},t)$	Particle density operator
ρ_0	Average number density
$\boldsymbol{\Sigma}$	Macroscopic cross section associated with a given cross section σ (see below)
σ_a	Absorption cross section
σ_t	Bound total cross section ($\sigma_\mathrm{s} + \sigma_\mathrm{a}$)
σ_c	Bound coherent scattering cross section
σ_i	Bound incoherent scattering cross section
σ_s	Bound scattering cross section ($\sigma_\mathrm{c} + \sigma_\mathrm{i}$)
$\frac{1}{2}\boldsymbol{\sigma}$	Neutron spin (Pauli) operator

$\boldsymbol{\tau}$	Reciprocal lattice vector $\{2\pi[(h/a),(k/b),(l/c)]\}$
$\boldsymbol{\Phi}$	Neutron flux (typically defined as neutrons crossing per unit area per unit time)
ϕ	Scattering angle ($=2\theta$)
χ	Susceptibility
$\chi(\mathbf{Q}, E)$	Generalized susceptibility
Ω	Solid angle
ω	Radian frequency associated with neutron energy transfer $E = \hbar\omega$
$\omega_k(\mathbf{q})$	Frequency of normal mode k

REFERENCE

[1] All numerical values have been taken from the CODATA Recommended Values of the Fundamental Physical Constants, as detailed in P.J. Mohr, B.N. Taylor, D.B. Newell, Rev. Mod. Phys. 84 (2010) 1527−1605. Updated (2010) values can be found at physics.nist.gov/cuu/Constants/ (Last accessed on 12.08.15).

This page intentionally left blank

Chapter 3

High-Temperature Superconductors

Yu Song* and **Pengcheng Dai**
Department of Physics and Astronomy, Rice University, Houston, Texas, USA
**Corresponding author: E-mail: Yu.Song@rice.edu*

Chapter Outline

3.1 INTRODUCTION

Understanding the microscopic origin of high-temperature superconductivity in cuprate and iron-based superconductors is at the forefront of condensed matter physics. Since the parent compounds of cuprate and iron-based superconductors are antiferromagnets with long-range magnetic order and superconductivity arises by electron- or hole-doping into the parent compounds, the key question to be answered is how magnetism is related to superconductivity. The relevance of magnetism is indisputable, evidenced by proximity of superconductivity to

Experimental Methods in the Physical Sciences, Vol. 48. http://dx.doi.org/10.1016/B978-0-12-802049-4.00003-8

magnetic order in cuprates, iron pnictides and heavy fermion superconductors and the presence of intense magnetic excitations in the superconducting state obviating from the paradigm of conventional BCS superconductors. However, the exact role of magnetism and whether magnetic excitations play the role of pairing glue analogous to phonons in conventional superconductors is still not resolved. Neutron scattering has played a key role toward our current understanding of magnetism in high-temperature superconductors and related compounds, here we review key results and recent progress in cuprate and iron-based superconductors.

The discovery of superconductivity in the cuprate $La_{2-x}Ba_xCuO_4$ [1] took the physics community by surprise. It completely goes against the rules set out by Matthias [2] for finding higher T_c, the weak electron−phonon coupling in these materials suggested a non-phonon pairing mechanism (hence "unconventional" superconductivity in contrast to phonon mediated "conventional" superconductivity; alternatively, unconventional superconductivity may be defined by its sign-changing superconductivity order parameter on different parts of the Fermi surface). Neutron diffraction soon uncovered the parent compound La_2CuO_4 to be a Mott insulator with antiferromagnetic order [3]. This finding highlighted the relevance of magnetism and set the stage for research in high-temperature superconductivity where neutron scattering played a key role. With the discovery of superconductivity above 77 K in $YBa_2Cu_3O_{6+x}$ [4], cuprates became bona fide high-temperature superconductors. Recent developments in neutron scattering instrumentation and single-crystal growth techniques allowed comprehensive studies of magnetic excitations in the cuprates, despite the small magnetic moment of Cu^{2+} and the large bandwidth of magnetic excitations (in magnetically ordered cuprate parent compounds, this corresponds to the spin-wave bandwidth which is $\sim 2J$, J being the nearest-neighbor exchange coupling). The fact that cuprates are two-dimensional (2D) systems coupled with time-of-flight neutron spectroscopy with large area detectors allowed magnetic excitations throughout the Brillouin zone to be mapped efficiently. While there is still no consensus regarding the exact mechanism of superconductivity in the cuprates, a universal picture for the evolution of spin excitations has emerged for different families of hole-doped cuprates. The spin waves in the parent compounds and their evolution in doped cuprates have been reviewed in Refs [5−10]. Here key results and more recent results are reviewed.

The discovery of superconductivity in iron pnictides [11] presents a new challenge. While also based on 2D structural motifs, the multiband nature makes this system even more challenging to understand and each family of materials appears unique. Unlike the cuprates, even the nature of the magnetism in the parent compounds of the iron pnictides is perplexing. While spin waves have been mapped out in the parent compounds of iron-pnictide superconductors, interpretations involving either itinerant electrons or local moments have been

presented [12]. Compared to hole-doped cuprates, significant differences exist among different families of iron-based superconductors, both in their electronic structure and spin-excitation spectra. Neutron scattering has made significant contributions toward understanding the magnetism in iron pnictides and has been reviewed in Refs [12–14]. Here we will review neutron scattering results in the iron pnictides/chalcogenides focusing on systematic single-crystal studies on systems derived from $BaFe_2As_2$, NaFeAs, and FeTe. Alkali metal iron chalcogenides present another intriguing case of unconventional superconductivity where superconductivity can be induced with the suppression of antiferromagnetic order [15]. While the jury is still out on which phase is responsible for superconductivity and how the insulating phase with block antiferromagnetic order is related to superconductivity, neutron scattering has played an essential role in determining the nature of these systems. The physics of this specific system has been reviewed in Ref. [16], here we will survey the neutron scattering results so far and discuss their significance.

Polarized neutron scattering allows the polarization dependence of magnetic excitations and the ordered magnetic moment to be studied [17]. Typically, such a setup requires a guide field, and in the case of superconductors the Meissner effect tends to affect the polarization of the neutrons. Development of techniques allowing the sample to be in zero-field allowed detailed studies of polarization dependence of magnetic excitation in both the cuprates and iron-based superconductors. By tuning the polarization direction of the neutron, it is further possible to measure the magnetic response polarized along each crystallographic direction. Here we review the principles used in such experiments and some results.

With improvements of energy resolution below 0.1 eV, resonant inelastic X-ray scattering (RIXS) has demonstrated comparable capability in measuring high-energy spin excitations in both cuprates [18] and iron pnictides [19]. With RIXS instruments having even better energy resolution scheduled to come on line, RIXS is undoubtedly challenging neutron scattering's monopoly in measuring magnetic excitations resolving both energy and momentum. Since RIXS and neutron scattering probe different regions of reciprocal space, these two techniques provide complementary information in the study of high-temperature superconductors. RIXS results on the cuprates and iron pnictides and comparison with neutron scattering are discussed.

3.2 HOLE-DOPED CUPRATE SUPERCONDUCTORS

3.2.1 Magnetic Order and Spin Waves in the Parent Compounds

For the purpose of neutron scattering, compounds based on La_2CuO_4 and $YBa_2Cu_3O_{6+x}$ are most studied due to availability of large single crystals. La_2CuO_4 orders magnetically below $T_N \approx 320$ K [20]. The ordered moments

are collinear and lie in the CuO_2 planes oriented at 45° from the Cu−O bond directions (Figure 1(a)) [21]. In the case of $YBa_2Cu_3O_{6+x}$, the actual doping per Cu^{2+} in the CuO_2 planes p does not have a simple relation to x, but for samples with $x \leq 0.15$, p is sufficiently small that it can be regarded as the parent phase [22]. $YBa_2Cu_3O_{6.05}$ orders below $T_N \approx 410$ K with magnetic moments lying in the CuO_2 planes parallel to the Cu−O bond directions (Figure 1(b)) [23]. In both systems, the magnetic unit cells have the same size along c as the structural unit cells shown in Figure 1, whereas in the CuO_2 plane the size is doubled. Therefore, magnetic Bragg peaks occur at (1/2,1/2,1) and equivalent positions. In the case of $YBa_2Cu_3O_{6+x}$, the bilayer structure gives rise to a sinusoidal modulation of the magnetic structure factor along L (reciprocal lattice units are defined as $(H,K,L) = \left(\frac{q_x a}{2\pi}, \frac{q_y b}{2\pi}, \frac{q_z c}{2\pi}\right)$ where the momentum transfer $\mathbf{Q} = (q_x, q_y, q_z)$ is in units of Å^{-1}). Since both cuprates and iron-based superconductors are quasi-2D, the L component of $\mathbf{Q}$ is sometimes dropped resulting in notation of the form (H,K).

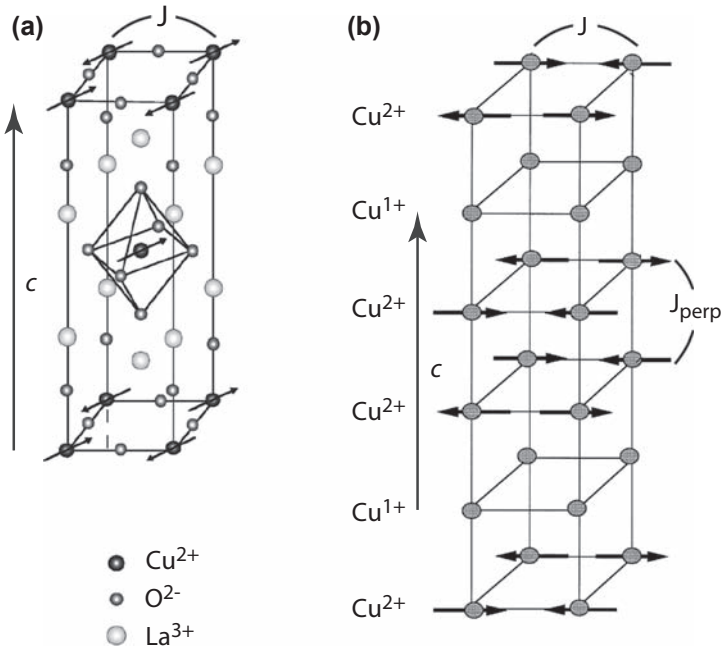

FIGURE 1 Magnetic structure for La_2CuO_4 [21] and $YBa_2Cu_3O_{6+x}$ with $x < 0.4$ [23]. (a) Magnetic structure of La_2CuO_4 [21]. *Adapted with permission from Ref. [21].* (b) The magnetic structure of $YBa_2Cu_3O_{6+x}$ with $x < 0.4$, only Cu atoms are shown, the structure consists of magnetic Cu^{2+} layers and nonmagnetic Cu^{1+} layers. *Adapted from Ref. [23].* Lengths of the unit cells along c axis are shown in the figure by vertical arrows.

The magnetic interactions in cuprate parent compounds are dominated by the superexchange between in-plane nearest-neighbors J which is on the order of 100 meV [7]. Magnetic interactions over longer distances, while much weaker than J, are still significant compared to the superconductivity pairing energies. To obtain these interactions, it is necessary to obtain the dispersion of spin waves along the zone boundary. In La_2CuO_4 this was accomplished and the dispersion of spin waves along the zone boundary is interpreted as due to a cyclic exchange term J_c (58(4) meV) that is almost half of J (143(2) meV) at 10 K. Within this interpretation, the next-nearest (J') and next-next-nearest (J'') interactions are 5% of J_c [20,24] (Figure 2(a) and (b)). In addition, it was found that spin waves at the (1/2,0) zone boundary position show strong damping compared to another zone boundary position (1/4,1/4) [20] (Figure 2(c)). This is surprising as the energy of the spin waves at the zone boundaries ($\sim 2J$) is much smaller than the charge-transfer gap in La_2CuO_4. The authors argued that

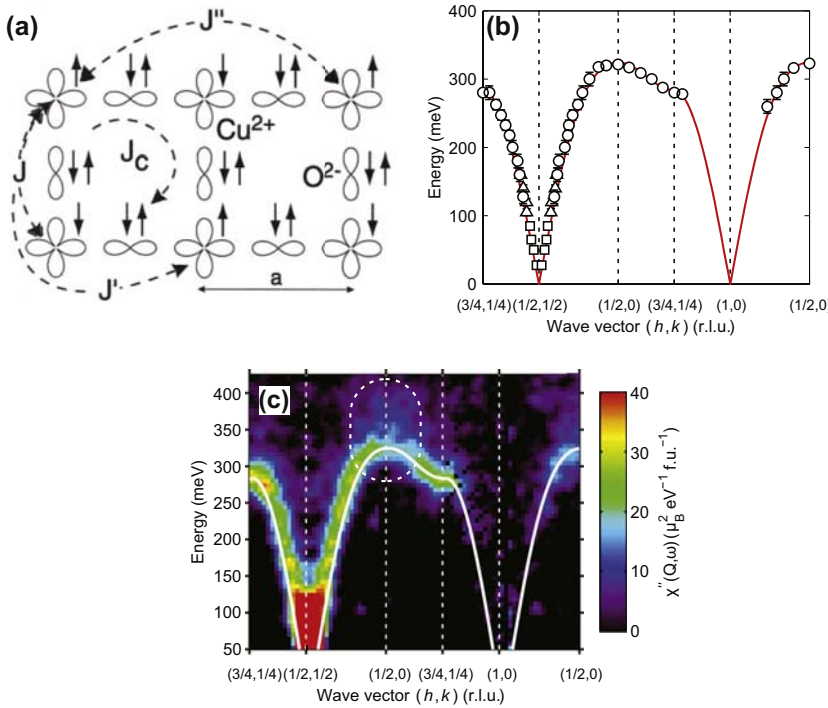

FIGURE 2 Spin waves in La_2CuO_4. (a) The exchange couplings for La_2CuO_4. *Adapted with permission from Ref. [24].* The dispersion (b) and intensity (c) of spin waves in La_2CuO_4. *Adapted with permission from Ref. [20].* The spin waves are damped near (1/2,0) despite the spin-wave energies being much smaller than the charge-transfer gap in La_2CuO_4, as can be seen in (c) inside the dashed ellipse.

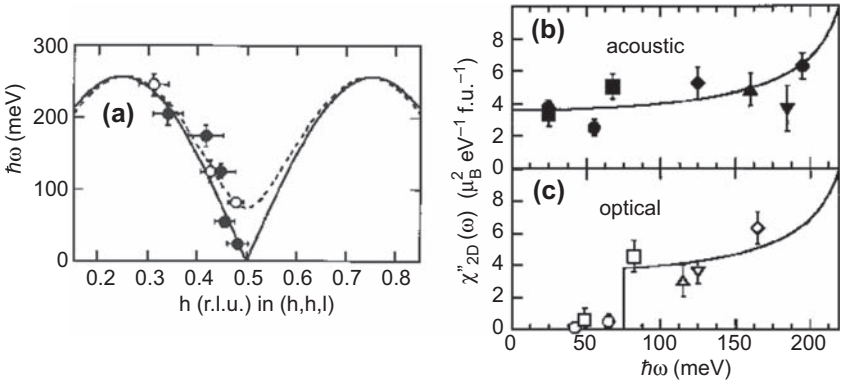

FIGURE 3 Spin waves in $YBa_2Cu_3O_{6.15}$. *Adapted with permission from Ref. [25].* (a) The spin-wave dispersions of the acoustic and optical spin-wave modes. The closed symbols and the solid line correspond to the acoustic branch, the open symbols and the dotted line refer to the optical spin-wave branch. The local susceptibilities for the acoustic (b) and optical (c) spin-wave branches. Above ~100 meV, the acoustic and optical branches become almost identical.

the damped zone boundary spin waves at (1/2,0) decay into a two-spinon continuum which has a lower energy at (1/2,0) than (1/4,1/4).

Compared to La_2CuO_4 where the couplings between CuO_2 layers are weak, the parent phase of $YBa_2Cu_3O_{6+x}$ consists of coupled CuO_2 bilayers. This doubling of CuO_2 planes results in an optical spin-wave branch not present in monolayer La_2CuO_4. Measurements of both the acoustic and the optical spin-wave branches enabled a determination of the in-plane nearest-neighbor coupling $J = 125(5)$ meV and the out-of-plane nearest-neighbor coupling $J_{perp} = 11(2)$ meV (Figure 3) [25]. So far there is no report of spin-wave dispersion along the zone boundary in $YBa_2Cu_3O_{6+x}$ and it is not clear if the cyclic exchange and damping of spin waves at (1/2,0) are unique to La_2CuO_4 or common features of cuprate parent compounds.

Due to quantum fluctuations, both the spin-wave energies and the intensities will be renormalized compared to values derived from the classical large-S limit. Neutron scattering cannot directly measure the spin-wave energy renormalization factor Z_c, instead $Z_c = 1.18$ is assumed to extract the exchange couplings [24,25]. The spin-wave intensity renormalization factors Z_d for La_2CuO_4 is 0.40(4) [20] and for $YBa_2Cu_3O_{6.15}$ $Z_\chi = 0.4(1)$ ($Z_d = Z_\chi Z_c$) has been reported [25], these values are smaller than $Z_d \sim 0.6$ obtained in theoretical studies [26]. Quantum fluctuations, therefore, increase the spin-wave bandwidth and decrease spin-wave intensities. The total moment squared obtained in La_2CuO_4 is $\langle M_{tot}^2 \rangle = 1.9(3)\ {\mu_B}^2$, compared to $3\ {\mu_B}^2$ expected for $S = 1/2$ [20]. The reduction of the observed total moment may be due to the presence of magnetic excitations at higher energies that is not included in the estimate, another possible cause is hybridization of Cu 3d orbitals with O p orbitals causing a marked drop of magnetic intensity as found in Sr_2CuO_3 [27].

Such hybridization effects will be manifested in the magnetic form factor, while it has long been established that the Cu^{2+} magnetic form factor is anisotropic [28], only in recent works [29] hybridization effects are taken into account when considering the magnetic form factor.

2D spin correlations survive above T_N in both La_2CuO_4 and $YBa_2Cu_3O_{6+x}$, a result of the dominant nearest-neighbor J being much larger than the interlayer coupling and 3D magnetic ordering is bottlenecked by the weaker interlayer coupling [7]. It is interesting to note that persistence of 2D spin correlations above T_N is also found in $BaFe_2As_2$ [30] and $CeRhIn_5$ [31], the parent compounds of iron-based superconductors, and heavy fermion superconductors.

3.2.2 Evolution of Magnetic Excitations upon Doping

Upon doping by holes, the commensurate antiferromagnetic order in the parent compound is very quickly suppressed at $p \sim 0.02$ as shown in the phase diagram of $La_{2-x}Sr_xCuO_4$ (Figure 4) [8,32]. The long-range commensurate order

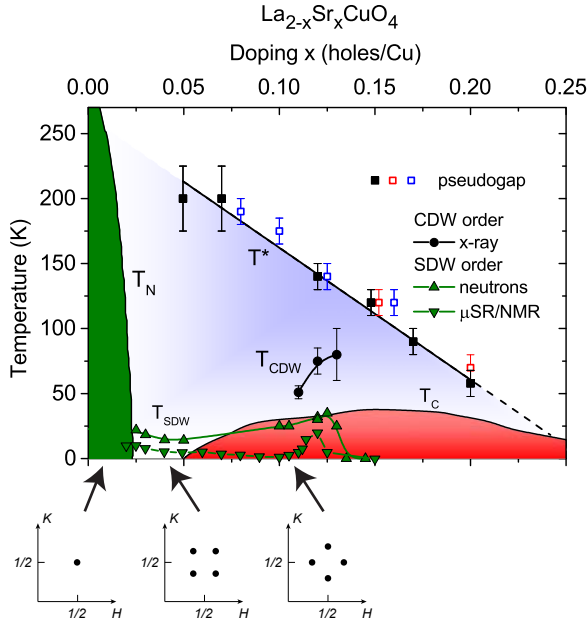

FIGURE 4 The phase diagram of $La_{2-x}Sr_xCuO_4$. *Adapted with permission from Ref. [32].* Schematics for low-energy magnetic excitations are shown at the bottom of the figure for the commensurate long-range ordered, the spin-glass (SG), and the superconducting (SC) regime. The low-energy excitations in the commensurate long-range ordered phase are commensurate spin waves, in the SG phase they form quartets split along the (110) direction and in the SC phase they form quartets split along the Cu—O bond directions ((100) direction). In untwinned samples the quartet in the SG phase becomes two peaks. CDW, charge density waves; SDW, spin density waves.

is supplanted by incommensurate magnetic order in the doping range $p \sim 0.02$ to ~ 0.055 corresponding to a spin-glass phase. For doping levels higher than $p \sim 0.055$, superconductivity appears. At $p = 0.125$ there is a slight dip in the superconductivity dome and optimal superconductivity is achieved at $p \sim 0.16$ (this is termed optimal doping, compounds below and above this doping level are described as underdoped and overdoped, respectively). For $p \sim 0.25$, superconductivity disappears giving way to a Fermi liquid metallic state.

In the spin-glass phase, the incommensurate magnetic order and excitations are split along the (110) direction at 45° to the Cu−O bonds. Upon just entering the superconducting state, the incommensurate magnetic order split along the (110) direction rotates by 45° becoming parallel to (100) and then disappears at higher doping levels [33], while the low-energy excitations persist (low-energy excitations stem from the magnetic ordering wave vector and also rotate by 45° along with the magnetic ordering wave vector near the boundary between superconductivity and the spin-glass regime). Despite the rotation by 45° of the incommensurate magnetic order and low-energy excitations, the splitting scales linearly with doping until saturating around optimal doping (Figure 5(a)) [8,33]. Both the transitions from long-range commensurate order to incommensurate order split along (110), and the rotation of incommensurate magnetic order involves samples with phase separation, suggesting both transitions are first order in nature. In contrast, a quantum critical point seems to be involved with the disappearance of the incommensurate magnetic order split along (100), where application of a magnetic field pushes this quantum critical point to higher doping levels [34−36] (Figure 5(b)).

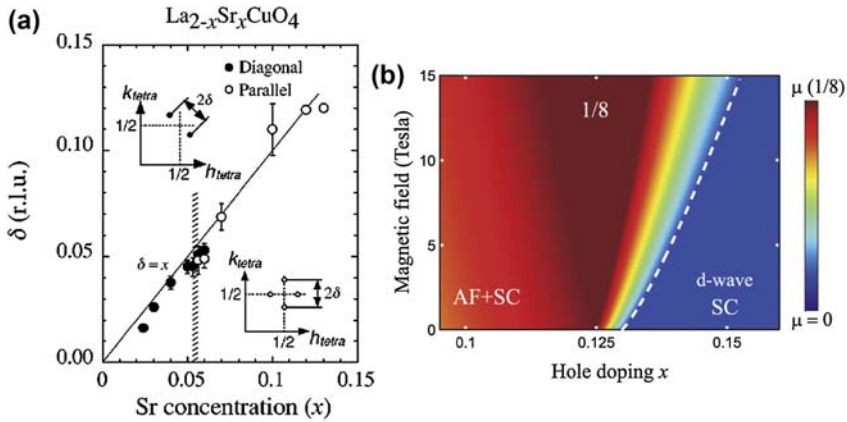

FIGURE 5 (a) The splitting of incommensurate peaks in $La_{2-x}Sr_xCuO_4$. Despite the rotation by 45° of the splitting direction, the splitting itself increases linearly with $p \approx \delta$. *Adapted with permission from Ref. [33].* (b) The disappearance of incommensurate order along (100) in $La_{2-x}Sr_xCuO_4$ involves a quantum phase transition, the critical point can be driven to higher doping levels with the application of a magnetic field. *Adapted with permission from Ref. [36].* SC, superconducting.

A very similar phase diagram with incommensurate magnetic excitations rotating from split along (110) to split along (100) is also found in $Bi_{2+x}Sr_{2-x}CuO_{6+y}$ [37], demonstrating that the complexity of the phase diagram outlined above is not unique to $La_{2-x}(Sr,Ba)_xCuO_4$. In $YBa_2Cu_3O_{6+x}$, there is no phase with incommensurate magnetic ordering split along (110). When long-range magnetic order in the parent phase is suppressed with increasing doping, incommensurate magnetic order split along (100) sets in [38]. In $La_{2-x}Sr_xCuO_4$ with incommensurate order split long (110) and $YBa_2Cu_3O_{6+x}$ with incommensurate excitations split along (100), it has been found in untwinned samples that the low-energy incommensurate magnetic peaks display twofold rotational symmetry (Figure 6) [38–40]. Given that the

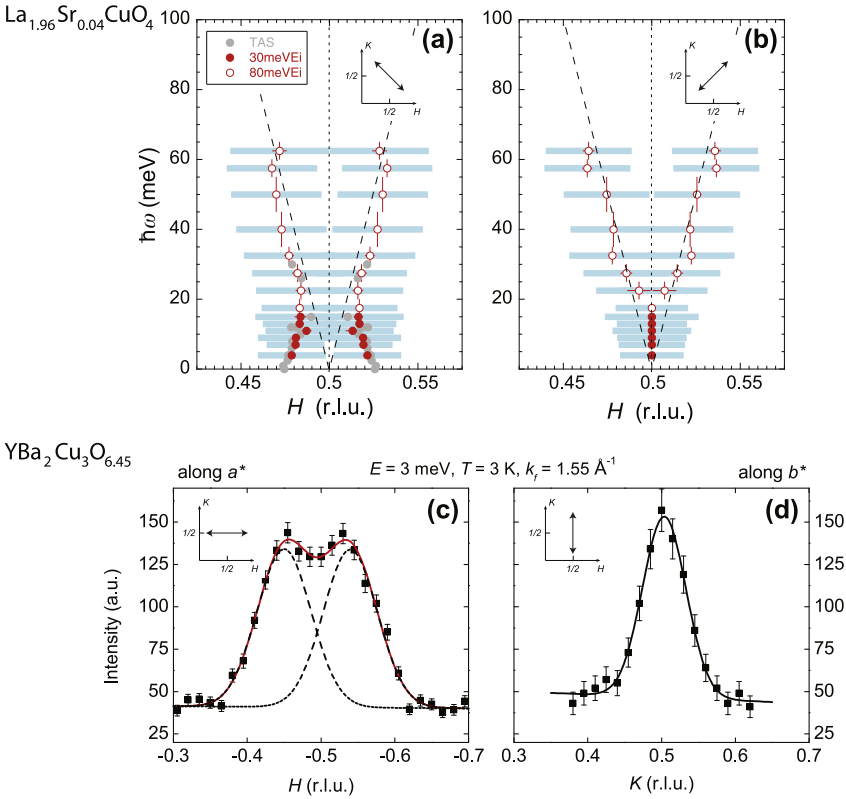

FIGURE 6 (a and b) The twofold rotational symmetry of low-energy excitations in untwinned $La_{1.96}Sr_{0.04}CuO_4$, along the two directions at 45° relative to Cu–O bonds. Clear differences can be seen at low energies, whereas at high energy they both exhibit dispersions similar to La_2CuO_4 (dotted line). *Adapted with permission from Ref. [39].* (c and d) In untwinned $YBa_2Cu_3O_{6.45}$, twofold rotational symmetry is observed at low energies, however, the symmetry axes are along Cu–O bonds, rotated by 45° compared to $La_{1.96}Sr_{0.04}CuO_4$. *Adapted with permission from Ref. [38].*

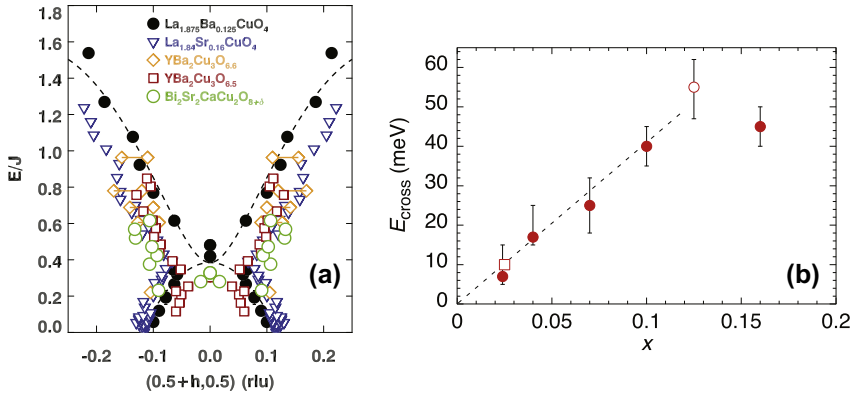

FIGURE 7 (a) The universal hourglass dispersion found in different families of cuprates scaled by J of the parent compound. The dashed line corresponds to $La_{1.875}Ba_{0.125}CuO_4$. It is clear that doping holes causes a softening of high-energy excitations compared to the parent compounds which have bandwidths $\sim 2J$. *Adapted with permission from Ref. [8].* (b) The energy E_{cross} at which the upward dispersion and the downward dispersion meet scales with doping, similar to the splitting of low-energy incommensurate excitations. *Adapted with permission from Ref. [42].*

incommensurability decreases with increasing temperature similar to order parameters, these observations may be associated with electronic nematicity [41]. While we adopt the unit cells in Figure 1, it should be noted that in $La_{2-x}Sr_xCuO_4$ there are small structural distortions that cause (110) and (1−10) to become inequivalent, in $YBa_2Cu_3O_{6+x}$ Cu−O chains cause (100) and (010) to become inequivalent.

The low-energy excitations in hole-doped cuprates emanating from incommensurate positions disperse inward toward (1/2,1/2) until some energy E_{cross} above which it starts to disperse out resembling spin waves in the corresponding parent compounds although with a slightly reduced effective J. Taken together, these features form the well-known universal hourglass dispersion [8] (Figure 7(a)). The inward dispersion has a velocity that is more or less independent of doping, resulting in E_{cross} also increasing linearly with doping and saturating around optimal doping similar to the splitting of incommensurate magnetic order (Figure 7(b)) [42]. A remarkable achievement toward the understanding of hole-doped cuprates is establishing that these behaviors are universal for different families of hole-doped cuprates. The hourglass dispersion has been established in both $La_{2-x}(Sr,Ba)_xCuO_4$, $YBa_2Cu_3O_{6+x}$, and $Bi_2Sr_2CaCu_2O_{8+\delta}$ [8]. The linear dependence of incommensurate splitting with doping has been established for $YBa_2Cu_3O_{6+x}$ and $Bi_{2+x}Sr_{2-x}CuO_{6+y}$ in addition to $La_{2-x}Sr_xCuO_4$ [37]. It should be noted that the splitting is typically determined from elastic magnetic peaks, but in compounds where no magnetic order is found, it is determined from the splitting of low-energy magnetic excitations.

While it is generally accepted that the upward dispersing excitations above E_{cross} are spin-wave-like excitations, there are mainly two approaches for understanding the inward dispersion below E_{cross}. One possibility is these excitations are due to the dynamic version of static stripes found in $La_{2-x}Ba_xCuO_4$ [7]. The phase diagram of $La_{2-x}Ba_xCuO_4$ is similar to $La_{2-x}Sr_xCuO_4$, however, superconductivity is strongly suppressed at $p = 0.125$ where both charge- and spin-stripe orders are found for this doping. Doped holes segregate into stripes resulting in charge ordering and form antiphase domain boundaries for the magnetically ordered regions, resulting in incommensurate elastic magnetic peaks split along Cu−O bond directions. The charge stripe is therefore correlated with spin-stripe ordering. This is in agreement with the observation that the charge-ordering temperature T_{CO} and the spin-ordering temperature T_{SO} are both enhanced near $p = 0.125$ and both compete with superconductivity [32]. While charge ordering and stripe ordering are also found in $La_{2-x}Sr_xCuO_4$ [32], structural distortions in $La_{2-x}Ba_xCuO_4$ making 100 and 010 inequivalent allow such ordering to be much stronger causing the stronger suppression of superconductivity at $p = 0.125$ in $La_{2-x}Ba_xCuO_4$ [9]. These results suggest that the inward dispersion emanating from incommensurate positions in cuprates is due to fluctuations of spin stripes associated with charge stripes [9]. The similar magnetic excitation spectra found for $YBa_2Cu_3O_{6.45}$, $La_{1.875}Ba_{0.125}CuO_4$, and $Bi_2Sr_2CaCu_2O_{8+\delta}$ also supports this scenario [43−45].

In $La_{2-x}Ba_xCuO_4$, static stripes are found and superconductivity is strongly suppressed at $p = 0.125$, whereas in $La_{2-x}Sr_xCuO_4$ and $YBa_2Cu_3O_{6+x}$ T_c, superconductivity is only mildly suppressed. Recently charge ordering and fluctuations have been observed in underdoped $YBa_2Cu_3O_{6+x}$ [46,47] which competes with superconductivity. Upon application of a magnetic field static charge ordering can be induced [48] or enhanced [46] concomitant with the suppression of superconductivity, demonstrating the competition between charge ordering and superconductivity [46]. The charge ordering in $YBa_2Cu_3O_{6+x}$ is found to arise from charge stripes which break fourfold rotational symmetry of the lattice, similar to stripes in $La_{2-x}Ba_xCuO_4$ [49]. Therefore, electronic orders breaking fourfold rotational symmetry that compete with superconductivity seem to be another unifying theme for the hole-doped cuprates. It is worthwhile to note that the detected magnetism in these proposed stripes display 2D rather than 1D magnetism because the magnetic moments from different spin stripes are in fact correlated with each other.

Given the metallic nature of doped cuprates, the hourglass dispersion can also be tackled from the perspective of itinerant electrons by interpreting the low-energy magnetic excitations as particle-hole excitations [50,51]. This approach is appealing since it provides a link between the iron pnictides and the cuprates. However, observation of an hourglass dispersion in insulating $La_{5/3}Sr_{1/3}CoO_4$ suggests itinerant electrons are not necessary and the hourglass dispersion should be ascribed to fluctuating stripes [52]. Since spin stripes are

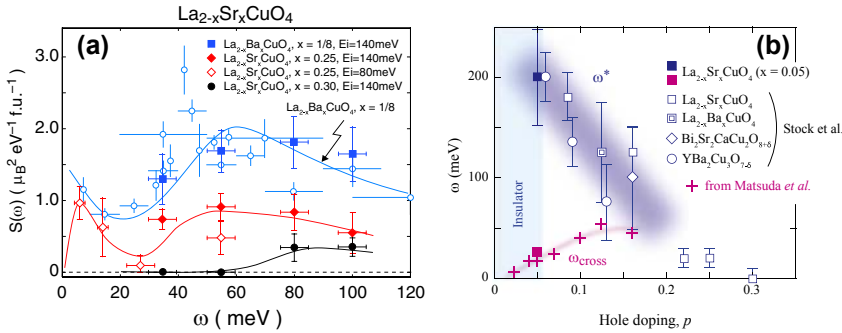

FIGURE 8 Evolution of magnetic spectral weight with doping. (a) Integrated magnetic intensity for $La_{2-x}Sr_xCuO_4$; with increasing doping, the intensity is strongly suppressed [55]. (b) The energy at which χ'' falls to half of the parent compound closely follows the pseudogap energy, E_{cross} is also plotted (ω_{cross} in the figure) [56]. *Adapted with permission from Refs [8,55].*

based on charge stripes, the observation of an hourglass dispersion and incommensurate magnetic order in the absence of charge-stripe order in $La_{1.6}Sr_{0.4}CoO_4$ led the authors to argue that neither the stripe scenario nor band effects are connected to the hourglass dispersion [53], but rather nanoscopic phase separation is responsible [54]. More research is needed to settle the origin of the hourglass spectrum and its relationship to superconductivity.

With increasing hole-doping, the overall magnetic intensity is suppressed, and the effective coupling is reduced resulting in softened and weaker spin excitations [55] (Figure 8(a)). Interestingly, by tracking the energy at which the magnetic signal falls to half of that of the parent compound, it was found that this energy tracks the well-known pseudogap energy very well (Figure 8(b)) [56]. The suppression of magnetic spectral weight agrees with Raman scattering measurements of bimagnons [57].

3.2.3 Neutron Scattering versus RIXS

In RIXS, the scattering process is similar to inelastic neutron scattering, an incident photon is scattered exchanging both energy and momentum with the sample. By tuning the incident photon energy to match the absorption edge of specific elements the inelastic scattering cross sections can be significantly enhanced, this in addition allows for element selectivity. The RIXS inelastic cross section is sensitive to magnetic, charge, and orbital degrees of freedom, while versatile this also means the RIXS cross section is more complicated than that for neutron scattering. Compared to neutron scattering RIXS only needs very small sample volumes, but since incident photons are typically $\sim$keV it is challenging to resolve excitations in solids which are typically $\sim$0.1 eV [58]. Recent advances in RIXS instrumentation have allowed measurements of spin excitations in cuprates with reasonable energy resolution.

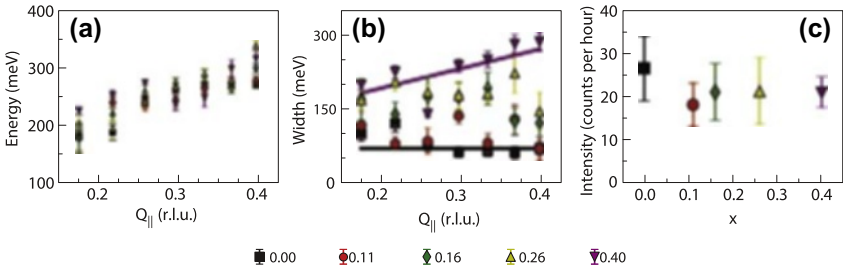

FIGURE 9 The evolution of magnetic excitations in $La_{2-x}Sr_xCuO_4$ with doping seen by resonant inelastic X-ray scattering measured along (1,0) direction at $(Q_{||},0)$. (a) The dispersions show no/small doping dependence. (b) The energy widths of magnetic excitations become much broader for doped cuprates. (c) The averaged magnetic intensity does not change with doping. *Adapted with permission from Ref. [59].*

The spin excitations in $La_{2-x}Sr_xCuO_4$ were found to neither soften nor weaken in terms of intensity even up to the overdoped regime with $p = 0.2$ (Figure 9), compared to spin waves in La_2CuO_4 [59]. The persistence of spin excitations was also found in many other hole-doped cuprate superconductors [18,60]. These results seem to contradict the observations of neutron scattering, where significant reduction of magnetic spectral weight is observed for doped cuprates [56]. An important difference between neutron scattering and RIXS is that neutron scattering measures near (1/2,1/2), RIXS measures near (0,0). In the antiferromagnetically ordered parent compounds, spin waves emanating from (0,0) and (1/2,1/2) have identical dispersion but the structure factor near (1/2,1/2) is much larger. When holes are doped resulting in the destruction of antiferromagnetic order, (0,0) and (1/2,1/2) are no longer equivalent. Therefore, the persistence of spin excitations with doping near (0,0) does not necessarily contradict the suppression of spin excitations near (1/2,1/2). However, since the magnetic spectral weight is concentrated near (1/2,1/2), the integrated magnetic spectral weight will still be strongly suppressed with doping despite the persistence of spin excitations near (0,0).

Also it should be noted that, whereas the neutron scattering cross section is simple and well understood, the RIXS cross section is considerably more complicated including contributions from magnetic, charge, and orbital degrees of freedom [58]. Therefore, it would be ideal if the RIXS results can be reproduced with neutron scattering especially for the doped compounds where, due to the suppression of antiferromagnetic order, magnetic excitations near (0,0) are no longer equivalent to those near (1/2,1/2). However, so far no such results have been reported, possibly because the structure factor is too small near (0,0) for neutron scattering.

Compared to neutron scattering the sample volume required for RIXS is much smaller, and it has even been possible to measure spin excitations in heterostructures consisting of single La_2CuO_4 layers [61]. In addition, RIXS is

element sensitive, making it an ideal probe to study compounds where more than one element could be magnetic. With several new RIXS instruments with even better energy resolution coming on line in the near future, RIXS is poised to become a very powerful probe in measuring spin excitations in addition to neutron scattering.

3.2.4 The "Resonance" Mode in the Superconducting State

Upon cooling below T_c, a "resonance" mode has been found in many superconducting cuprates. Loosely speaking, the resonance mode refers to strong enhancements of collective magnetic excitations at certain wave vectors and energy transfers due to superconductivity. Experimentally, the mode is observed by subtracting the neutron scattering intensity in the normal state just above T_c from the signal in the superconducting state (Figure 10(a) and (b)). In addition, the resonance mode responds to the onset of superconductivity. In hole-doped cuprates, the energy of the resonance mode does not change as a function of temperature while its intensity resembles the superconductivity order parameter (Figure 10(c)). Formation of the resonance mode is typically associated with

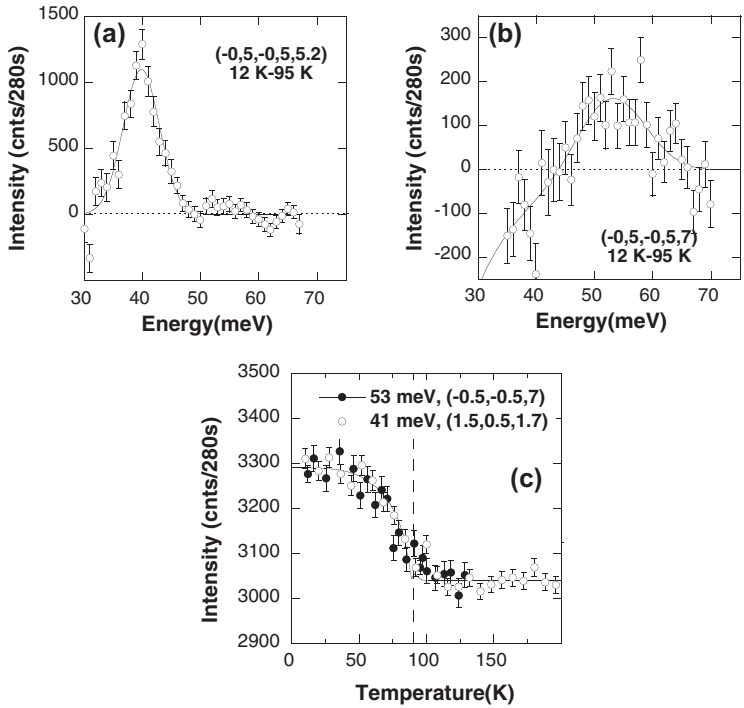

FIGURE 10 The resonance mode seen in $YBa_2Cu_3O_{6.85}$, obtained by subtracting the signal just above T_c from the signal well below T_c. *Adapted with permission from Ref. [78].* (a) The odd mode. (b) The even mode. (c) Temperature dependence of both the odd and even modes scaled together.

the opening of a spin gap at energies below the resonance, where upon entering the superconducting state magnetic spectral weight shifts from inside the spin gap to the resonance mode. The resonance mode in hole-doped cuprates was initially discovered in $YBa_2Cu_3O_{6+x}$ [62] and was later found in $La_{2-x}Sr_xCuO_4$ [63], $Bi_2Sr_2CaCu_2O_{8+\delta}$ [64], $Tl_2Ba_2CuO_{6+\delta}$ [65], and $HgBa_2CuO_{4+\delta}$ [66]. Similar enhancements were also observed in electron-doped cuprates [67], iron-based superconductors [68], and heavy fermion superconductors [69–71]. It has been argued that the energy of the resonance mode scales with T_c [72] or the superconducting gap [73]. The spin gap in $YBa_2Cu_3O_{6+x}$ due to superconductivity is found to scale with T_c [74]. In the cuprates, iron pnictides, and heavy fermion superconductors, the change in magnetic exchange energy in the superconducting state due to the resonance mode is sufficient to account for the superconductivity condensation energy [71,75,76].

In the case of $La_{2-x}Sr_xCuO_4$, the resonance occurs at incommensurate positions below E_{cross}, the spin gap is small, and the magnetic excitations above T_c are already strong unlike in other hole-doped cuprates [63,77]. Interestingly in bilayer cuprates $YBa_2Cu_3O_{6+x}$ [78] and $Bi_2Sr_2CaCu_2O_{8+\delta}$ [79], two resonance modes, one with odd symmetry and another with even symmetry in the bilayers, are found (Figure 10(a) and (b)), similar to the acoustic and optical spin waves found in the parent phase of $YBa_2Cu_3O_{6+x}$ [25]. The average energy of the two modes has been argued to correspond to the energy of the resonance in single-layer cuprates [80], the average has been also used by Yu et al. [73] to arrive at the universal relationship between the resonance energy and the superconducting gap. In underdoped $YBa_2Cu_3O_{6+x}$, the resonance mode was found to survive above T_c in the pseudogap state [81].

In slightly underdoped $YBa_2Cu_3O_{6+x}$, the resonant mode forms an hourglass dispersion [78], similar to the excitations in the normal state of $La_{1.875}Ba_{0.125}CuO_4$ [44]. One way to unify the magnetic excitations in different systems is to consider them to be dynamic stripes as described above, which is essentially a local-moment approach. Such a description is a natural extension of the spin waves in the insulating parent compounds. Alternatively, an entirely itinerant approach appropriate for optimal doped and overdoped cuprates has been widely studied [82,83]. In this picture, the resonance is a spin-exciton inside the particle-hole continuum, and spin fluctuations measured by neutron scattering at the wave vector $\mathbf{Q}$ are favored when $\mathbf{Q}$ connects Fermi surfaces (at $\mathbf{k}$ and $\mathbf{Q}+\mathbf{k}$) with opposite superconductivity order parameters ($\Delta(\mathbf{k}+\mathbf{Q}) = -\Delta(\mathbf{k})$). In the case of cuprates, this is satisfied at $\mathbf{Q} = (1/2,1/2)$ which connects "hot spots" near the Fermi surface with opposite superconductivity order parameters. The hourglass dispersion can be reproduced by calculating the threshold of the particle-hole continuum which puts an upper limit on the resonance energy (Figure 11) [80,82]. It has been suggested that this interpretation of the resonance mode serves as a "common thread" linking different families of unconventional superconductors [83]. The observation of a "Y"-shaped normal state response in $YBa_2Cu_3O_{6+x}$ suggests that this approach is more appropriate for

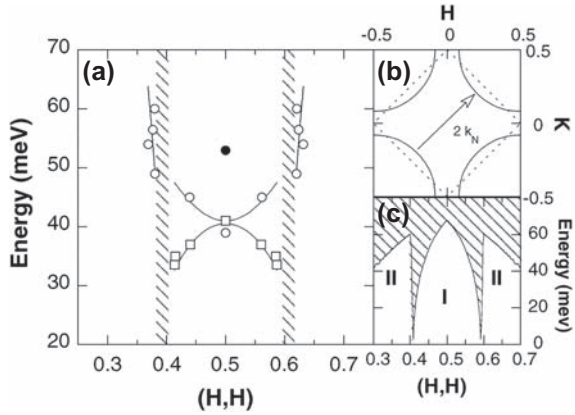

FIGURE 11 Resonance modes in $YBa_2Cu_3O_{6.85}$. *Adapted with permission from Ref. [78].* (a) Experimentally observed dispersion of the resonance, open (full) symbols represent resonance modes with odd (even) symmetry. (b) Typical Fermi surface found in hole-doped cuprates. (c) Electron-hole spin-flip continuum, the downward dispersion is enforced by the continuum going to zero at the border between regions I and II.

$YBa_2Cu_3O_{6+x}$ than dynamic stripes [84]. This approach, however, cannot account for the hourglass magnetic excitations in $La_{1.875}Ba_{0.125}CuO_4$, where stripe order is clearly a better description. The enhancement of magnetic excitations in $La_{2-x}Sr_xCuO_4$ is interpreted as a reduction in damping rather than a spin-exciton [85]. Such a mechanism accounts for the enhancement of phonon lifetimes and intensities in conventional superconductors [86]. Recently, a "Y"-shaped magnetic response in both the superconducting and the normal state was uncovered in $HgBa_2CuO_{4+\delta}$ [87], representing a departure from the universal hourglass dispersion.

The dichotomy of theoretical descriptions of magnetic excitations in doped cuprates has been a long-standing issue in the field. It is clear that cuprates become less correlated with increasing doping and for a large part of the phase diagram reside in the intermediate coupling regime. The difficulty with reconciling the itinerant and the local moment approaches could be the lack of a suitable description of magnetism in the intermediate coupling regime. Similar difficulties are all the more apparent in the iron-based superconductors, where even how to describe the magnetism in the parent compounds is not entirely clear.

3.3 IRON-BASED SUPERCONDUCTORS

3.3.1 Introduction, Compounds, and Phase Diagrams

While the physics of superconducting cuprates remains to be elucidated, the discovery of high-temperature superconductivity in iron pnictides [11] opened up a whole new perspective to tackle the problem. The discovery of

antiferromagnetic order in the parent compound highlights the relevance of magnetism in superconductivity [88] similar to the cuprates. However, in stark contrast to the cuprates, the parent compounds of iron pnictides are metallic, and the presence of nested electron and hole Fermi surfaces suggests that the magnetism may be of itinerant origin [2]. This initial observation raises the question whether superconductivity in the two systems can have the same origin. Unlike the parent compounds of the cuprates, the parent compounds of the iron-based superconductors reside in the intermediate coupling regime, similar to doped cuprates [89]. It is not clear whether the iron pnictides are also close to a Mott-insulating phase as theoretically proposed [90].

Iron-based superconductors that are well studied can be divided into five families, iron pnictides 1111 (e.g., $LaFeAsO_{1-x}F_x$), 122 (e.g., $Ba(Fe_{1-x}Co_x)_2As_2$), 111 (e.g., $NaFe_{1-x}Co_xAs$), iron chalcogenides (e.g., $FeTe_{1-x}Se_x$), and alkali metal iron chalcogenides (e.g., $K_xFe_{2-y}Se_2$). The parent compounds of iron pnictides (e.g., LaFeAsO, $BaFe_2As_2$, and NaFeAs) are metallic paramagnets with tetragonal crystal structure at room temperature. As the temperature is lowered, the crystal structure changes to orthorhombic at the structural transition temperature T_S, and then long-range antiferromagnetic order develops at T_N. Although the structural transition either precedes or coincides with the magnetic transition, it is believed to be driven by electronic degrees of freedom [91]. The parent compounds of the iron pnictides adopt collinear magnetic order (stripe order) [88], the magnetic structure of FeTe is instead bicollinear magnetic order (double-stripe order) [92]. The insulating alkali metal iron chalcogenide is made up of antiferromagnetically aligned ferromagnetic blocks with four Fe atoms (block checkerboard antiferromagnetic order) [93].

Starting from the parent compound of the iron pnictides such as $BaFe_2As_2$, superconductivity can be induced by applying pressure, electron-doping, hole-doping, and even isovalent substitution [94,95]. For example, starting from $BaFe_2As_2$, superconductivity can be induced by introducing alkali metals at Ba sites; Co, Ni, Ru, or Rh at Fe sites; and P at As sites. Curiously, while doping Cr or Mn at Fe sites suppresses the magnetic order, superconductivity is not induced. The phase diagrams for $Ba_{1-x}K_xFe_2As_2$ and $Ba(Fe_{1-x}Co_x)_2As_2$ are shown in Figure 12(a), superconductivity is induced in both cases by doping either holes or electrons. However, T_S and T_N split with Co doping while they remain coincident for K doping. There is also a region where superconductivity coexists with antiferromagnetic order in both cases. The phase diagrams for other iron pnictides are similar to Figure 12(a). For NaFeAs and LaFeAsO, T_S and T_N are already split in the parent phase, whereas LiFeAs is paramagnetic with tetragonal crystal structure at all temperatures. The phase diagram for $FeTe_{1-x}Se_x$ is shown in Figure 12(b), doping Se in FeTe suppresses magnetic ordering and results in a glassy magnetic state at low dopings before inducing bulk superconductivity. There is no coexistence of long-range magnetic order and superconductivity. The end member FeSe also superconducts at 8 K, and it has also been proposed that Fe_4Se_5 is the parent compound for

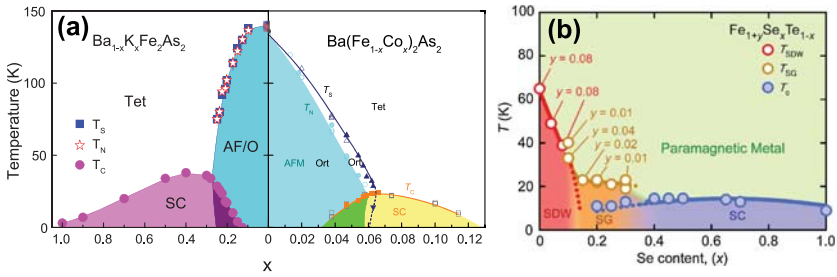

FIGURE 12 (a) Phase diagram of $Ba_{1-x}K_xFe_2As_2$ and $Ba(Fe_{1-x}Co_x)_2As_2$. T_S and T_N split with Co doping, but remains coincident for K doping [14]. (b) Phase diagram of $FeTe_{1-x}Se$, a glassy magnetic phase separates long-range magnetic order from bulk superconductivity. *Adapted with permission from Ref. [229].*

iron chalcogenides instead of FeTe [96]. The case of alkali metal iron chalcogenides is more complicated due to phase separation. While a phase diagram where superconductivity is induced with the suppression of antiferromagnetic order has been proposed [15], the exact phase responsible for superconductivity is still under debate [16]. Sections 3.3.2–3.3.5 will focus on magnetism in the iron pnictides and iron chalcogenides. Magnetism in alkali-metal iron chalcogenides is discussed in Section 3.3.6. Results from polarized neutron scattering experiments are discussed in Section 3.3.7.

3.3.2 Antiferromagnetically Ordered Metallic Parent Compounds

At room temperature, the parent compounds of iron pnictides adopt a tetragonal structure as shown in Figure 13(a) and (b), while for 122 compounds the chemical unit cell consists of two FeAs layers; 11, 111, and 1111 compounds have only one FeAs/FeTe(Se) layer in the chemical unit cell. Upon cooling, the tetragonal crystal structure changes to orthorhombic, this transition is first order for $SrFe_2As_2$ and $CaFe_2As_2$ but is second order for $BaFe_2As_2$ and NaFeAs [97,98]. The orthorhombic unit cell is rotated by 45° compared to the tetragonal unit cell and is twice as large in the *ab* plane. Stripe magnetic order appears in the orthorhombic phase with spins oriented along the longer in-plane orthorhombic axes (a_O) when temperature is further lowered (Figure 13(d)). In the notation of the orthorhombic chemical unit cell, the magnetic order appears at $(1,0,1)_O$ and equivalent wave vectors for 122 compounds and $(1,0,0.5)_O$ for 111 and 1111 compounds. The magnetic transition is first order for $BaFe_2As_2$, $SrFe_2As_2$, and $CaFe_2As_2$, but is second order for NaFeAs [97,98]. Upon electron doping, both the structural and magnetic transitions become second order. In the discussion of magnetic scattering, we typically adopt the orthorhombic notation and use subscripts to indicate which notation is used. In the orthorhombic notation, magnetic scattering occurs near $(1,0)_O$, while in tetragonal

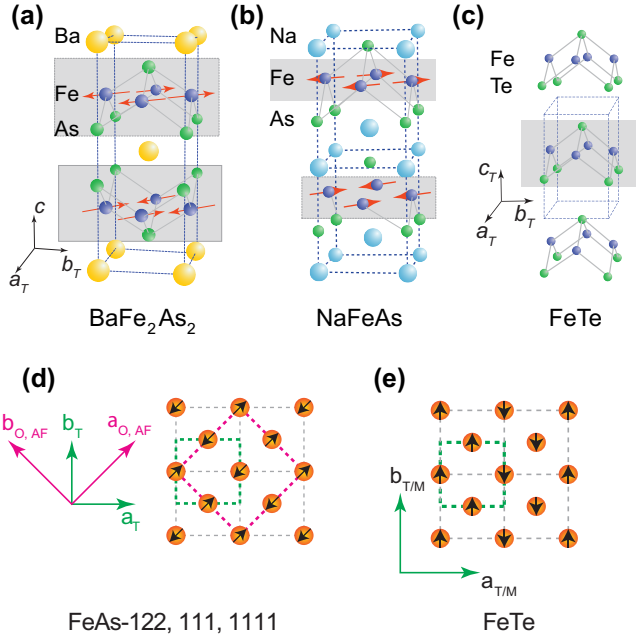

FIGURE 13 The crystal structures of (a) $BaFe_2As_2$, (b) NaFeAs, and (c) FeTe. The dashed lines indicate the tetragonal chemical unit cell, and arrows are ordered moments in the magnetically ordered state. (d) In-plane magnetic structure of iron pnictides including 122, 111, and 1111 compounds. The green (dark gray in print versions) dashed box is the tetragonal chemical unit cell, and the dashed magenta (gray in print versions) box is the orthorhombic chemical unit cell. The ordered moments are aligned along the a_O direction. (e) In-plane magnetic structure for FeTe, the green (dark gray in print versions) dashed line is the chemical unit cell for both the tetragonal and monoclinic phases.

notation this position becomes $(0.5,0.5)_T$. In systems that are tetragonal and in orthorhombic systems due to twinning, magnetic signal is also seen at $(0,1)_O$.

FeTe is also tetragonal at room temperature, below $\sim$70 K the system orders magnetically accompanied by a structural transition. Below the structural transition temperature FeTe changes to a weakly monoclinic structure, with $a_M > b_M$ and $\beta < 90°$. The magnetic order in FeTe has a bicollinear structure as shown in Figure 13(e), in this unit cell magnetic order occurs at $(0.5,0)_T$, and the spins are oriented along b_M. In FeTe samples an additional complicating factor is the presence of excess Fe, a small amount of which is necessary to stabilize the structure, therefore, the actual chemical composition is $Fe_{1+x}Te$. For $x < 0.12$ the system adopts the commensurate magnetic order in Figure 13(e) with a weakly monoclinic crystal structure. For $x > 0.12$ the magnetic order instead becomes incommensurate, characterized by the wave vector $(0.5 - \delta,0,0.5)_T$ and the crystal structure becomes orthorhombic [99]. For $FeTe_{1-x}Se_x$, with increasing Se doping the amount of excess Fe decreases,

and in superconducting samples excess Fe is no longer an issue of concern (Figure 12(b)). In stark contrast to the parent compounds of iron pnictides, Fermi-surface nesting is absent in FeTe and suggests that the magnetic order originates from local moments. However, it has been argued that the magnetic order in the absence of Fermi-surface nesting in FeTe can still be reproduced with itinerant models involving d_{xz}/d_{yz} orbitals [100].

In contrast to the cuprates, the magnetic form factor in iron pnictides is isotropic and agrees with that of metallic iron [101]. The ordered moments in the parent compounds of iron pnictides are smaller than 1 μ_B. Such values are smaller than the predictions from density functional theory (DFT), but calculations combining with dynamical mean field theory (DMFT) yields a much better agreement [102]. This highlights the fact that iron pnictides reside in the intermediate coupling regime and that neither a fully local nor a fully itinerant picture is sufficient to describe the underlying physics. Alternatively, it has been proposed that the small-ordered moment observed by neutron diffraction is due to local structural variations [103]. The ordered moment size in FeTe is $\sim 2\ \mu_B$, suggesting it is a more localized system compared to the iron pnictides [92].

Similar to the cuprates, measurements of high-energy spin waves can be done with the incident neutron beam parallel to the *c*-axis on chopper time-of-flight instruments. In such a geometry, L cannot be independently varied but is determined by incident energy, energy transfer, and momentum transfer in the *ab* plane. If the magnetism in iron pnictides is truly 2D as in the cuprates, this method can unequivocally obtain the complete magnetic response for all energy transfers. If the magnetism is 3D, and the magnetic signal is sharp in reciprocal space, it is possible to choose energy transfers that correspond to either zone center or the zone boundary along L and determine if there is significantly L dependence. This was done for nearly optimal-doped $Ba(Fe_{0.935}Co_{0.065})_2As_2$ and no L dependence was found for $E > 10$ meV, demonstrating the magnetic excitations are essentially L independent for this compound [104]. For the parent compounds, the spin-anisotropy gaps depend on L. For $BaFe_2As_2$, the spin-anisotropy gap is 10 meV for the magnetic zone center ($L = 1$) and 20 meV for the zone boundary ($L = 0$) [105]. For NaFeAs, the gap size is 5 meV for the magnetic zone center ($L = 0.5$) and 7 meV for the zone boundary ($L = 0$) [106]. For LaFeAsO, the gap is ~ 10 meV for both the magnetic zone center ($L = 0.5$) and zone boundary ($L = 0$) [107]. Since the L dependence of the spin-anisotropy gap is essentially determined by interlayer coupling J_c [107], these results suggest that the magnetism in LaFeAsO is more 2D than NaFeAs, which in turn is more 2D than $BaFe_2As_2$. It should also be noted that these results are obtained using triple-axis spectrometers where L can be independently varied, whereas estimates from time-of-flight measurements with $\mathbf{k_i}$ parallel to *c*-axis are not sensitive to J_c [108,109].

Spin waves in the entire Brillouin zone have been mapped out for $BaFe_2As_2$ [108], $CaFe_2As_2$ [110], $SrFe_2As_2$ [111], and NaFeAs [109]. As can be seen in Figure 14(e), the spin waves emanate from $(1,0)_O$ and disperse

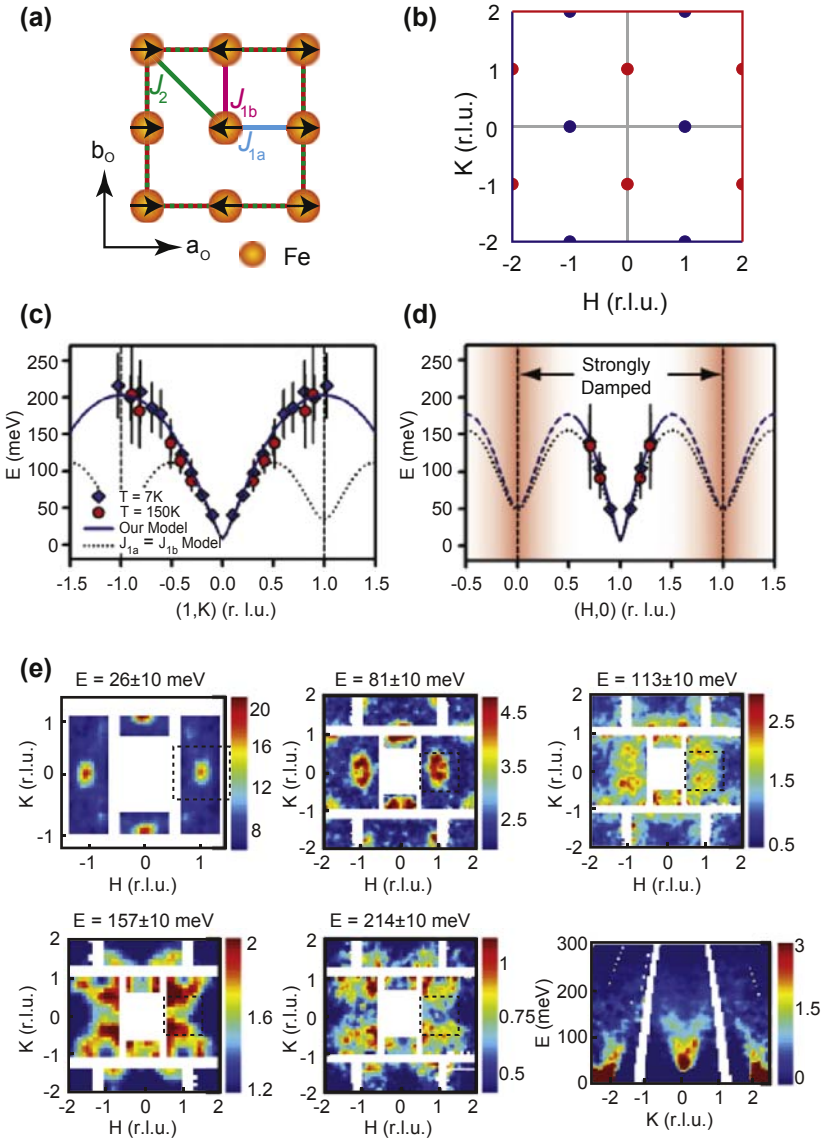

FIGURE 14 Spin waves in $BaFe_2As_2$. *Adapted with permission from Ref. [108].* (a) The in-plane magnetic structure of $BaFe_2As_2$ and definition of effective exchange couplings. (b) The magnetic Bragg peaks in reciprocal space, the blue (dark gray in print versions) points are Bragg peaks for the structure in (a), and the red (gray in print versions) points are from domains rotated by 90° from (a), the notation in reciprocal space corresponds to the orthorhombic chemical unit cell in (a) enclosed in the green (light gray in print versions) box. (c) The dispersion of spin waves along the transverse direction centered at (1,0,*L*), the solid line represents a model with $J_{1a} \neq J_{1b}$, and the dashed line is the model with $J_{1a} = J_{1b}$. Similarly, the dispersion along the longitudinal direction centered at (1,0,*L*) is shown in (d). (e) Constant-*E* slices of time-of-flight data for $BaFe_2As_2$, the spin waves emanate from (1,0) and disperse toward (1,1) with a bandwidth over 200 meV.

toward $(1,1)_O$, the spin-wave velocity along the longitudinal direction is higher than that along the transverse direction. The results can be interpreted using Heisenberg models with effective exchange interactions (Figure 14(a)). For $BaFe_2As_2$, the obtained exchange couplings are $SJ_{1a} = 59(2)$ meV, $SJ_{1b} = -9(1)$ meV, and $SJ_2 = 14(1)$ meV. It should be noted that SJ can be directly obtained by fitting spin waves measured by neutron scattering, and only when S is known as in the case of parent compounds of cuprates, J can be determined. In the case of iron-based superconductors, SJ is typically reported. Within the Heisenberg model, the larger spin-wave velocity along the longitudinal direction than the transverse direction is due to $J_{1a} + J_{1b} > 0$ [94]. Anisotropic nearest-neighbor exchange with $J_{1a} \neq J_{1b}$ is also necessary to account for the observed spin-wave dispersion as shown in Figure 14(c), whereas a model with isotropic exchange interactions does not correctly account for the magnetic band top being at $(1,1)_O$. Given the metallic nature of the parent compounds, spin waves are expected to be damped by particle-hole excitations in large portions of the Brillouin zone in contrast to La_2CuO_4 for which the spin waves are only damped possibly by interactions with spinon pairs near (1/2,0) [20]. As can be seen in Figure 14(e), the spin waves at low energies near $(1,0)_O$ are well defined, and with increasing energy they become more diffuse. This can be understood by calculating particle-hole excitation spectra which is weak near $(1,0)_O$ [112]. Experimentally, damping of spin waves is accounted for by using an empirical form [108–110]. Alternatively, the spin waves can also be interpreted using a Heisenberg model with isotropic J_1 and J_2 by adding a biquadratic coupling of the form $-K(S_i \cdot S_j)^2$ [113–115]. Compared to the Heisenberg model with anisotropic exchange, this model can also account for the magnetic excitations in the tetragonal paramagnetic state [30,111].

The spin waves can also be understood using itinerant models. For $SrFe_2As_2$, it was argued that the magnetic excitations are better explained by a five-band itinerant mean-field model [111]. However, calculations using the random-phase approximation (RPA) within a purely itinerant model to calculate the spin excitations cannot reproduce the local magnetic susceptibility in $BaFe_2As_2$ (see Section 3.3.4), whereas DMFT can qualitatively reproduce the local susceptibility [116], stressing the importance of electronic correlations in understanding the magnetism in iron pnictides. Compared to the 122 parent compounds, the magnetic excitations in NaFeAs are qualitatively the same except that their bandwidth is much narrower suggesting that NaFeAs is more correlated [102,109]. $CaFe_2As_2$ presents an intriguing case where under external pressure (or internal strain field due to FeAs precipitates) both the magnetic order and spin waves completely disappear as the system enters the so-called collapsed tetragonal phase where the c-axis lattice parameter is significantly reduced [117]. NMR [118] and DFT + DMFT [119] calculations suggest that in the collapsed tetragonal phase, electron correlations are suppressed, and $CaFe_2As_2$ becomes a good metal with suppressed spin correlations.

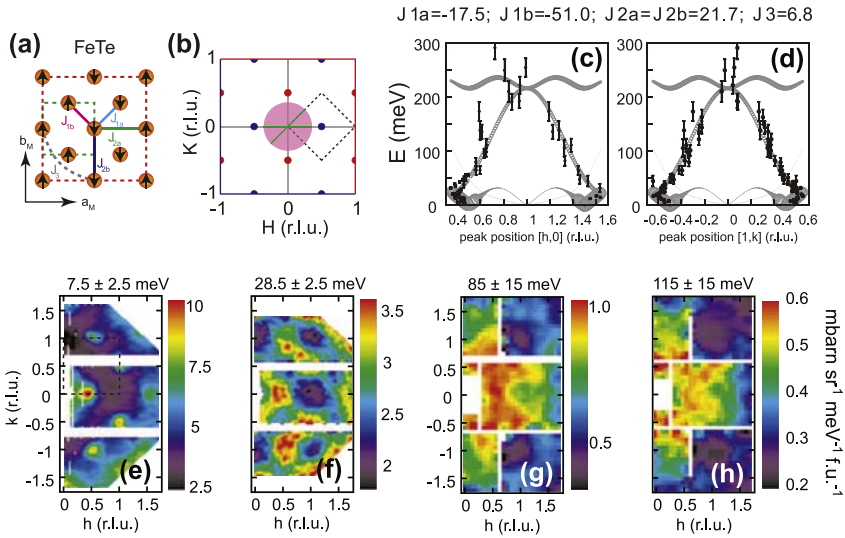

FIGURE 15 Spin waves in FeTe. *Adapted with permission from Ref. [120].* (a) The in-plane collinear commensurate magnetic structure of FeTe and definition of effective exchange couplings. (b) The magnetic Bragg peaks in reciprocal space, the blue (dark gray in print versions) points are Bragg peaks for the structure in (a), and the red (gray in print versions) points are from domains rotated by 90° from (a). The notation in reciprocal space corresponds to the monoclinic chemical unit cell in (a) enclosed in the green (light gray in print versions) box. (c) and (d) show the dispersion extracted from the data, the gray circles are the dispersion expected from the Heisenberg model using parameters above panels (c) and (d). (e—h) show constant energy slices of spin waves in FeTe. Above 85 meV, the excitations become diffuse.

Spin waves in FeTe have also been mapped out for samples with 5% [120] and 10% [121] excess Fe. The magnetic excitations can be fit with a Heisenberg model with anisotropic nearest-neighbor exchange interactions (Figure 15(a)) [120]. However, the spin waves become very diffuse above 85 meV (Figure 15). In another experiment, the magnetic excitations in FeTe were interpreted as correlations of liquidlike spin plaquettes [121]. Interestingly, the effective moment was found to increase with increasing temperature suggesting that local moments become entangled with itinerant electrons at low temperatures via a Kondo-type mechanism. It should be noted that excess Fe significantly affects low-energy magnetic excitations [122]. FeTe with ∼6% excess Fe orders at $(1/2,0,1/2)_T$, and spin waves emanating from this wave vector have a 7 meV spin gap, while samples with 14% excess Fe exhibit gapless magnetic excitations stemming from the incommensurate magnetic ordering wave vector $(0.38,0,1/2)_T$. While the low-energy spectral weight in $Fe_{1.14}Te$ is stronger than $Fe_{1.06}Te$, the total moment obtained by considering both elastic and inelastic spectral weight are similar [123]. The commensurate and incommensurate magnetism compete with each other as demonstrated

in $Fe_{1.08}Te$, below T_N the magnetism is commensurate with a spin gap while above T_N incommensurate magnetic excitations are seen [124].

3.3.3 Evolution of Magnetic Order and Magnetic Excitations with Doping

Starting from the parent compounds of the iron pnictides, the ordered moments become smaller, and T_N decreases with increasing doping. The orthorhombicity $\delta = (a_O - b_O)/(a_O + b_O)$ for the tetragonal-to-orthorhombic structural transition becomes smaller and T_S also decreases. Therefore, it becomes challenging to study the evolution of the magnetic order and the structural transition near the region where magnetic order and superconductivity coexists (Figure 12(a)), especially with powder samples. Therefore, although the phase diagrams for 1111 compounds were the first to be mapped out [94], the majority of detailed studies in the region where superconductivity coexists with antiferromagnetic order have been performed on doped 122 single crystals. Doping Co or Ni at Fe sites in $BaFe_2As_2$ splits the magnetic and the structural transition while both transitions are driven toward lower temperatures (Figure 12(a)). Increasing doping further, the magnetic order changes from long-range commensurate to transverse-split short-range incommensurate in a first-order fashion (Figure 16(c)) [125,126]. The incommensurate magnetic order was argued to be a hallmark of magnetism driven by a spin-density-wave instability [125], recent results from NMR and neutron resonant spin-echo measurements [127–129] instead suggest that the incommensurate short-range magnetic order is due to formation of a cluster spin-glass phase. In this scenario, the disappearance of short-range magnetic order with increasing doping corresponds to the disappearance of volume fraction for the spin-glass phase [128,129]. In the underdoped region of the phase diagram where superconductivity coexists with magnetic order, it was found that superconductivity competes with magnetic order, whether it is long-range commensurate (Figure 16(a)) or short-range incommensurate order (Figure 16(b)) [126,129,130]. Since the long-range magnetic order from the parent compound disappears through a first-order transition to the short-range incommensurate order phase, there is no quantum critical point in the conventional sense [131]. Application of a magnetic field suppresses superconductivity and enhances magnetic order for both commensurate long-range order [132] and incommensurate short-range order (Figure 16(c)) [126]. However, there is no report of field-induced magnetic order in a sample which does not order under zero field as in $La_{2-x}Sr_xCuO_4$ [35]. Compared to Co and Ni, doping Cu in $BaFe_2As_2$ does not induce incommensurate magnetic order near the putative quantum critical point [133]. Although similar to the former cases, long-range magnetic order also disappears through a phase with short-range magnetic order without a quantum critical point.

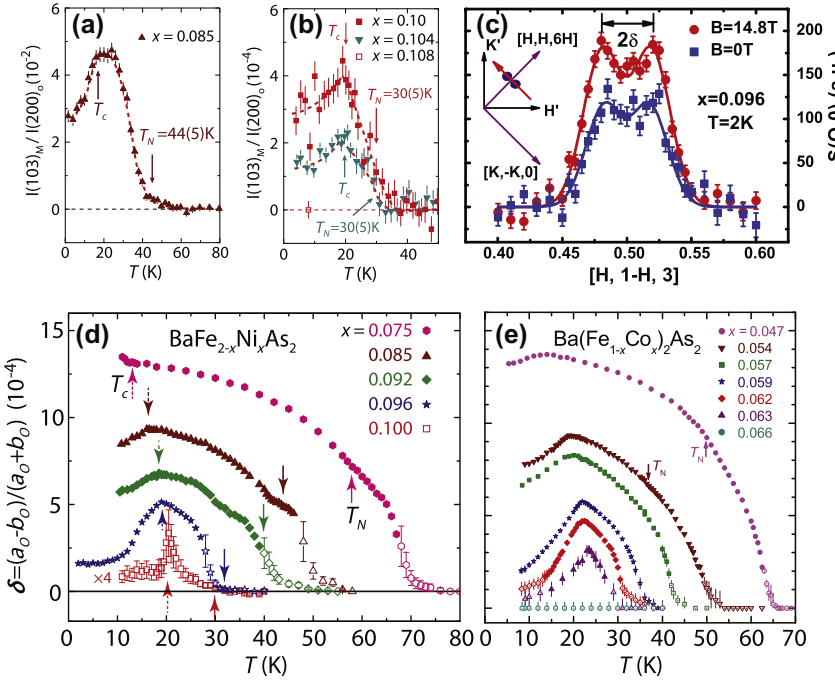

FIGURE 16 Evolution of magnetic order and structural distortion in $BaFe_{2-x}Ni_xAs_2$ and $Ba(Fe_{1-x}Co_x)_2As_2$. (a) The magnetic order parameter in $BaFe_{2-x}Ni_xAs_2$ with $x = 0.085$ which shows long-range commensurate magnetic order, below T_c the magnetic order is suppressed [131]. (b) The magnetic order parameter for $BaFe_{2-x}Ni_xAs_2$ with $x = 0.1$, 0.104, and 0.108. Samples $x = 0.1$ and 0.104 exhibit short-range incommensurate magnetic order, and no magnetic ordering is seen in the sample with $x = 0.108$ [131]. (c) Effect of an applied magnetic field on the short-range incommensurate magnetic order in $BaFe_{2-x}Ni_xAs_2$ with $x = 0.096$. The inset shows the geometry of the experimental setup [126]. (d) Orthorhombicity for $BaFe_{2-x}Ni_xAs_2$, clear suppression of orthorhombicity is seen below T_c, but does not reenter the tetragonal state [131]. (e) Orthorhombicity for $Ba(Fe_{1-x}Co_x)_2As_2$, reenters tetragonal state for samples with $x = 0.063$ [134]. *Adapted with permission from Refs [126,131,134].*

In the underdoped region where superconductivity coexists with antiferromagnetic order in the orthorhombic state, the onset of superconductivity suppresses orthorhombicity (Figure 16(d) and (e)) [131,134]. In the case of $Ba(Fe_{1-x}Co_x)_2As_2$ for critical doping ($x = 0.063$), the system changes from tetragonal to orthorhombic at T_S and then reenters the tetragonal state below T_c. In the case of $BaFe_{2-x}Ni_xAs_2$, similar behavior is seen but no reentrance behavior was observed, even though for samples with $x = 0.096$ and 0.1 the orthorhombicity becomes temperature independent at the lowest temperatures measured (Figure 16(d)) [131]. The suppression of orthorhombicity is suggested to be a result of magnetoelastic coupling [134], therefore it is a secondary effect linked to the competition between magnetic order and superconductivity.

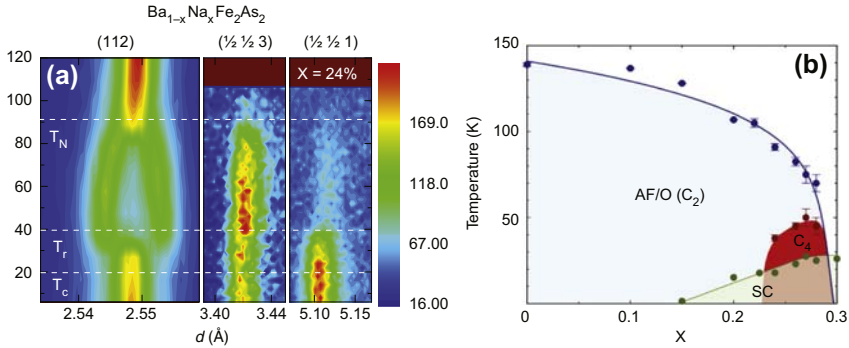

FIGURE 17 Reentrant tetragonal phase in $Ba_{1-x}Na_xFe_2As_2$. *Adapted with permission from Ref. [135].* (a) Temperature scans of the structural peak (1,1,2) and magnetic peaks (1/2,1/2,3) and (1/2,1/2,1) in $Ba_{1-x}Na_xFe_2As_2$ with $x = 0.24$. The reentry temperature is marked as T_r, the magnetic peaks show significant change in intensity below T_r suggesting possible spin reorientation. (b) The phase diagram for $Ba_{1-x}Na_xFe_2As_2$ showing reentrant phase with C_4 rotational symmetry with magnetic order, the reentry temperature occurs above T_c. SC, superconducting.

Doping holes in $BaFe_2As_2$ by substituting Ba with K and Na also induces superconductivity while suppressing magnetic order, however, the magnetic ordering transition temperature T_N and the structural transition temperature T_S do not split with doping, and superconductivity is achieved at a much higher doping level with a superconductivity dome that spans a much larger region (Figure 12(a)). For $Ba_{1-x}Na_xFe_2As_2$, reentry into the tetragonal state was also found (Figure 17) [135]. In contrast to $Ba(Fe_{1-x}Co_x)_2As_2$, the reentry occurs above T_c. The reentry to the tetragonal state is possibly accompanied by a reorientation of magnetic moments (Figure 17(a)) [135]. The presence of magnetic order in tetragonal $Ba_{1-x}Na_xFe_2As_2$ favors the presence of a magnetic Ising-nematic state [91].

Doping Mn and Cr at Fe sites in $BaFe_2As_2$ does not split the magnetic and structural transitions nor induces superconductivity. In the phase diagram for $Ba(Fe_{1-x}Cr_x)_2As_2$, while the stripe magnetic order from $BaFe_2As_2$ is suppressed at low Cr concentrations, checkerboard magnetic order (characterized by the ordering wave vector $(1,1)_O$) appears for doping levels $x > 0.3$ (Figure 18(a)) [136]. The phase diagram for $Ba(Fe_{1-x}Mn_x)_2As_2$ is similar [137,138]. For Mn doping levels $x > 0.1$, it was found that the system enters a Griffiths-type phase before the stripe magnetic order associated with $BaFe_2As_2$ is completely suppressed. Therefore, Mn dopants act as strong local magnetic impurities [138]. In $Ba(Fe_{1-x}Mn_x)_2As_2$ with $x = 0.075$ which exhibit only stripe magnetic order, Neel-type magnetic excitations at $(1,1,L)$ are seen suggesting such magnetic fluctuations compete with stripe magnetic fluctuations [139]. Isovalent doping P at As sites or Ru at Fe sites in $BaFe_2As_2$ also suppresses magnetic order. In these cases, the structural transition temperature T_S remains coincident with the magnetic

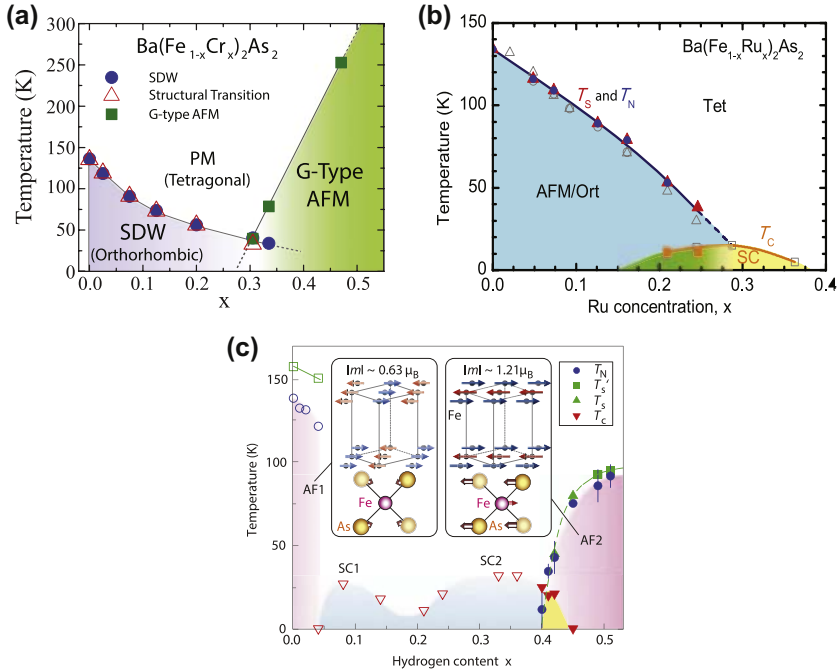

FIGURE 18 Magnetic phase diagram of Cr-doped [136] and Ru-doped [230] $BaFe_2As_2$ and H-doped LaFeAsO [143]. (a) In $Ba(Fe_{1-x}Cr_x)_2As_2$, stripe magnetic order is suppressed with Cr doping up to ∼30% and then G-type magnetic order appears [136]. (b) In $Ba(Fe_{1-x}Ru_x)_2As_2$, T_N and T_S remain coincident for all doping levels, and superconductivity is induced at ∼20% Ru doping [230]. (c) In $LaFeAsO_{1-x}H_x$, two superconductivity domes associated with two magnetically ordered phases are observed, the two magnetically ordered end compounds have different magnetic structures and order moments [143]. *Adapted with permission from Refs [136,143,230].*

transition temperature T_N, and superconductivity is induced for ∼20% dopants. $BaFe_2(As_{1-x}P_x)_2$ is especially interesting because of the numerous reports of a quantum critical point [140] in this system [141]. However, results from single-crystal neutron diffraction suggest magnetic order in this system also disappears in a weakly first-order fashion [142]. An interesting case occurs when electron dopant H is introduced into LaFeAsO, superconductivity forms two domes and for doping levels ∼50%, another magnetically ordered phase appears (Figure 17(c)) [143]. The second magnetically ordered phase also exhibits stripe order, but compared to LaFeAsO it is ferromagnetic along c-axis and the moments are perpendicular to the stripe direction. The two superconductivity domes derived from two separate ordered phases highlight the connection between magnetism and superconductivity.

For spin excitations, upon doping Ni in $BaFe_2As_2$ the immediate effect is to suppress the spin-anisotropy gap and, therefore, the c-axis coupling present in the parent compound [144]. The low-energy magnetic excitations centered at

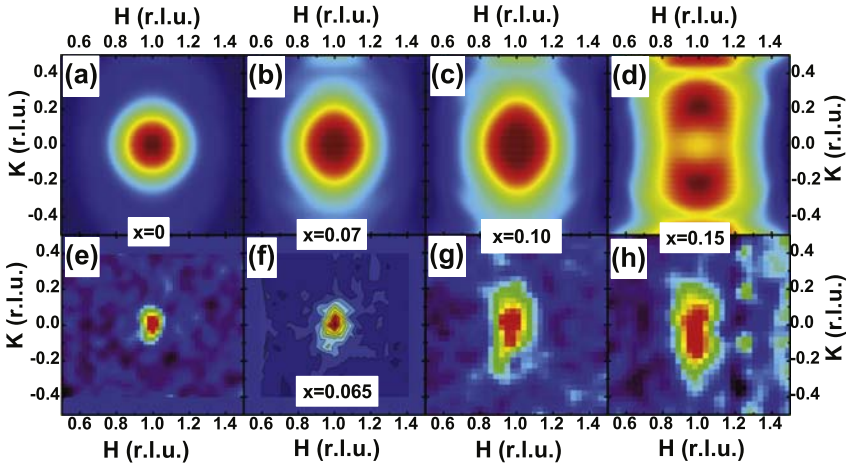

FIGURE 19 Evolution of low-energy magnetic excitations in $BaFe_{2-x}Ni_xAs_2$ at $E = 8$ meV. *Adapted with permission from Ref. [145].* (a–d) random-phase approximation calculations. (e–h) Neutron scattering measurements. The qualitative agreement suggests the low-energy excitations can be ascribed to itinerant electrons.

$(1,0)_O$ broaden along both the longitudinal and the transverse directions but with a higher rate along the transverse direction. The evolution of low-energy magnetic excitations with doping can be qualitatively reproduced by calculations using the RPA favoring an itinerant origin of low-energy magnetic excitations (Figure 19) [145]. Remarkably, doping K at Ba site in $BaFe_2As_2$ results in the low-energy magnetic excitations becoming longitudinally elongated at optimal doping (Figure 20(a)) [146], in agreement with weak coupling model predictions [147]. Further K doping results in two split peaks situated at $(1 \pm \delta,0)$ in overdoped $Ba_{1-x}K_xFe_2As_2$ [148] and KFe_2As_2 (Figure 20(b)) [149].

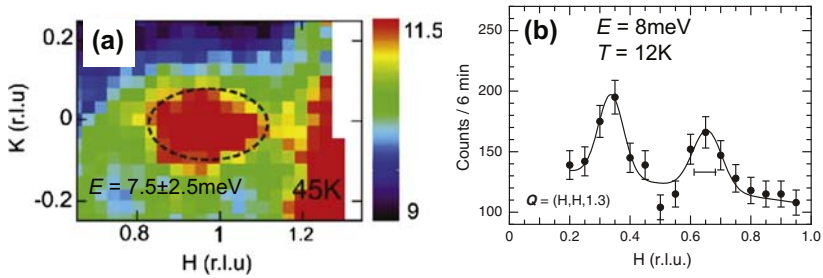

FIGURE 20 Evolution of low-energy magnetic excitations in $Ba_{1-x}K_xFe_2As_2$. (a) In optimal doped $Ba_{0.67}K_{0.33}Fe_2As_2$, the low-energy magnetic excitations become longitudinally elongated, rotated by 90° compared to electron-doped $BaFe_2As_2$. *Adapted with permission from Ref. [146].* (b) In KFe_2As_2, magnetic excitations split into two peaks along the longitudinal direction. *Adapted with permission from Ref. [149].*

Interestingly in $SrCo_2As_2$, magnetic excitations are found to be centered at $(1,0)_O$ but are longitudinally elongated [150] resembling K-doped rather than Co-/Ni-doped $BaFe_2As_2$ [145]. It is not clear how such an evolution occurs as Co gradually replaces Fe in $SrFe_2As_2$.

Doping Se in FeTe suppresses static magnetic order and causes magnetic spectral weight to be transferred from $(0.5,0)_T$ to $(0.5,0.5)_T$ near optimal doping [151,152]. Therefore, in superconducting $FeTe_{1-x}Se_x$ compounds, magnetic excitations are situated at the same wave vector as in the iron pnictides. Coexistence of magnetic excitations at $(0.5,0)_T$ and near $(0.5,0.5)_T$ is found over a wide doping range for $FeTe_{1-x}Se_x$. With increasing Se content, magnetic excitations at $(0.5,0)_T$ are suppressed while those at $(0.5,0.5)_T$ are enhanced [153–155]. In moderately Se-doped $FeTe_{1-x}Se_x$, low-energy magnetic excitations are found at $(0.5,0)_T$ while at higher energies the spectral weight transfers to incommensurate peaks transversely split around $(0.5,0.5)_T$ [153,156]. Increasing Se to $\sim$50%, the magnetic response becomes commensurate at $(0.5,0.5)_T$ [157]. The magnetic excitations in $FeTe_{1-x}Se_x$ are compared for nonsuperconducting doping $x = 0.27$ and superconducting doping $x = 0.49$ in Figure 21 [156]. For $E = 6$ meV, the magnetic excitations in $FeTe_{0.73}Se_{0.27}$ are centered at $(0.5,0)_T$ (Figure 21(a)) but at higher energies become transversely split incommensurate peaks centered around $(0.5,0.5)_T$ (Figure 21(b)). In $FeTe_{0.51}Se_{0.49}$, the corresponding magnetic excitations are transversely elongated commensurate peaks centered at $(0.5,0.5)_T$ (Figure 21(f) and (g)). However, the high-energy magnetic excitations are similar in the two compounds (Figure 21(c–e) and (h–k)). These results suggest that the appearance of superconductivity in $FeTe_{1-x}Se_x$ is accompanied by the appearance of low-energy magnetic excitations around $(0.5,0.5)_T$. The appearance of superconductivity and magnetic fluctuations at $(0.5,0.5)_T$ in superconducting $FeTe_{1-x}Se_x$ is significant since this corresponds to the nesting wave vector [158], suggesting that despite the different magnetic ground state of FeTe and parent compounds of iron pnictides, similar magnetic fluctuations are found in superconducting compounds of both systems [154]. In Cu-doped $Fe_{1-x}Cu_xTe_{0.5}Se_{0.5}$, low-energy magnetic excitations are enhanced and resistivity of the system resembles an insulator rather than a metal. However, it is not clear whether the enhanced magnetic excitations are due to a redistribution of high-energy spectral weight or an enhanced magnetic moment [159].

LiFeAs represents an oddity among iron-pnictide parent compounds as it does not order magnetically and instead becomes superconducting below $T_c = 18$ K. Low-energy magnetic excitations in LiFeAs form transversely split incommensurate peaks (Figure 22(a)) [160,161], similar to electron overdoped 122 compounds. While the absence of static magnetic order in LiFeAs differs from other parent compounds, the low-energy magnetic excitations agree with Fermi-surface measurements using angle-resolved photoemission spectroscopy (ARPES) [162]. Given the Fermi surface of LiFeAs, two possible nesting

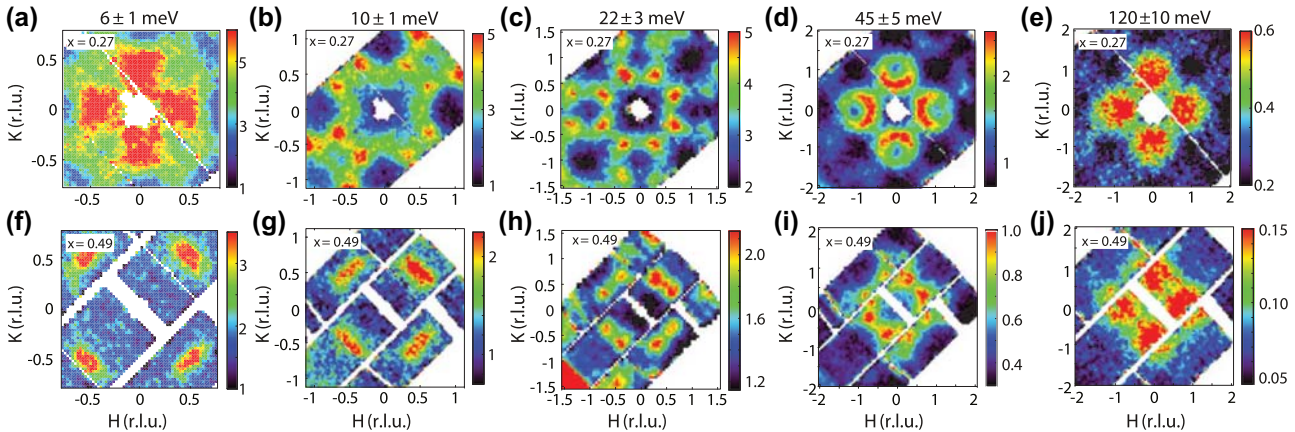

FIGURE 21 Comparison of magnetic excitations in $FeTe_{1-x}Se_x$ with $x = 0.27$ and $x = 0.49$. *Adapted with permission from Ref. [156].* (a–e) Constant-E slices for $FeTe_{1-x}Se_x$ with $x = 0.27$. (f–j) Identical slices for $x = 0.49$.

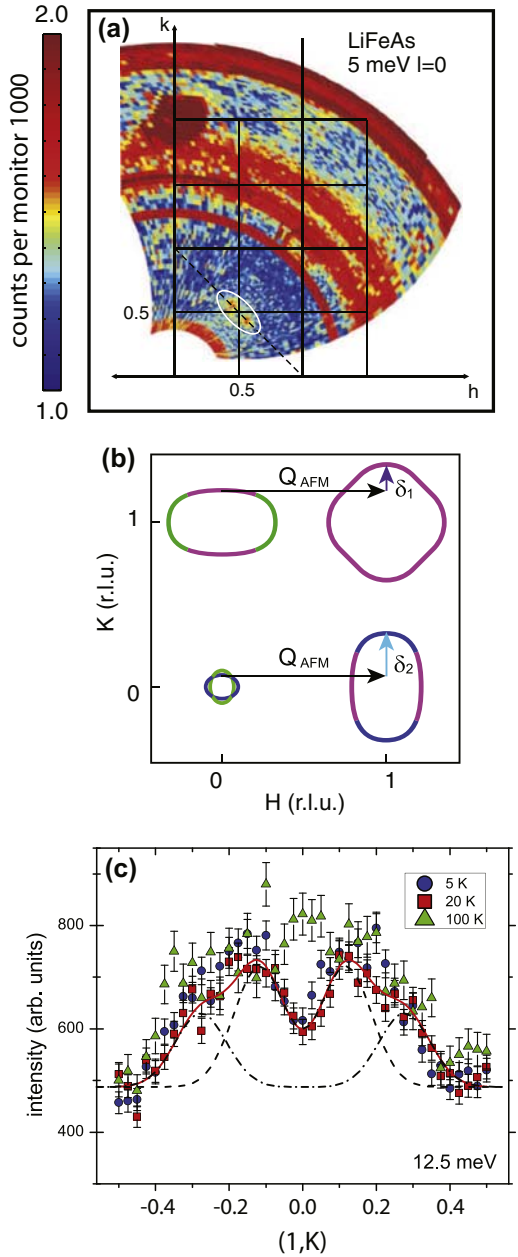

FIGURE 22 Magnetic excitations in LiFeAs. (a) Transverse split incommensurate peaks found in LiFeAs [161]. Here, tetragonal notation is used where $(0.5,0.5)_T$ correspond to $(1,0)_O$ in orthorhombic notation. (b) Fermi surface of LiFeAs from angle-resolved photoemission spectroscopy where two possible nesting vectors are possible [162]. (c) The magnetic excitations can be described by two pairs of incommensurate peaks, suggesting both nesting conditions in (b) give rise to magnetic fluctuations [163]. *Adapted with permission from Refs [161,163].*

wave vectors are possible (Figure 22(b)) and signature for two pairs of incommensurate split peaks are seen experimentally from inelastic neutron scattering (Figure 22(c)) [163].

3.3.4 Persistence of High-Energy Magnetic Excitations

The systematic evolution of magnetic excitations with electron doping has been studied for $BaFe_{2-x}Ni_xAs_2$ (Figure 23) [76,108,116,164]. At low energies, sharp spin waves in $BaFe_2As_2$ become ellipses elongated along the transverse direction while high-energy magnetic excitations remain similar. For $BaFe_{1.7}Ni_{0.3}As_2$, low-energy magnetic excitations are completely suppressed below $\sim$50 meV (Figure 23(u–v)) [76] while high-energy magnetic excitations persist. The persistence of high-energy magnetic excitations in

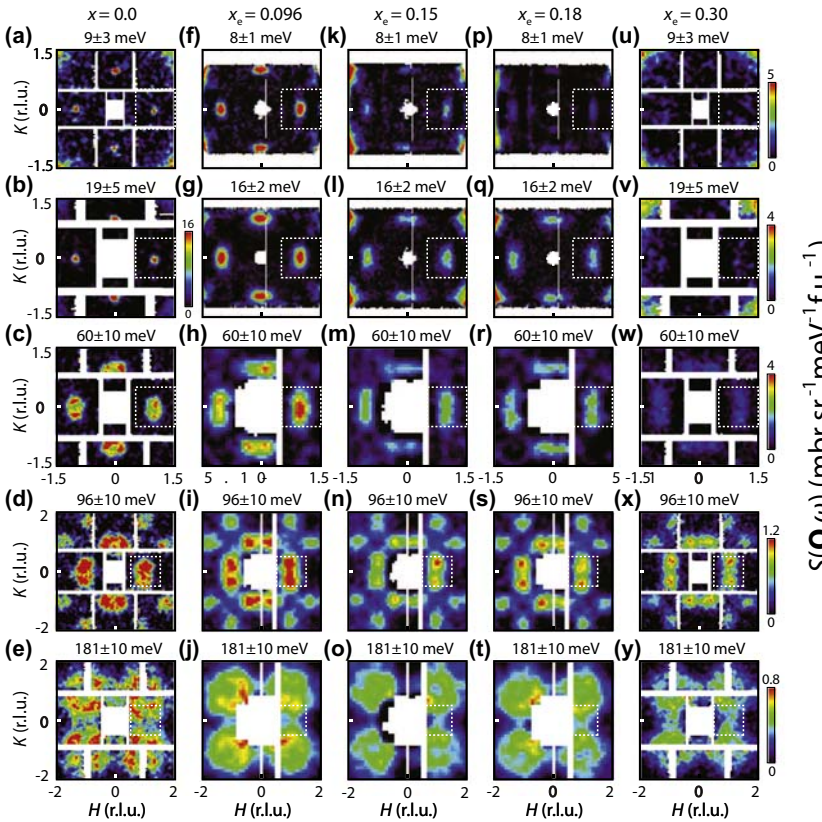

FIGURE 23 Evolution of high-energy magnetic excitations in $BaFe_{2-x}Ni_2As_2$. (a–e) $BaFe_2As_2$ [108]. (f–j) $BaFe_{1.904}Ni_{0.096}As_2$ [164]. (k–o) $BaFe_{1.85}Ni_{0.15}As_2$ [164]. (p–t) $BaFe_{1.82}Ni_{0.18}As_2$ [164]. (u–y) $BaFe_{1.7}Ni_{0.3}As_2$ [76].

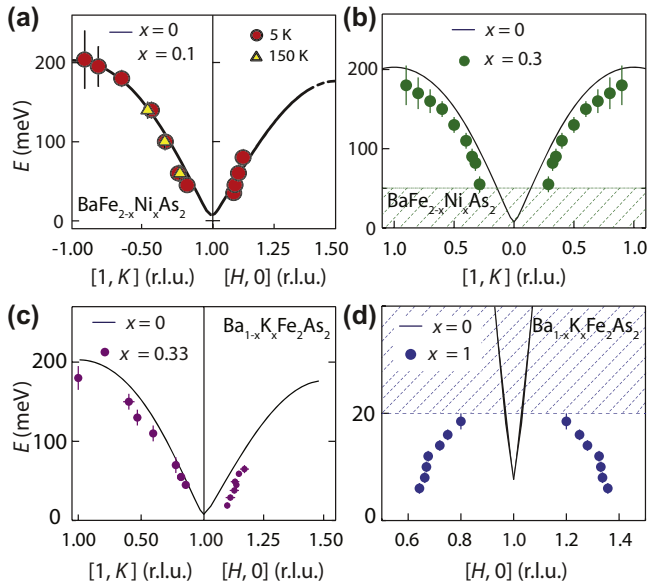

FIGURE 24 Doping dependence of the dispersion of magnetic excitations in $BaFe_2As_2$ compared with undoped $BaFe_2As_2$ (solid black line). (a) $BaFe_{1.9}Ni_{0.1}As_2$ [116]. (b) $BaFe_{1.7}Ni_{0.3}As_2$ [76]. (c) $Ba_{0.67}K_{0.33}Fe_2As_2$ [76]. (d) KFe_2As_2 [76].

$BaFe_{2-x}Ni_xAs_2$ contrasts with what was observed in hole-doped cuprates, where with increasing doping magnetic excitations are strongly suppressed (Figure 8(b)). The dispersion of magnetic excitations in $BaFe_{2-x}Ni_xAs_2$ with $x = 0.1$ and 0.3 only slightly softens compared to $BaFe_2As_2$ (Figure 24(a) and (b)). A similar persistence of magnetic excitations is also seen in $Ba_{0.67}K_{0.33}Fe_2As_2$ (Figure 24(c)) but in KFe_2As_2 only low-energy magnetic excitations are seen (Figure 24(d)). Based on these results, it was argued that in electron-/hole-doped $BaFe_2As_2$, low-energy magnetic excitations originate from nested Fermi surfaces, whereas high-energy magnetic excitations are due to short-range local magnetic correlations [76]. In this picture, the persistence of high-energy magnetic excitations can be understood since they are not sensitive to doping, and the large spin gap in $BaFe_{1.7}Ni_{0.3}As_2$ is due to the suppression of itinerant magnetism. It is still not clear how the large spin gap in $BaFe_{1.7}Ni_{0.3}As_2$ opens with increasing doping: Is the spectral weight below $\sim$50 meV gradually suppressed or does the gap increase in size with increasing doping? More work is needed to clarify this issue.

To quantitatively trace the evolution of magnetic spectral weight with doping, it is useful to calculate the local susceptibility, defined as

$$\chi''(E) = \int \chi''(\mathrm{Q}, E)\mathrm{dQ} \Big/ \int \mathrm{dQ},$$

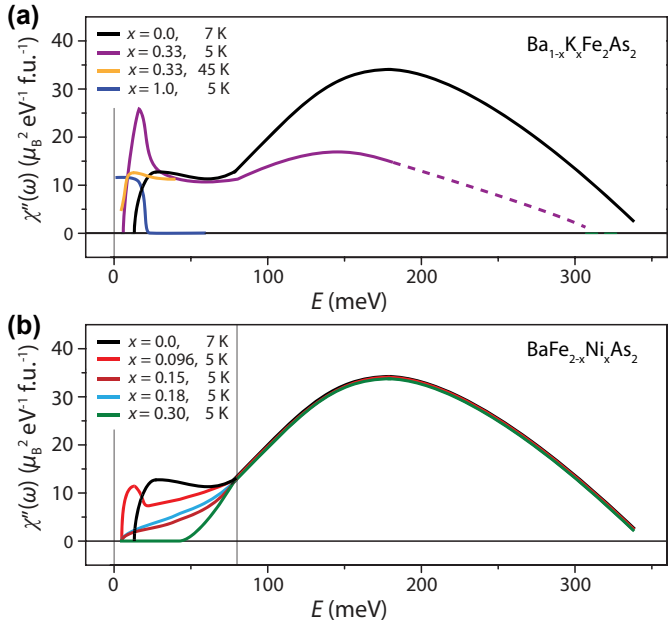

FIGURE 25 The local susceptibility for $Ba_{1-x}K_xFe_2As_2$ and $BaFe_{2-x}Ni_xAs_2$ shown in units of $\mu_B{}^2$/eV/formula unit [14]. (a) $Ba_{1-x}K_xFe_2As_2$. (b) $BaFe_{2-x}Ni_xAs_2$.

where in practice the integration should be carried over an area large enough such that the average is equivalent to the average over the whole reciprocal space [104]. The local susceptibility therefore represents the overall strength of magnetic fluctuations and by integrating the local susceptibility over energy one obtains the total fluctuating moment through

$$\langle m^2 \rangle = \frac{3\hbar}{\pi} \int \frac{\chi''(E)\mathrm{d}E}{1 - \exp\left(-\frac{\hbar\omega}{k_B T}\right)}.$$

The local susceptibility has been studied using time-of-flight neutron spectroscopy for $Ba_{1-x}K_xFe_2As_2$ and $BaFe_{2-x}Ni_xAs_2$ [14], and results are summarized in Figure 25. For $Ba_{1-x}K_xFe_2As_2$, the low-energy local susceptibility is significantly modified with doping. For optimal doped $Ba_{0.67}K_{0.33}Fe_2As_2$, there is a strong resonance mode in the superconducting state ($T_c = 38$ K). As in the cuprates, while the resonance is the most prominent feature in the magnetic excitation spectrum, it accounts for only a small part of the total spectral weight. The effect of K doping on high-energy magnetic excitations seems to be a gradual suppression of spectral weight, which strongly contrasts with Ni doping where high-energy magnetic excitations persist. The total fluctuating moment for $BaFe_2As_2$ is estimated to be $\sim 3.6\ \mu_B{}^2$/Fe [30] and with Ni doping it gradually decreases to $\sim 2.8\ \mu_B{}^2$/Fe in $BaFe_{1.7}Ni_{0.3}As_2$ [164]. The fluctuating

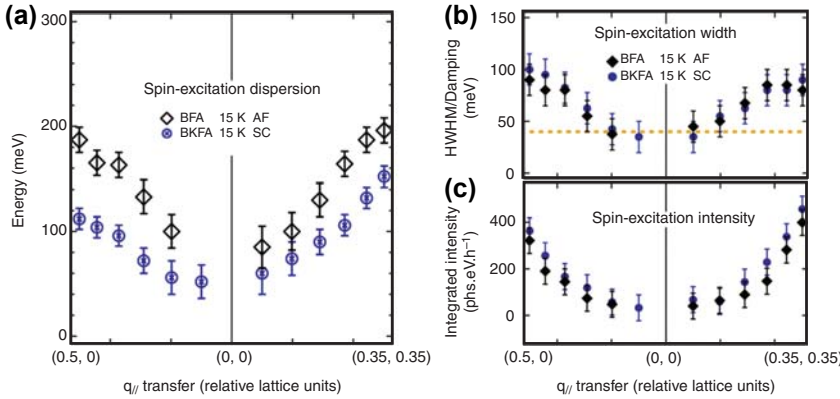

FIGURE 26 Magnetic excitations in $BaFe_2As_2$ (BFA) and $Ba_{0.6}K_{0.4}Fe_2As_2$ (BKFA) seen by resonant inelastic X-ray scattering [19]. (a) The dispersion of magnetic excitations in the two compounds. (b) The widths of excitations, the dashed line represents instrument resolution. (c) The intensity of magnetic excitations. *Adapted with permission from Ref. [19].*

moment in $Ba_{0.67}K_{0.33}Fe_2As_2$ and KFe_2As_2 reduces to $\sim 1.7\ \mu_B{}^2$/Fe and $0.1\ \mu_B{}^2$/Fe, respectively [76], within the energy range when data are currently available.

The persistence of high-energy magnetic excitations is also seen by RIXS in $Ba_{0.6}K_{0.4}Fe_2As_2$ (Figure 26) [19]. Compared to neutron scattering results [76], RIXS also sees a softening of magnetic excitations with K doping (Figure 26(a)) but the persistence of intensity with K doping disagrees with neutron scattering results (Figure 26(c)). This discrepancy is similar to what was observed in the cuprates, where neutrons saw significant suppression of spectral weight but RIXS saw persistence of magnetic intensity. Similar to the case of the cuprates, neutron scattering measures magnetic signals near $(1,0)_O$ and RIXS measures near (0,0) (magnetic spectral weight is concentrated near $(1,0)_O$), dispersion of spin waves are identical for these two points in the magnetically ordered parent compounds but with the suppression of magnetic order these two points are no longer equivalent. Neutron scattering and RIXS therefore provide complementary information on how spin waves evolve from magnetically ordered parent compounds to magnetic excitations in the superconducting compounds.

3.3.5 The Resonance Mode in Iron-Based Superconductors

Soon after the discovery of superconductivity in the iron pnictides, a resonance mode was found in $Ba_{1-x}K_xFe_2As_2$ [68]. Later, it was confirmed in many other iron pnictides [161,165–170]. The resonance-mode intensity tracks the superconductivity order parameter and forms in the superconducting state by shifting spectral weight from lower energies so a spin gap also opens in the superconducting state. In the electron-underdoped regime where superconductivity

and antiferromagnetic order coexist, the static order is suppressed when entering the superconducting state so the corresponding spectral weight also shifts to the resonance mode [130,165]. The resonance mode in underdoped iron pnictides centered at $(1,0)_O$ disperses both along c [171] and b [172], but is sharply peaked along a. The dispersion along L becomes weaker with increasing doping, but remains dispersive in overdoped compounds [168,173]. The dispersion of the resonance mode is due to 3D spin correlations in the antiferromagnetically ordered parent compounds. Moving away from antiferromagnetic order well past optimal doping, the resonance becomes dispersionless (Figure 27(a)) [168]. Alternatively, the dispersion of the resonance in doped

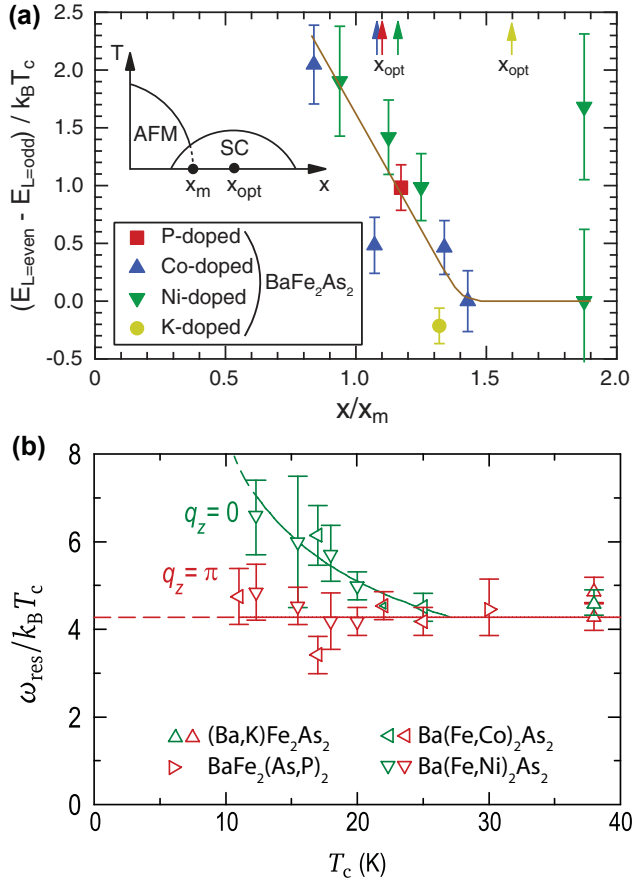

FIGURE 27 Dispersion along c of the resonance mode in doped $BaFe_2As_2$. (a) Dispersion along c becomes weaker when moving further away from $BaFe_2As_2$ [168]; x_m is the critical doping level where magnetic order disappears. (b) Alternatively, the dispersion along c may depend on T_c. In samples with smaller T_c, the dispersion becomes stronger [174]. *Adapted with permission from Refs [168,174].*

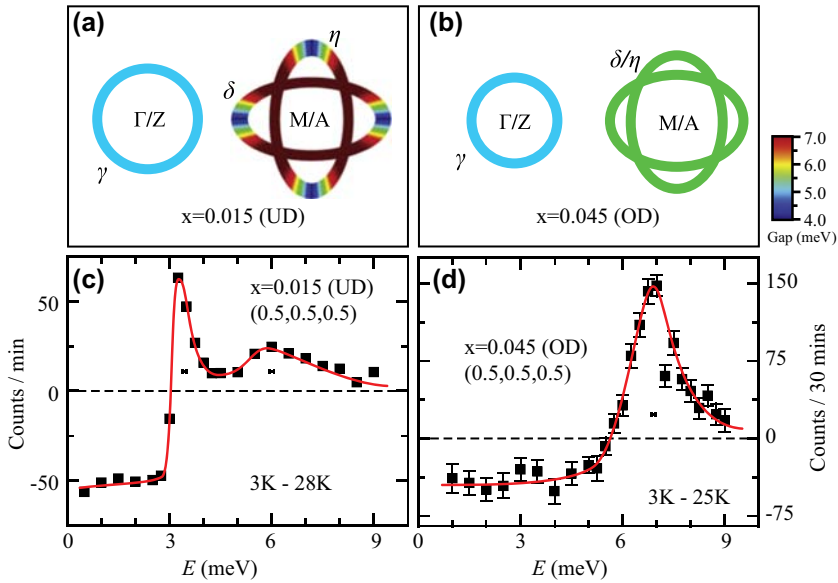

FIGURE 28 Double-resonance mode in underdoped $NaFe_{0.985}Co_{0.015}As$ and single-resonance mode in overdoped $NaFe_{0.955}Co_{0.045}As$ [170] seen in neutron scattering experiments. (a) Schematic diagram of the anisotropic superconducting gap as indicated by the color scale in underdoped $NaFe_{0.985}Co_{0.015}As$. (b) Schematic of the isotropic superconducting gap in overdoped $NaFe_{0.955}Co_{0.045}As$. (c) Double resonance found in underdoped $NaFe_{0.985}Co_{0.015}As$. (d) Single resonance found in overdoped $NaFe_{0.955}Co_{0.045}As$. *Adapted with permission from Ref. [170].*

$BaFe_2As_2$ has been argued to be related to T_c, with samples with lower T_c exhibiting a stronger dispersion (Figure 27(b)) [174]. With increasing doping, the resonance splits along the transverse direction for $BaFe_{1.85}Ni_{0.15}As_2$ [145].

While the resonance in iron pnictides is mostly interpreted as a spin-exciton with $s\pm$ pairing symmetry where the superconductivity order parameter changes sign on different Fermi surfaces [2,83], the broad resonance mode observed in 122 compounds [146,175] led to the proposals of orbital-mediated $s{+}{+}$ superconductivity (the superconductivity order parameter maintains the same sign on different Fermi surfaces) in the iron pnictides [176,177]. The sharp resonance found in both overdoped (Figure 28(d)) [169] and underdoped $NaFe_{1-x}Co_xAs$ (Figure 28(c)) [170] ruled out the $s{+}{+}$ scenario since the $s{+}{+}$ scenario can only account for broad resonance modes. Intriguingly, in underdoped $NaFe_{1-x}Co_xAs$, two resonance modes were found [170]. The origin of the double resonance is still under debate. It may be due to anisotropy of the superconducting gap for underdoped $NaFe_{1-x}Co_xAs$ which becomes isotropic for overdoped $NaFe_{1-x}Co_xAs$ (Figure 28(a) and (b)) [178] or the two resonances actually occur at different wave vectors (one at $(1,0)_O$ and the other at

$(0,1)_O$) but due to twinning they are simultaneously observed [179]. Inelastic neutron scattering experiments on detwinned samples are needed to determine the origin of the double resonance.

A resonance mode has also been reported in superconducting LiFeAs [161]. Similar to the normal-state magnetic excitations, the resonance mode is also incommensurate. Neutron resonance modes are also found in superconducting $FeTe_{1-x}Se_x$ [152,157,180]. While the normal-state magnetic excitations can be transversely split centered at $(0.5,0.5)_T$, the resonance mode is commensurate at $(0.5,0.5)_T$ (Figure 29) [157].

3.3.6 Magnetism in $A_xFe_{2-y}Se_2$ (A = Alkali Metal or Tl) Compounds

The report in 2010 of superconductivity in $K_{0.8}Fe_2Se_2$ with $T_c \sim 30$ K initiated research on $A_xFe_{2-y}Se_2$ [181]. Initial neutron diffraction data suggested the coexistence of superconductivity with block antiferromagnetic order with the composition $A_{0.8}Fe_{1.6}Se_2$ (Figure 30(a)) [93]. Later, it became clear that superconducting $A_xFe_{2-y}Se_2$ samples are phase separated [182–184], and that block antiferromagnetism and superconductivity originate from different phases [185–188]. The parent phases have been proposed to be either $A_{0.8}Fe_{1.6}Se_2$ with block antiferromagnetic order (245 phase, Figure 30(a)) [93,189,190] or $AFe_{1.5}Se_2$ with stripe antiferromagnetic order and rhombus iron vacancy (122 phase, Figure 30(b)) [187], whereas the superconducting phase has the structure of the 122 phase but with disordered iron vacancies and no magnetic order [187,188]. Fe vacancies in $A_{0.8}Fe_{1.6}Se_2$ order at $T_S = 500–578$ K and Fe moments order at a slightly lower temperature $T_N = 471–559$ K with an ordered moment of $\sim 3.3\ \mu_B$/Fe (Figure 30 (a)) [190]. Magnetic moments in $KFe_{1.5}Se_2$ were found to order at $T_N \sim 280$ K with an ordered moment $\sim 2.8\ \mu_B$/Fe [187].

While insulating $K_xFe_{2-y}Se_2$ samples are made up entirely of the 245 phase, semiconducting and superconducting samples also contain a significant portion of the 122 phase. The 122 phase in the semiconducting sample orders magnetically but the 122 phase in superconducting samples do not. Furthermore, the magnetic order in the 122 phase resembles the magnetic order in the parent phase of iron pnictides (Figure 30(b)). Based on these results, it was suggested that the 122 phase with magnetic order is the actual parent compound from which superconductivity is derived [187]. It is worth noting that a similar phase separation of 245 and 122 phases is seen in $Rb_xFe_{2-y}S_2$. However, superconductivity is absent in this system [191].

Spin waves have been mapped out for block-ordered $Rb_{0.8}Fe_{1.6}Se_2$ (Figure 31(a–d)) [192], $(Tl,Rb)_{0.8}Fe_{1.6}Se_2$ [193], and $K_2Fe_4Se_5$ [194]. These results were analyzed using linear spin-wave theory. Two optical branches (Figure 31(a) and (b)) in addition to an acoustic branch are observed

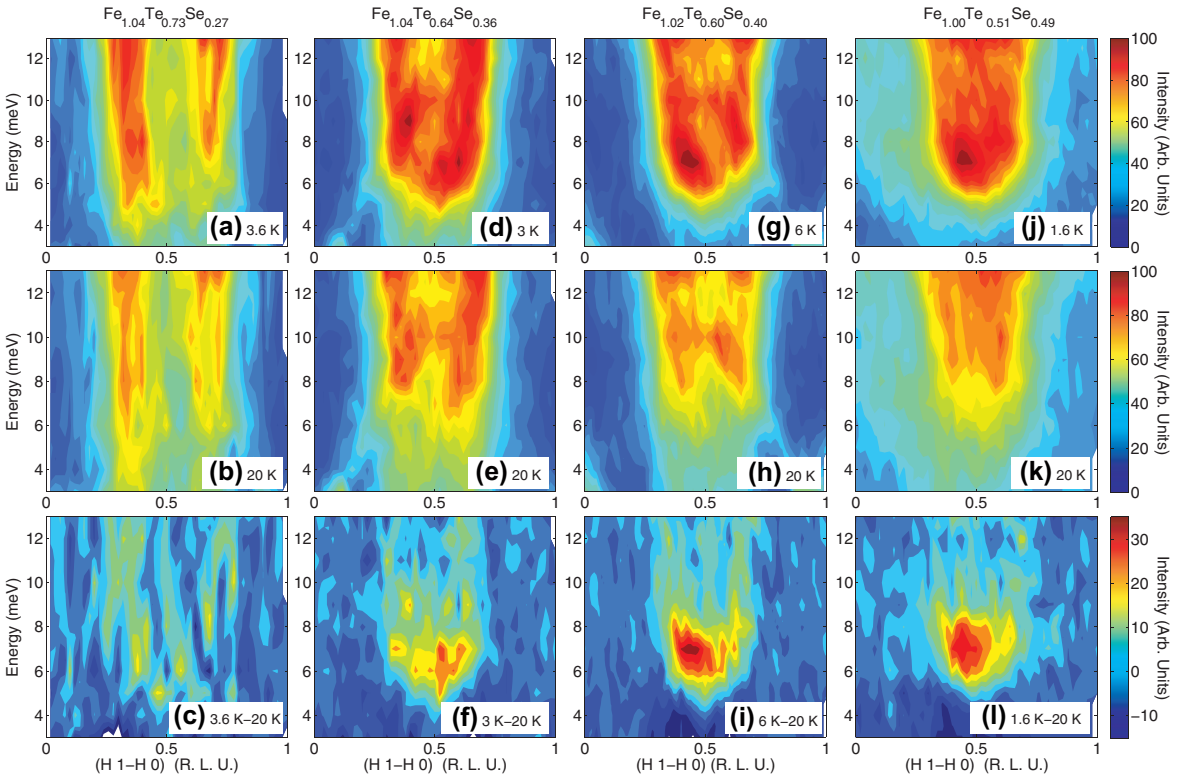

FIGURE 29 Low-energy magnetic excitations in $FeTe_{1-x}Se_x$ with $x = 0.27$ (a–c), 0.36 (d–f), 0.40 (g–i), and 0.49 (j–l). *Adapted with permission from Ref. [157].* The samples with $x = 0.27$ and 0.36 show filamentary superconductivity. For $x = 0.40$, $T_c = 13$ K and for $x = 0.49$, $T_c = 14$ K. While the response at 20 K may be commensurate or incommensurate, 3–20 K data are commensurate suggesting the resonance mode is commensurate.

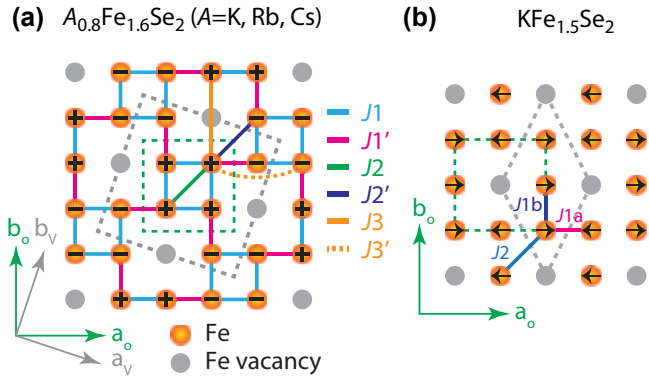

FIGURE 30 Fe vacancy order and magnetic order in (a) $A_2Fe_4Se_5$ (A = K, Rb, Cs) and (b) $KFe_{1.5}Se$ [14]. The gray dashed box in (a) is the structural and magnetic unit cell for the $A_2Fe_4Se_5$ phase.

(Figure 31(c)), which can also be seen by examining the local susceptibility (Figure 31(d)). The fluctuating moment is found to be $\langle m^2 \rangle \sim 16\ {\mu_B}^2/\text{Fe}$. Considering that the ordered moment is $\sim 3\ \mu_B/\text{Fe}$, the total moment can be determined from

$$M_{\text{total}}^2 = M_{\text{ord}}^2 + \langle m^2 \rangle,$$

resulting in a total moment $M_{\text{tot}}^2 \sim 25\ {\mu_B}^2/\text{Fe}$, consistent with $24\ {\mu_B}^2/\text{Fe}$ expected for Fe with $S = 2$ within experimental error [192]. In addition, the study of the temperature dependence of magnetic excitations in $Rb_{0.8}Fe_{1.6}Se_2$ found that contrary to $BaFe_2As_2$ [30], the magnetic excitations do not persist above T_N [195]. Magnetic excitations arising from the 122 phase have also been studied (Figure 31(e–h)). In this case, the spin waves form cones stemming from $(1,0)_O$ similar to the parent compounds of the iron pnictides [196]. While this evidence favors a superconducting state arising from doping of the magnetically ordered 122 phase, in $A_xFe_{2-y}Se_2$ the resonance mode associated with superconductivity does not appear at $(0.5,0.5)_T$ as in iron pnictides. Instead, the resonance in $Rb_xFe_{2-y}Se_2$ is found near $(0.5,0.25)_T$ at $E \sim 14$ meV (Figure 32(a)) [197], corresponding to the nesting wave vector between two electron pockets (Figure 32(c)) [198]. This finding is later confirmed by similar measurements in related systems [198–201]. The resonance is elongated along the transverse direction and does not disperse along c. Also, the resonance mode does not show the symmetry of the 245 phase clearly indicating it does not arise from the blocked ordered phase [198,199]. Since the resonance is believed to arise from quasiparticle excitations that are enhanced when the superconducting gaps connected by the resonance wave vector have opposite signs [83], the Fermi surface of

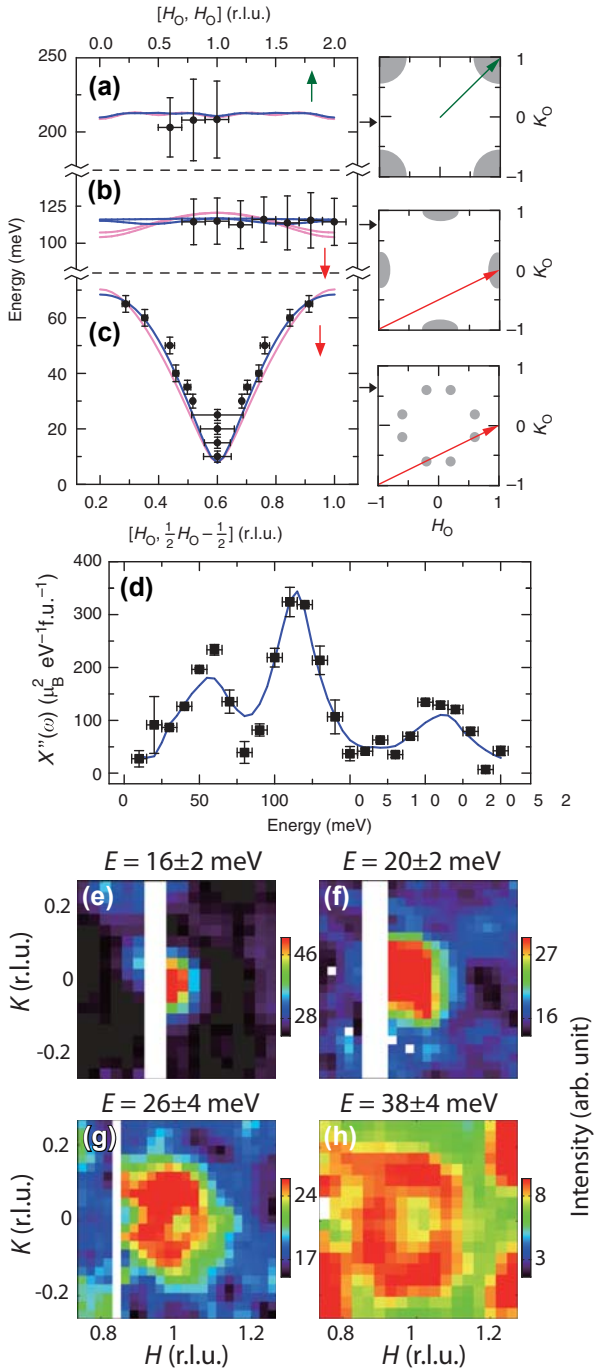

FIGURE 31 Spin waves in the 245 and 122 phases of $A_xFe_{2-y}Se_2$. (a and b) Optical and (c) acoustic branches of spin waves in $Rb_{0.8}Fe_{1.6}Se_2$ [192]. The blue (dark gray in print versions) solid lines are for a spin wave model with $J_3 > 0$, and pink (light gray in print versions) solid lines are for $J_3 = 0$. The dispersion curves are along directions shown to the right of each panel. (d) Local susceptibility of $Rb_{0.8}Fe_{1.6}Se_2$ [192]. The solid line is the calculated local susceptibility based on a spin wave model. (e–h) Constant-E slices of spin waves from the 122 phase of $K_xFe_{2-y}Se_2$ [196]. *Adapted with permission from Refs [192,196].*

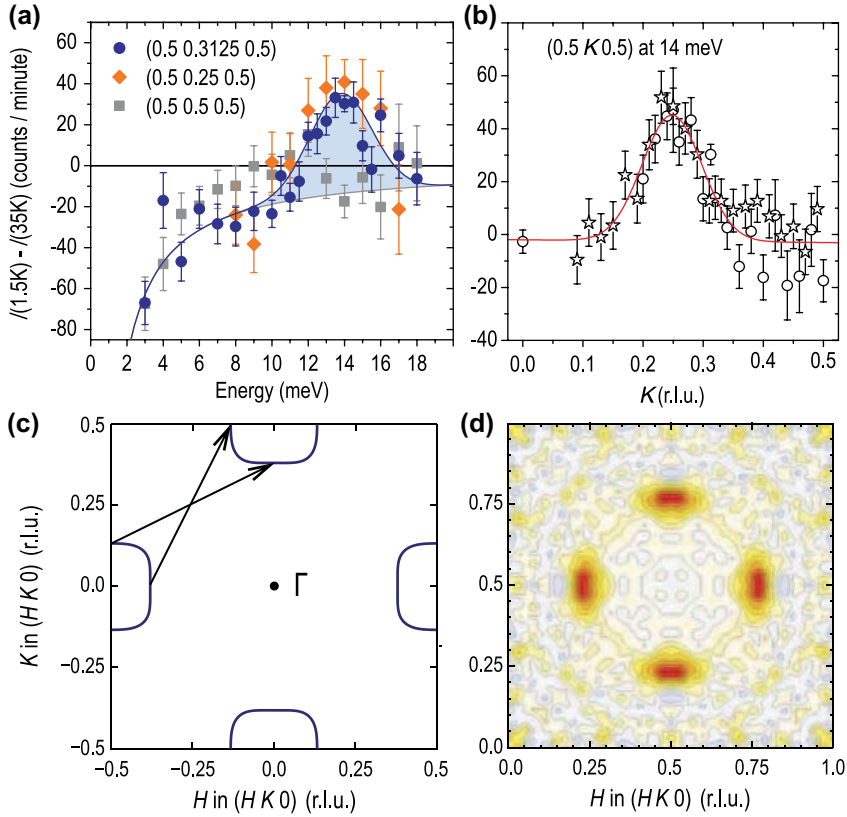

FIGURE 32 The resonance mode in $A_xFe_{2-y}Se_2$. (a) 1.5−35 K data for constant-**Q** scan of the resonance mode in $Rb_xFe_{2-y}Se_2$ with $T_c = 32$ K [197]. (b) 1.5−35 K data for constant energy scan of the resonance mode [197]. (c) Possible nesting wave vector that connects the two electron Fermi surfaces corresponding to the resonance wave vector [198]. (d) *H-K* map at $E = 15$ meV for $Rb_xFe_{2-y}Se_2$ [198]. *Adapted with permission from Refs [197,198].*

$A_xFe_{2-y}Se_2$ (Figure 32(c)) suggests that superconductivity has *d*-wave symmetry rather than $s\pm$ as in the superconducting iron pnictides.

3.3.7 Polarization Dependence of Low-Energy Magnetic Excitations

By polarizing the incident neutron beam and analyzing the scattered neutrons with a particular spin direction, it becomes possible to study the polarization dependence of magnetic excitations [17]. It is typically useful to choose three such directions *x*, *y*, and *z*, to be parallel and perpendicular to the scattering vector **Q** in the scattering plane and perpendicular to the scattering plane, respectively. Since the polarization of the magnetic signal

has to be perpendicular to **Q** and the neutron-polarization direction for spin-flip scattering, the spin-flip scattering cross sections are [202]:

$$\sigma_{xx}^{\mathrm{SF}} \sim M_y + M_z + B^{\mathrm{SF}}$$
$$\sigma_{yy}^{\mathrm{SF}} \sim M_z + B^{\mathrm{SF}}$$
$$\sigma_{zz}^{\mathrm{SF}} \sim M_y + B^{\mathrm{SF}}$$

M_i is the magnetic signal polarized along i and B^{SF} is the background for spin-flip scattering. Similarly for non-spin-flip scattering the cross sections are:

$$\sigma_{xx}^{\mathrm{NSF}} \sim B^{\mathrm{NSF}}$$
$$\sigma_{yy}^{\mathrm{NSF}} \sim M_y + B^{\mathrm{NSF}}$$
$$\sigma_{zz}^{\mathrm{NSF}} \sim M_z + B^{\mathrm{NSF}}$$

B^{NSF} is the non-spin-flip background. By measuring all three cross sections (either spin-flip or non-spin-flip), M_y and M_z can be unequivocally determined. Doing the same at an equivalent wave-vector position in another Brillouin zone allows M_a, M_b, and M_c to be determined when effects of instrumental resolution can be estimated [106,202–204].

In optimal doped $YBa_2Cu_3O_{6+x}$, polarized neutron scattering experiments found that the normal state response and the resonance mode are isotropic in spin space (i.e., $M_y = M_z$), but low-energy magnetic excitations in the superconducting state are anisotropic with magnetic excitations polarized along c being suppressed [205]. Another advantage of using polarized neutrons in $YBa_2Cu_3O_{6+x}$ is that it allows the magnetic signal to be separated from phonons which overlap with the magnetic signal. However, so far there are a limited number of such studies in the cuprates possibly due to the weak magnetic signal of the cuprates and reduced flux for polarized experiments.

In $BaFe_2As_2$, significant spin anisotropy was found [204,206]. The spin waves polarized along c have a smaller gap than those polarized in-plane, suggesting that it costs more energy to rotate spins in the ab-plane than perpendicular to it [206]. More interestingly, longitudinal magnetic excitations that cannot be explained using spin-wave theory are also observed, highlighting the contribution of itinerant electrons to magnetism in the iron pnictides (Figure 33(a–b)) [204]. Similar anisotropy is also found in NaFeAs, but with smaller spin-anisotropy gaps (Figure 33(c–d)) [106]. Upon electron doping in $BaFe_2As_2$ and NaFeAs, a similar anisotropy is found to persist even when antiferromagnetic order is suppressed [202,203,207,208], and magnetic excitations become isotropic only well on the overdoped side of the phase diagram [202,209]. For $Ba_{1-x}K_xFe_2As_2$, significant anisotropy exists in optimal and overdoped samples [210,211]. Remarkably, using polarized neutron scattering, it was found that the broad resonance mode in near-optimal doped $Ba(Fe_{0.94}Co_{0.06})_2As_2$ consists of two parts, a low-energy component polarized along c and a higher-energy isotropic component (Figure 34(a–b)) [208].

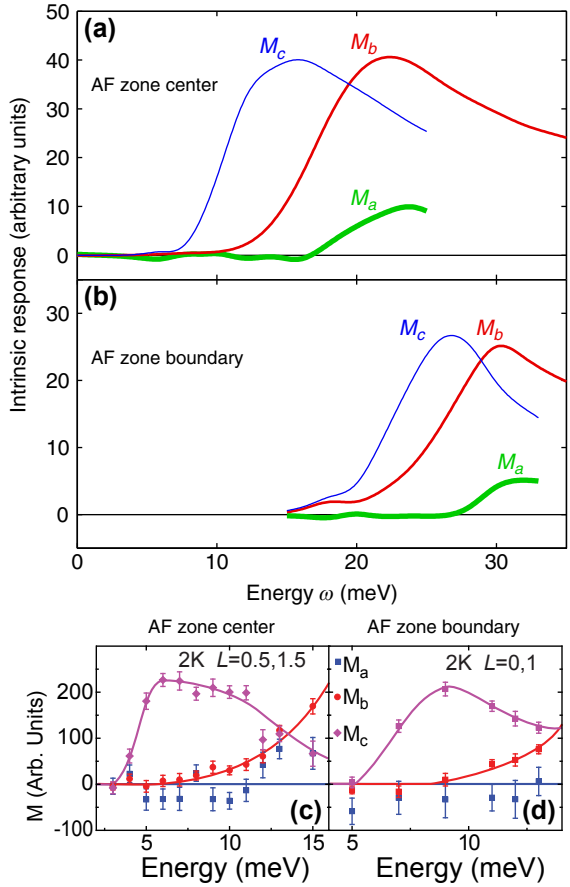

FIGURE 33 Polarization of spin waves in $BaFe_2As_2$ [204] and NaFeAs [106]. (a) The spin waves in $BaFe_2As_2$ at the magnetic zone center. (b) The spin waves in $BaFe_2As_2$ at the zone boundary along c. (c) The spin waves in NaFeAs at the magnetic zone center. (d) The spin waves in NaFeAs at the zone boundary along c. *Adapted with permission from Refs [106,204].*

Similar behavior is also seen in optimal (Figure 34(c−d)) [210] and slightly overdoped $Ba_{1-x}K_xFe_2As_2$ [211]. In underdoped $NaFe_{0.985}Co_{0.015}As$ with double resonances coexisting with antiferromagnetic order [170], the lower-energy resonance is anisotropic, but the resonance at higher energy is isotropic [202]. These findings suggest that the double resonance in $NaFe_{0.985}Co_{0.015}As$ [170] is actually a common feature of iron pnictides, but in other systems the two modes are too broad and merge into one in unpolarized neutron scattering experiments. The first resonance mode is dispersive along c and anisotropic, while the second resonance is isotropic in spin space and forms a flat band along c [170,202]. In-plane spin anisotropy in near-optimal doped $BaFe_{1.904}Ni_{0.096}As_2$ exists at $E = 3$ meV even in the paramagnetic tetragonal

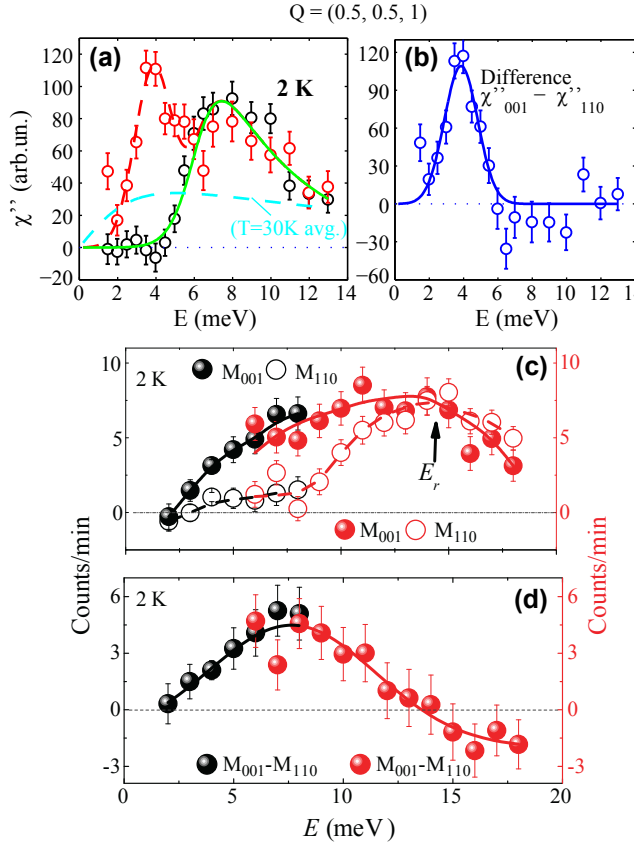

FIGURE 34 Polarization of magnetic excitations in near-optimal doped $Ba(Fe_{0.94}Co_{0.06})_2As_2$ [208] and optimal-doped $Ba_{0.67}K_{0.33}Fe_2As_2$ [210]. (a) In-plane and out-of-plane polarized magnetic excitations for $Ba(Fe_{0.94}Co_{0.06})_2As_2$ at 2 K. (b) The difference along the two directions. (c) Similar in-plane and out-of-plane polarized magnetic excitations for $Ba_{0.67}K_{0.33}Fe_2As_2$ at 2 K. (d) The difference along the two directions. *Adapted with permission from Refs [208,210].*

state but is enhanced in the superconducting state, while magnetic excitations at $E = 7$ meV are isotropic at all temperatures (Figure 35) [203]. This finding suggests that the anisotropy of the first resonance could be caused by electronic anisotropy or orbital ordering already present in the normal state. Weak spin anisotropy is also found in superconducting $FeTe_{1-x}Se_x$, with the in-plane component slightly larger than the out-of-plane component [212,213].

So far, there are few theoretical studies on the polarization of spin excitations in iron pnictides to explain the experimental observations. While the energy scale of spin anisotropy is small compared to exchange couplings in the parent compounds, spin anisotropy has an energy scale comparable to the resonance mode in many compounds and may be an important ingredient

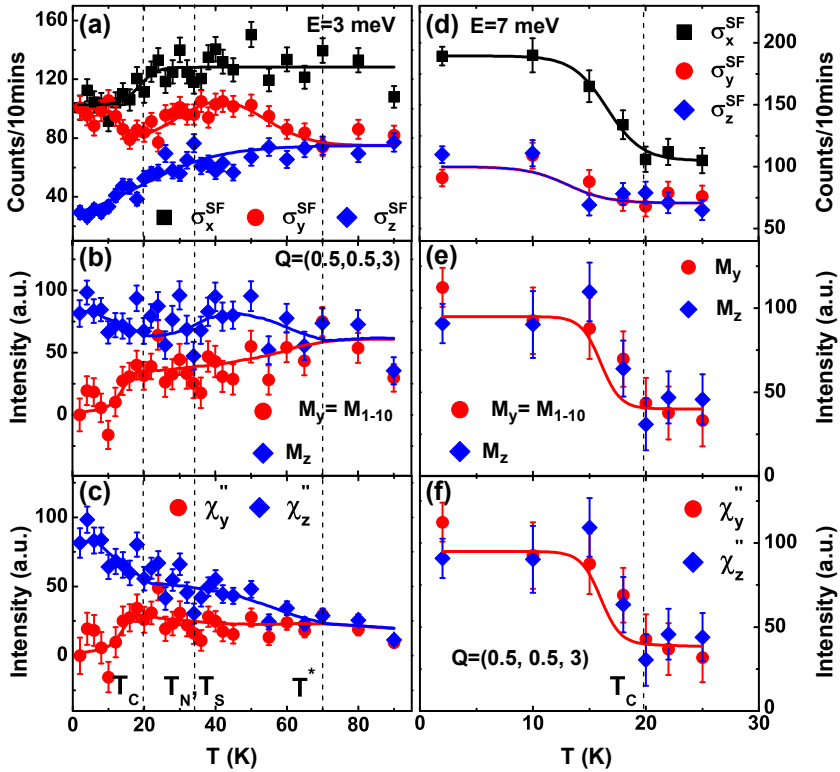

FIGURE 35 Polarization of magnetic excitations in near-optimal doped $BaFe_{1.904}Ni_{0.096}As_2$ [203]. (a) Cross sections for x, y, and z at (0.5,0.5,3) $E = 3$ meV. (b) M_y and M_z. (c) Susceptibility χ_y'' and χ_z'' which is related to M_y and M_z by the Bose factor. (d–f) Similar plots as (a–c) but for $E = 7$ meV.

for understanding the origin of superconductivity. Further experimental and theoretical efforts are needed to understand the polarization of low-energy magnetic excitations in both the cuprates and iron-based superconductors.

3.4 SUMMARY AND OUTLOOK

Superconductivity in both the cuprates and iron-based superconductors is derived from antiferromagnetically ordered parent compounds. However, whereas the parent compounds of cuprates are half-filled, single-band Mott insulators, the parent compounds of iron pnictides have multiple bands derived from several orbitals and are metallic. In both cases, strong magnetic excitations with a wide magnetic bandwidth are observed by neutron scattering. Whereas in hole-doped cuprates and iron pnictides, the magnetic excitations are suppressed with increasing doping, high-energy magnetic

excitations persist in electron-doped iron pnictides. In the superconducting state, resonance modes are found in both systems. While the resonance mode is the most prominent feature in the superconducting state, it accounts for a small fraction of the entire magnetic spectral weight, but nevertheless it is able to account for the superconductivity condensation energy.

An electronic nematic state that exists in iron pnictides has been the focus of considerable research [91]. However, due to structural twinning, limited progress has been made from a neutron scattering perspective. Neutron diffraction has been carried out on $Ba(Fe_{1-x}Co_x)_2As_2$ [214,215] and NaFeAs [98] by applying uniaxial pressure to detwin samples and found that uniaxial pressure can affect both T_S and T_N. Inelastic neutron scattering has also been done on detwinned $BaFe_{2-x}Ni_xAs_2$ under uniaxial pressure and found that anisotropy between $(1,0)_O$ and $(0,1)_O$ persists even above T_N, favoring a spin-nematic scenario for electronic nematicity [216]. By studying the spin−spin correlation length between T_S and T_N in twinned samples, anomalies in spin excitations between T_S and T_N also suggest a magnetic scenario for electronic nematicity [217]. Studies of magnetic excitations over the entire Brillouin zone using detwinned samples and in situ removal of uniaxial strain are needed to clarify the connection between electronic nematicity and magnetism in iron pnictides.

The strength of electronic correlations for the parent compounds of iron pnictides is in fact similar to superconducting cuprates [89]. Further, superconductivity can be induced in iron pnictides in almost every way that suppresses the antiferromagnetic ordering [94], whereas in the cuprates the route is much more specific. Based on these general results, an alternate view of the iron pnictides has been proposed (Figure 36) [218]. In this picture, the iron pnictides are also derived from a Mott insulating phase with strong electronic correlations when all Fe orbitals are half-filled ($n = 5$, corresponding to doping one hole to each Fe in $BaFe_2As_2$ with $n = 6$) and each band individually becomes Mott insulating [218−220]. For slightly higher fillings, the system is tuned to a selective Mott insulating state with different orbitals having different degrees of localization. The parent compounds then correspond to 20% doping, which in the cuprates is slightly overdoped (Figure 4). The strength of electronic correlations is found to increase from the electron-doped to the hole-doped side of the phase diagram for $BaFe_2As_2$ [218,221], culminating in KFe_2As_2 ($n = 5.5$) with a large mass enhancement close to a selective Mott transition [222]. In this picture, the magnetic order in the parent compounds corresponds to competing phases similar to stripe order in $La_{2-x}Ba_xCuO_4$, which naturally accounts for why superconductivity can be induced in numerous ways by suppressing magnetic order, and the similar strength of electronic correlations found in superconducting cuprates and parent compounds of iron pnictides. While this view is certainly tantalizing by putting the cuprates and iron pnictides on the same footing, experimental evidence for a Mott insulating phase with half-filled Fe orbitals would be desirable.

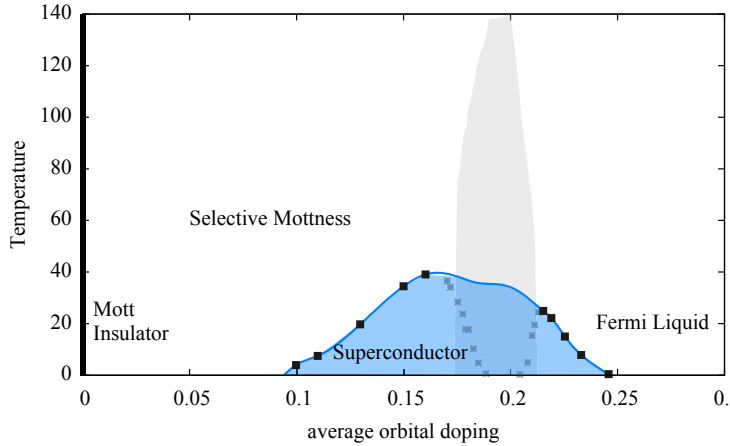

FIGURE 36 Proposal of unified phase diagram for iron pnictides and cuprates [218]. Zero doping correspond to a yet-to-be-discovered Mott insulating phase with half-filled ($n = 5$) Fe orbitals. 10% doping corresponds to KFe_2As_2 with $n = 5.5$, and 20% doping corresponds to $BaFe_2As_2$ ($n = 6$). In this picture, the magnetic order in $BaFe_2As_2$ is then viewed as a competing phase with superconductivity similar to the formation of stripes in the cuprates. *Adapted with permission from Ref. [218].*

For research on the cuprates, one challenge would be to have one model system to be well characterized by different probes, since currently most scanning tunneling microscopy and ARPES studies have examined different compounds compared to those well characterized by neutron scattering. Combining neutron scattering and ARPES results, it was argued that spin fluctuations have sufficient strength to mediate superconductivity in $YBa_2Cu_3O_{6+x}$ [223]. Polarization dependence studies of magnetic excitations are also interesting to study anisotropies in spin space. Further, it has the potential to unveil broad magnetic features that are difficult to observe using unpolarized neutrons [205].

There are many systems that are not well studied by neutron scattering due to sample limitations, such as $Bi_2Sr_2Ca_{n-1}Cu_nO_{2n+4+\delta}$ (BSCCO), 1111 iron pnictides, and FeSe. When samples of the necessary size become available, it will be highly interesting to carry out neutron scattering experiments on these systems. In addition, newer systems such as $Ca_{10}(Pt_3As_8)(Fe_2As_2)_5$ and $Ca_{10}(Pt_4As_8)(Fe_2As_2)_5$ [224,225], $Ca_{1-x}(Pr,La)_xFeAs_2$ (112) [226,227] and $La_{0.4}Na_{0.6}Fe_2As_2$ [228] are also of great interest for neutron scattering. To understand the role of magnetism in high-temperature superconductors, neutron scattering plays and will continue to play a key role. To further the current understanding, new materials, combination of different probes, and theory will be important.

ACKNOWLEDGMENTS

We acknowledge help from X. Lu in preparing some of the figures. The materials synthesis and neutron scattering efforts on the hole-doped 122 and 111 family of materials are supported by the U.S. DOE, Office of Basic Energy Sciences, under Contract No. DE-SC0012311. The neutron scattering work on the electron-doped 122 family of materials is supported by U.S. NSF, DMR-1362219. The combination of RPA calculation and neutron scattering is supported by U.S. NSF, DMR-1436006 and DMR-1308603. Part of the materials synthesis at Rice University is supported by the Robert A. Welch Foundation Grants No. C-1839.

REFERENCES

[1] J.G. Bednorz, K.A. Müller, Z. Phys. B 64 (1986) 189.
[2] I.I. Mazin, Nature 464 (2010) 183.
[3] D. Vaknin, S.K. Sinha, D.E. Moncton, D.C. Johnston, J.M. Newsam, C.R. Safinya, et al., Phys. Rev. Lett. 58 (1987) 2802.
[4] M.K. Wu, J.R. Ashburn, C.J. Torng, P.H. Hor, R.L. Meng, L. Gao, et al., Phys. Rev. Lett. 58 (1987) 908.
[5] M.A. Kastner, R.J. Birgeneau, G. Shirane, Y. Endoh, Rev. Mod. Phys. 70 (1998) 897.
[6] R.J. Birgeneau, C. Stock, J.M. Tranquada, K. Yamada, J. Phys. Soc. Jpn. 75 (2006) 111003.
[7] J.M. Tranquada, in: J.R. Schrieffer, J.S. Brooks (Eds.), Handbook of High-Temperature Superconductivity, Springer, New York, 2007, pp. 257−298.
[8] M. Fujita, H. Hiraka, M. Matsuda, M. Matsuura, J.M. Tranquada, S. Wakimoto, et al., J. Phys. Soc. Jpn. 81 (2012) 011007.
[9] J.M. Tranquada, AIP Conf. Proc. 1550 (2013) 114.
[10] J.M. Tranquada, G. Xu, I.A. Zaliznyak, J. Magn. Magn. Mater. 350 (2014) 148.
[11] Y. Kamihara, T. Watanabe, M. Hirano, H. Hosono, J. Am. Chem. Soc. 130 (2008) 3296.
[12] P. Dai, J. Hu, E. Dagotto, Nat. Phys. 8 (2012) 709.
[13] M.D. Lumsden, A.D. Christianson, J. Phys. Condens. Matter. 22 (2010) 203203.
[14] P. Dai, Rev. Mod. Phys. 87 (2015) 855.
[15] M.-H. Fang, H.-D. Wang, C.-H. Dong, Z.-J. Li, C.-M. Feng, J. Chen, et al., Europhys. Lett. 94 (2011) 27009.
[16] E. Dagotto, Rev. Mod. Phys. 85 (2013) 849.
[17] F. Fernandez-Alonso, D.L. Price, in: F. Fernandez-Alonso, D.L. Price (Eds.), Neutron Scattering − Fundamentals, Experimental Methods in the Physical Sciences, vol. 44, Academic Press, Amsterdam, 2013, pp. 1−136.
[18] M.P.M. Dean, J. Magn, Magn. Mater. 376 (2015) 3.
[19] K.-J. Zhou, Y.-B. Huang, C. Monney, X. Dai, V.N. Strocov, N.-L. Wang, et al., Nat. Commun. 4 (2013) 1470.
[20] N.S. Headings, S.M. Hayden, R. Coldea, T.G. Perring, Phys. Rev. Lett. 105 (2010) 247001.
[21] Y.S. Lee, R.J. Birgeneau, M.A. Kastner, Y. Endoh, S. Wakimoto, K. Yamada, et al., Phys. Rev. B 60 (1999) 3643.
[22] R. Liang, D.A. Bonn, W.N. Hardy, Phys. Rev. B 73 (2006) 180505.
[23] P. Burlet, J.Y. Henry, L.P. Regnault, Phys. C (Amsterdam, Neth.) 296 (1998) 205.
[24] R. Coldea, S.M. Hayden, G. Aeppli, T.G. Perring, C.D. Frost, T.E. Mason, et al., Phys. Rev. Lett. 86 (2001) 5377.

[25] S.M. Hayden, G. Aeppli, T.G. Perring, H.A. Mook, F. Doğan, Phys. Rev. B 54 (1996) 6905.
[26] J. Lorenzana, G. Seibold, R. Coldea, Phys. Rev. B 72 (2005) 224511.
[27] A.C. Walters, T.G. Perring, J.-S. Caux, A.T. Savici, G.-D. Gu, C.-C. Lee, et al., Nat. Phys. 5 (2009) 867.
[28] S. Shamoto, M. Sato, J.M. Tranquada, B.J. Sternlieb, G. Shirane, Phys. Rev. B 48 (1993) 13817.
[29] Z. Xu, C. Stock, S. Chi, A.I. Kolesnikov, G. Xu, G. Gu, et al., Phys. Rev. Lett. 113 (2014) 177002.
[30] L.W. Harriger, M. Liu, H. Luo, R.A. Ewings, C.D. Frost, T.G. Perring, et al., Phys. Rev. B 86 (2012) 140403.
[31] W. Bao, G. Aeppli, J.W. Lynn, P.G. Pagliuso, J.L. Sarrao, M.F. Hundley, et al., Phys. Rev. B 65 (2002) 100505.
[32] T.P. Croft, C. Lester, M.S. Senn, A. Bombardi, S.M. Hayden, Phys. Rev. B 89 (2014) 224513.
[33] M. Fujita, K. Yamada, H. Hiraka, P.M. Gehring, S.H. Lee, S. Wakimoto, et al., Phys. Rev. B 65 (2002) 064505.
[34] E. Demler, S. Sachdev, Y. Zhang, Phys. Rev. Lett. 87 (2001) 067202.
[35] B. Khaykovich, S. Wakimoto, R.J. Birgeneau, M.A. Kastner, Y.S. Lee, P. Smeibidl, et al., Phys. Rev. B 71 (2005) 220508.
[36] J. Chang, Ch Niedermayer, R. Gilardi, N.B. Christensen, H.M. Rønnow, D.F. McMorrow, et al., Phys. Rev. B 78 (2008) 104525.
[37] M. Enoki, M. Fujita, T. Nishizaki, S. Iikubo, D.K. Singh, S. Chang, et al., Phys. Rev. Lett. 110 (2013) 017004.
[38] D. Haug, V. Hinkov, Y. Sidis, P. Bourges, N.B. Christensen, A. Ivanov, et al., New J. Phys. 12 (2010) 105006.
[39] M. Matsuda, G.E. Granroth, M. Fujita, K. Yamada, J.M. Tranquada, Phys. Rev. B 87 (2013) 054508.
[40] V. Hinkov, D. Haug, B. Fauqué, P. Bourges, Y. Sidis, A. Ivanov, et al., Science 319 (2008) 597.
[41] E. Fradkin, S.A. Kivelson, M.J. Lawler, J.P. Eisenstein, A.P. Mackenzie, Annu. Rev. Condens. Matter Phys. 1 (2010) 153.
[42] M. Matsuda, J.A. Fernandez-Baca, M. Fujita, K. Yamada, J.M. Tranquada, Phys. Rev. B 84 (2011) 104524.
[43] S.M. Hayden, H.A. Mook, P. Dai, T.G. Perring, F. Doğan, Nature 429 (2004) 531.
[44] J.M. Tranquada, H. Woo, T.G. Perring, H. Goka, G.D. Gu, G. Xu, et al., Nature 429 (2004) 534.
[45] G. Xu, G.D. Gu, M. Hücker, B. Fauqué, T.G. Perring, L.P. Regnault, et al., Nat. Phys. 5 (2009) 642.
[46] J. Chang, E. Blackburn, A.T. Holmes, N.B. Christensen, J. Larsen, J. Mesot, et al., Nat. Phys. 8 (2012) 871.
[47] G. Ghiringhelli, M. Le Tacon, M. Minola, S. Blanco-Canosa, C. Mazzoli, N.B. Brookes, et al., Science 337 (2012) 821.
[48] T. Wu, H. Mayaffre, S. Krämer, M. Horvatić, C. Berthier, W.N. Hardy, et al., Nature 477 (2011) 191.
[49] R. Comin, R. Sutarto, E.H. da Silva Neto, L. Chauviere, R. Liang, W.N. Hardy, et al., Science 347 (2015) 1335.
[50] M. Norman, Phys. Rev. B 63 (2001) 092509.
[51] T. Das, R.S. Markiewicz, A. Bansil, Phys. Rev. B 85 (2012) 064510.
[52] A.T. Boothroyd, P. Babkevich, D. Prabhakaran, P.G. Freeman, Nature 471 (2011) 341.

[53] Y. Drees, D. Lamago, A. Piovano, A.C. Komarek, Nat. Commun. 4 (2013) 2449.
[54] Y. Drees, Z.W. Li, A. Ricci, M. Rotter, W. Schmidt, D. Lamago, et al., Nat. Commun. 5 (2014) 5731.
[55] S. Wakimoto, K. Yamada, J.M. Tranquada, C.D. Frost, R.J. Birgeneau, H. Zhang, Phys. Rev. Lett. 98 (2007) 247003.
[56] C. Stock, R.A. Cowley, W.J.L. Buyers, C.D. Frost, J.W. Taylor, D. Peets, et al., Phys. Rev. B 82 (2010) 174505.
[57] S. Sugai, H. Suzuki, Y. Takayanagi, T. Hosokawa, N. Hayamizu, Phys. Rev. B 68 (2003) 184504.
[58] L.J.P. Ament, M. van Veenendaal, T.P. Devereaux, J.P. Hill, J. van den Brink, Rev. Mod. Phys. 83 (2011) 705.
[59] M.P.M. Dean, G. Dellea, R.S. Springell, F. Yakhou-Harris, K. Kummer, N.B. Brookes, et al., Nat. Mater. 12 (2013) 1019.
[60] M. Le Tacon, G. Ghiringhelli, J. Chaloupka, M. Moretti Sala, V. Hinkov, M.W. Haverkort, et al., Nat. Phys. 7 (2011) 725.
[61] M.P.M. Dean, R.S. Springell, C. Monney, K.J. Zhou, J. Pereiro, I. Božović, et al., Nat. Mater. 11 (2012) 850.
[62] J. Rossat-Mignod, L.P. Regnault, C. Vettier, P. Bourges, P. Burlet, J. Bossy, et al., Phys. C (Amsterdam, Neth.) 185−189 (1991) 86.
[63] T.E. Mason, A. Schröder, G. Aeppli, H.A. Mook, S.M. Hayden, Phys. Rev. Lett. 77 (1996) 1604.
[64] H.F. Fong, P. Bourges, Y. Sidis, L.P. Regnault, A. Ivanov, G.D. Gu, et al., Nature 398 (1999) 588.
[65] H. He, P. Bourges, Y. Sidis, C. Ulrich, L.P. Regnault, S. Pailhès, et al., Science 295 (2002) 1045.
[66] G. Yu, Y. Li, E.M. Motoyama, X. Zhao, N. Barišić, Y. Cho, et al., Phys. Rev. B 81 (2010) 064518.
[67] S.D. Wilson, P. Dai, S. Li, S. Chi, H.J. Kang, J.W. Lynn, Nature 442 (2006) 59.
[68] A.D. Christianson, E.A. Goremychkin, R. Osborn, S. Rosenkranz, M.D. Lumsden, C.D. Malliakas, et al., Nature 456 (2008) 930.
[69] N.K. Sato, N. Aso, K. Miyake, R. Shiina, P. Thalmeier, G. Varelogiannis, et al., Nature 410 (2001) 340.
[70] C. Stock, C. Broholm, J. Hudis, H.J. Kang, C. Petrovic, Phys. Rev. Lett. 100 (2008) 087001.
[71] O. Stockert, J. Arndt, E. Faulhaber, C. Geibel, H.S. Jeevan, S. Kirchner, et al., Nat. Phys. 7 (2011) 119.
[72] S. Li, P. Dai, Front. Phys. 6 (2011) 429.
[73] G. Yu, Y. Li, E.M. Motoyama, M. Greven, Nat. Phys. 5 (2009) 873.
[74] P. Dai, H.A. Mook, R.D. Hunt, F. Doğan, Phys. Rev. B 63 (2001) 054525.
[75] H. Woo, P. Dai, S.M. Hayden, H.A. Mook, T. Dahm, D.J. Scalapino, et al., Nat. Phys. 2 (2006) 600.
[76] M. Wang, C. Zhang, X. Lu, G. Tan, H. Luo, Y. Song, et al., Nat. Commun. 4 (2013) 2874.
[77] N.B. Christensen, D.F. McMorrow, H.M. Rønnow, B. Lake, S.M. Hayden, G. Aeppli, et al., Phys. Rev. Lett. 93 (2004) 147002.
[78] S. Pailhès, Y. Sidis, P. Bourges, V. Hinkov, A. Ivanov, C. Ulrich, et al., Phys. Rev. Lett. 93 (2004) 167001.
[79] L. Capogna, B. Fauqué, Y. Sidis, C. Ulrich, P. Bourges, S. Pailhès, et al., Phys. Rev. B 75 (2007) 060502.
[80] Y. Sidis, S. Pailhès, V. Hinkov, B. Fauqué, C. Ulrich, L. Capogna, et al., C. R. Phys. 8 (2007) 745.

[81] P. Dai, H.A. Mook, S.M. Hayden, G. Aeppli, T.G. Perring, R.D. Hunt, et al., Science 284 (1999) 1344.
[82] M. Eschrig, Adv. Phys. 55 (2006) 47.
[83] D.J. Scalapino, Rev. Mod. Phys. 84 (2012) 1383.
[84] V. Hinkov, P. Bourges, S. Pailhès, Y. Sidis, A. Ivanov, C.D. Frost, et al., Nat. Phys. 3 (2007) 780.
[85] D.K. Morr, D. Pines, Phys. Rev. B 61 (2000) 6483.
[86] P.B. Allen, V.N. Kostur, N. Takesue, G. Shirane, Phys. Rev. B 56 (1997) 5552.
[87] M.K. Chan, C.J. Dorow, L. Mangin-Thro, Y. Tang, Y. Ge, M.J. Veit et al., http://arxiv.org/abs/1402.4517 (last accessed 20.07.15).
[88] C. de la Cruz, Q. Huang, J.W. Lynn, J. Li, W. Ratcliff II, J.L. Zarestky, et al., Nature 453 (2008) 899.
[89] D.N. Basov, R.D. Averitt, D. van der Marel, M. Dressel, K. Haule, Rev. Mod. Phys. 83 (2011) 471.
[90] Q. Si, E. Abrahams, Phys. Rev. Lett. 101 (2008) 076401.
[91] R.M. Fernandes, A.V. Chubukov, J. Schmalian, Nat. Phys. 10 (2014) 97.
[92] W. Bao, Y. Qiu, Q. Huang, M.A. Green, P. Zajdel, M.R. Fitzsimmons, et al., Phys. Rev. Lett. 102 (2009) 247001.
[93] W. Bao, Q. Huang, G. Chen, M.A. Green, D. Wang, J. He, et al., Chin. Phys. Lett. 28 (2011) 086104.
[94] D.C. Johnston, Adv. Phys. 59 (2010) 803.
[95] P.C. Canfield, S.L. Bud'ko, Annu. Rev. Condens. Matt. Phys. 1 (2010) 27.
[96] T.-K. Chen, C.-C. Chang, H.-H. Chang, A.-H. Fang, C.-H. Wang, W.-H. Chao, et al., Proc. Natl. Acad. Sci. U.S.A. 111 (2014) 63.
[97] M.G. Kim, R.M. Fernandes, A. Kreyssig, J.W. Kim, A. Thaler, S.L. Bud'ko, et al., Phys. Rev. B 83 (2011) 134522.
[98] Y. Song, S.V. Carr, X. Lu, C. Zhang, Z.C. Sims, N.F. Luttrell, et al., Phys. Rev. B 87 (2013) 184511.
[99] E.E. Rodriguez, C. Stock, P. Zajdel, K.L. Krycka, C.F. Majkrzak, P. Zavalij, et al., Phys. Rev. B 84 (2011) 064403.
[100] M.-C. Ding, H.-Q. Lin, Y.-Z. Zhang, Phys. Rev. B 87 (2013) 125129.
[101] W. Ratcliff II, P.A. Kienzle, J.W. Lynn, S. Li, P. Dai, G.F. Chen, et al., Phys. Rev. B 81 (2010) 140502.
[102] Z.P. Yin, K. Haule, G. Kotlair, Nat. Mater 10 (2011) 932.
[103] J.L. Niedziela, M.A. McGuire, T. Egami, Phys. Rev. B 86 (2012) 174113.
[104] C. Lester, J.-H. Chu, J.G. Analytis, T.G. Perring, I.R. Fisher, S.M. Hayden, Phys. Rev. B 81 (2010) 064505.
[105] J.T. Park, G. Friemel, T. Loew, V. Hinkov, Y. Li, B.H. Min, et al., Phys. Rev. B 86 (2012) 024437.
[106] Y. Song, L.P. Regnault, C. Zhang, G. Tan, S.V. Carr, S. Chi, et al., Phys. Rev. B 88 (2013) 134512.
[107] M. Ramazanoglu, J. Lamsal, G.S. Tucker, J.-Q. Yan, S. Calder, T. Guidi, et al., Phys. Rev. B 87 (2013) 140509.
[108] L.W. Harriger, H.Q. Luo, M.S. Liu, C. Frost, J.P. Hu, M.R. Norman, et al., Phys. Rev. B 84 (2011) 054544.
[109] C. Zhang, L.W. Harriger, Z. Yin, W. Lv, M. Wang, G. Tan, et al., Phys. Rev. Lett. 112 (2014) 217202.
[110] J. Zhao, D.T. Adroja, D.-X. Yao, R. Bewley, S. Li, X.F. Wang, et al., Nat. Phys. 5 (2009) 555.

[111] R.A. Ewings, T.G. Perring, J. Gillett, S.D. Das, S.E. Sebastian, A.E. Taylor, et al., Phys. Rev. B 83 (2011) 214519.
[112] E. Kaneshita, T. Tohyama, Phys. Rev. B 82 (2010) 094441.
[113] A.L. Wysocki, K.D. Delashchenko, V.P. Antropov, Nat. Phys. 7 (2011) 485.
[114] D. Stanek, O. Sushkov, G.S. Uhrig, Phys. Rev. B 84 (2011) 064505.
[115] R. Yu, Z. Wang, P. Goswami, A.H. Nevidomskyy, Q. Si, E. Abrahams, Phys. Rev. B 86 (2012) 085148.
[116] M. Liu, L.W. Harriger, H. Luo, M. Wang, R.A. Ewings, T. Guidi, et al., Nat. Phys. 8 (2012) 376.
[117] J.H. Soh, G.S. Tucker, D.K. Pratt, D.L. Abernathy, M.B. Stone, S. Ran, et al., Phys. Rev. Lett. 111 (2013) 227002.
[118] Y. Furukawa, B. Roy, S. Ran, S.L. Bud'ko, P.C. Canfield, Phys. Rev. B 89 (2014) 121109.
[119] S. Mandal, R.E. Cohen, K. Haule, Phys. Rev. B 90 (2014) 060501.
[120] O.J. Lipscombe, G.F. Chen, C. Fang, T.G. Perring, D.L. Abernathy, A.D. Christianson, et al., Phys. Rev. Lett. 106 (2011) 057004.
[121] I.A. Zaliznyak, Z. Xu, J.M. Tranquada, G. Gu, A.M. Tsvelik, M.B. Stone, Phys. Rev. Lett. 107 (2011) 216403.
[122] C. Stock, E.E. Rodriguez, M.A. Green, P. Zavalij, J.A. Rodriguez-Rivera, Phys. Rev. B 84 (2011) 045124.
[123] C. Stock, E.E. Rodriguez, O. Sobolev, J.A. Rodriguez-Rivera, R.A. Ewings, J.W. Taylor, et al., Phys. Rev. B 90 (2014) 121113.
[124] D. Parshall, G. Chen, L. Pintschovius, D. Lamago, Th Wolf, L. Radzihovsky, et al., Phys. Rev. B 85 (2012) 140515.
[125] D.K. Pratt, M.G. Kim, A. Kreyssig, Y.B. Lee, G.S. Tucker, A. Thaler, et al., Phys. Rev. Lett. 106 (2011) 257001.
[126] H. Luo, R. Zhang, M. Laver, Z. Yamani, M. Wang, X. Lu, et al., Phys. Rev. Lett. 108 (2012) 247002.
[127] B. Farago, J. Major, F. Mezei, Neutron optics and spin labeling methods, in: Felix Fernandez-Alonso, David L. Price (Eds.), Neutron Scattering - Magnetic and Quantum Phenomena, in: Thomas Lucatorto, Albert C. Parr, Kenneth Baldwin (Eds.), Experimental Methods in the Physical Sciences, vol. 48, Elsevier, Amsterdam, 2015, pp. 1−42.
[128] A.P. Dioguardi, J. Crocker, A.C. Shockley, C.H. Lin, K.R. Shirer, D.M. Nisson, et al., Phys. Rev. Lett. 111 (2013) 207201.
[129] X. Lu, D.W. Tam, C. Zhang, H. Luo, M. Wang, R. Zhang, et al., Phys. Rev. B 90 (2014) 024509.
[130] D.K. Pratt, W. Tian, A. Kreyssig, J.L. Zarestky, S. Nandi, N. Ni, et al., Phys. Rev. Lett. 103 (2009) 087001.
[131] X. Lu, H. Gretarsson, R. Zhang, X. Liu, H. Luo, W. Tian, et al., Phys. Rev. Lett. 110 (2013) 257001.
[132] M. Wang, H. Luo, M. Wang, S. Chi, J.A. Rodriguez-Rivera, D. Singh, et al., Phys. Rev. B 83 (2011) 094516.
[133] M.G. Kim, J. Lamsal, T.W. Heitmann, G.S. Tucker, D.K. Pratt, S.N. Khan, et al., Phys. Rev. Lett. 109 (2012) 167003.
[134] S. Nandi, M.G. Kim, A. Kreyssig, R.M. Fernandes, D.K. Pratt, A. Thaler, et al., Phys. Rev. Lett. 104 (2010) 057006.
[135] S. Avci, O. Chmaissem, J.M. Allred, S. Rosenkranz, I. Eremin, A.V. Chubukov, et al., Nat. Commun. 5 (2014) 3845.

[136] K. Marty, A.D. Christianson, C.H. Wang, M. Matsuda, H. Cao, L.H. VanBebber, et al., Phys. Rev. B 83 (2011) 060509.
[137] M.G. Kim, A. Kreyssig, A. Thaler, D.K. Pratt, W. Tian, J.L. Zarestky, et al., Phys. Rev. B 82 (2010) 220503.
[138] D.S. Inosov, G. Friemel, J.T. Park, A.C. Walters, Y. Texier, Y. Laplace, et al., Phys. Rev. B 87 (2013) 224425.
[139] G.S. Tucker, D.K. Pratt, M.G. Kim, S. Ran, A. Thaler, G.E. Granroth, et al., Phys. Rev. B 86 (2012) 020503.
[140] S. Haravifard, B. Gaulin, Z. Yamani, Quantum phase transitions, in: Felix Fernandez-Alonso, David L. Price (Eds.), Neutron Scattering - Magnetic and Quantum Phenomena, in: Thomas Lucatorto, Albert C. Parr, Kenneth Baldwin (Eds.), Experimental Methods in the Physical Sciences, vol. 48, Elsevier, Amsterdam, 2015, pp. 43−144.
[141] T. Shibauchi, A. Carrington, Y. Matsuda, Annu. Rev. Condens. Matter Phys. 5 (2014) 113.
[142] D. Hu, X. Lu, W. Zhang, H. Luo, S. Li, P. Wang, et al., Phys. Rev. Lett. 114 (2015) 157002.
[143] M. Hiraishi, S. Iimura, K.M. Kojima, J. Yamaura, H. Hiraka, K. Ikeda, et al., Nat. Phys. 10 (2014) 300.
[144] L.W. Harriger, A. Schneidewind, S. Li, J. Zhao, Z. Li, W. Lu, et al., Phys. Rev. Lett. 103 (2009) 087005.
[145] H. Luo, Z. Yamani, Y. Chen, X. Lu, M. Wang, S. Li, et al., Phys. Rev. B 86 (2012) 024508.
[146] C. Zhang, M. Wang, H. Luo, M. Wang, M. Liu, J. Zhao, et al., Sci. Rep. 1 (2011) 115.
[147] J.T. Park, D.S. Inosov, A. Yaresko, S. Graser, D.L. Sun, Ph. Bourges, et al., Phys. Rev. B 82 (2010) 134503.
[148] J.-P. Castellan, S. Rosenkranz, E.A. Goremychkin, D.Y. Chung, I.S. Todorov, M.G. Kanatzidis, et al., Phys. Rev. Lett. 107 (2011) 177003.
[149] C.H. Lee, K. Kihou, H. Kawano-Furukawa, T. Saito, A. Iyo, H. Eisaki, et al., Phys. Rev. Lett. 106 (2011) 067003.
[150] W. Jayasekara, Y. Lee, A. Pandey, G.S. Tucker, A. Sapkota, J. Lamsal, et al., Phys. Rev. Lett. 111 (2013) 157001.
[151] H.A. Mook, M.D. Lumsden, A.D. Christianson, S.E. Nagler, B.C. Sales, R. Jin, et al., Phys. Rev. Lett. 104 (2010) 187002.
[152] Y. Qiu, W. Bao, Y. Zhao, C. Broholm, V. Stanev, Z. Tesanovic, et al., Phys. Rev. Lett. 103 (2009) 067008.
[153] S. Chi, J.A. Rodriguez-Rivera, J.W. Lynn, C. Zhang, D. Phelan, D.K. Singh, et al., Phys. Rev. B 84 (2011) 214407.
[154] T.J. Liu, J. Hu, B. Qian, D. Fobes, Z.Q. Mao, W. Bao, et al., Nat. Mater 9 (2010) 716.
[155] Z. Xu, J. Wen, G. Xu, Q. Jie, Z. Lin, Q. Li, et al., Phys. Rev. B 82 (2010) 104525.
[156] M.D. Lumsden, A.D. Christianson, E.A. Goremychkin, S.E. Nagler, H.A. Mook, M.B. Stone, et al., Nat. Phys. 6 (2010) 182.
[157] A.D. Christianson, M.D. Lumsden, K. Marty, C.H. Wang, S. Calder, D.L. Abernathy, et al., Phys. Rev. B 87 (2013) 224410.
[158] A. Subedi, L. Zhang, D.J. Singh, M.H. Du, Phys. Rev. B 78 (2008) 134514.
[159] J. Wen, S. Li, Z. Xu, C. Zhang, M. Matsuda, O. Sobolev, et al., Phys. Rev. B 88 (2013) 144509.
[160] M. Wang, M. Wang, H. Miao, S.V. Carr, D.L. Abernathy, M.B. Stone, et al., Phys. Rev. B 86 (2012) 144511.
[161] N. Qureshi, P. Steffens, Y. Drees, A.C. Komarek, D. Lamago, Y. Sidis, et al., Phys. Rev. Lett. 108 (2012) 117001.

[162] S.V. Borisenko, V.B. Zabolotnyy, D.V. Evtushinsky, T.K. Kim, I.V. Morozov, A.N. Yaresko, et al., Phys. Rev. Lett. 105 (2010) 067002.
[163] N. Qureshi, P. Steffens, D. Lamago, Y. Sidis, O. Sobolev, R.A. Ewings, et al., Phys. Rev. B 90 (2014) 144503.
[164] H. Luo, X. Lu, R. Zhang, M. Wang, E.A. Goremychkin, D.T. Adroja, et al., Phys. Rev. B 88 (2013) 144516.
[165] A.D. Christianson, M.D. Lumsden, S.E. Nagler, G.J. MacDougall, M.A. McGuire, A.S. Sefat, et al., Phys. Rev. Lett. 103 (2009) 087002.
[166] S. Chi, A. Schneidewind, J. Zhao, L.W. Harriger, L. Li, Y. Luo, et al., Phys. Rev. Lett. 102 (2009) 107006.
[167] J. Zhao, C.R. Rotundu, K. Marty, M. Matsuda, Y. Zhao, C. Setty, et al., Phys. Rev. Lett. 110 (2013) 147003.
[168] C.H. Lee, P. Steffens, N. Qureshi, M. Nakajima, K. Kihou, A. Iyo, et al., Phys. Rev. Lett. 111 (2013) 167002.
[169] C. Zhang, H.-F. Li, Y. Song, Y. Su, G. Tan, T. Netherton, et al., Phys. Rev. B 88 (2013) 064504.
[170] C. Zhang, R. Yu, Y. Su, Y. Song, M. Wang, G. Tan, et al., Phys. Rev. Lett. 111 (2013) 207002.
[171] D.K. Pratt, A. Kreyssig, S. Nandi, N. Ni, A. Thaler, M.D. Lumsden, et al., Phys. Rev. B 81 (2010) 140510.
[172] M.G. Kim, G.S. Tucker, D.K. Pratt, S. Ran, A. Thaler, A.D. Christianson, et al., Phys. Rev. Lett. 110 (2013) 177002.
[173] M. Wang, H. Luo, J. Zhao, C. Zhang, M. Wang, K. Marty, et al., Phys. Rev. B 81 (2010) 174524.
[174] D.S. Inosov, J.T. Park, A. Charnukha, Y. Li, A.V. Boris, B. Keimer, et al., Phys. Rev. B 83 (2011) 214520.
[175] M.D. Lumsden, A.D. Christianson, D. Parshall, M.B. Stone, S.E. Nagler, G.J. MacDougall, et al., Phys. Rev. Lett. 102 (2009) 107005.
[176] S. Onari, H. Kontani, M. Sato Phys, Rev. B 81 (2010) 060504.
[177] S. Onari, H. Kontani, Phys. Rev. B 84 (2011) 144518.
[178] Q.Q. Ge, Z.R. Ye, M. Xu, Y. Zhang, J. Jiang, B.P. Xie, et al., Phys. Rev. X 3 (2013) 011020.
[179] W. Lv, A. Moreo, E. Dagotto, Phys. Rev. B 89 (2014) 104510.
[180] D.N. Argyiou, A. Hiess, A. Akbari, I. Eremin, M.M. Korshunov, J. Hu, et al., Phys. Rev. B 81 (2010) 220503.
[181] J. Guo, S. Jin, G. Wang, S. Wang, K. Zhu, T. Zhou, et al., Phys. Rev. B 82 (2010) 180520.
[182] A. Ricci, N. Poccia, G. Campi, B. Joseph, G. Arrighetti, L. Barba, et al., Phys. Rev. B 84 (2011) 060511.
[183] R.H. Yuan, T. Dong, Y.J. Song, P. Zheng, G.F. Chen, J.P. Hu, et al., Sci. Rep. 2 (2012) 221.
[184] F. Chen, M. Xu, Q.Q. Ge, Y. Zhang, Z.R. Ye, L.X. Yang, et al., Phys. Rev. X 1 (2011) 021020.
[185] W. Li, H. Ding, Z. Li, P. Deng, K. Chang, K. He, et al., Phys. Rev. Lett. 109 (2012) 057003.
[186] W. Li, H. Ding, P. Deng, K. Chang, C. Song, K. He, et al., Nat. Phys. 8 (2012) 126.
[187] J. Zhao, H. Cao, E. Bourret-Courchesne, D.-H. Lee, R.J. Birgeneau, Phys. Rev. Lett. 109 (2012) 267003.
[188] S.V. Carr, D. Louca, J. Siewenie, Q. Huang, A. Wang, X. Chen, et al., Phys. Rev. B 89 (2014) 134509.
[189] M. Wang, M. Wang, G.N. Li, Q. Huang, C.H. Li, G.T. Tan, et al., Phys. Rev. B 84 (2011) 094504.

[190] F. Ye, S. Chi, W. Bao, X.F. Wang, J.J. Ying, X.H. Chen, et al., Phys. Rev. Lett. 107 (2011) 137003.
[191] M. Wang, W. Tian, P. Valdivia, S. Chi, E. Bourret-Courchesne, P. Dai, et al., Phys. Rev. B 90 (2014) 125148.
[192] M. Wang, C. Fang, D.-X. Yao, G. Tan, L.W. Harriger, Y. Song, et al., Nat. Commun. 2 (2011) 580.
[193] S. Chi, F. Ye, W. Bao, M. Fang, H.D. Wang, C.H. Dong, et al., Phys. Rev. B 87 (2013) 100501.
[194] Y. Xiao, S. Nandi, Y. Su, S. Price, H.-F. Li, Z. Fu, et al., Phys. Rev. B 87 (2013) 140408.
[195] M. Wang, X. Lu, R.A. Ewings, L.W. Harriger, Y. Song, S.V. Carr, et al., Phys. Rev. B 87 (2013) 064409.
[196] J. Zhao, Y. Shen, R.J. Birgeneau, M. Gao, Z.-Y. Lu, D.-H. Lee, et al., Phys. Rev. Lett. 112 (2014) 177002.
[197] J.T. Park, G. Friemel, Y. Li, J.-H. Kim, V. Tsurkan, J. Deisenhofer, et al., Phys. Rev. Lett. 107 (2011) 177005.
[198] G. Friemel, J.T. Park, T.A. Maier, V. Tsurkan, Y. Li, J. Deisenhofer, et al., Phys. Rev. B 85 (2012) 140511.
[199] G. Friemel, W.P. Liu, E.A. Goremychkin, Y. Li, J.T. Park, O. Sobolev, et al., Europhys. Lett. 99 (2012) 67004.
[200] M. Wang, C. Li, D.L. Abernathy, Y. Song, S.V. Carr, X. Lu, et al., Phys. Rev. B 86 (2012) 024502.
[201] A.E. Taylor, R.A. Ewings, T.G. Perring, J.S. White, P. Babkevich, A. Krzton-Maziopa, et al., Phys. Rev. B 86 (2012) 094528.
[202] C. Zhang, Y. Song, L.-P. Regnault, Y. Su, M. Enderle, J. Kulda, et al., Phys. Rev. B 90 (2014) 140502.
[203] H. Luo, M. Wang, C. Zhang, X. Lu, L.-P. Regnault, R. Zhang, et al., Phys. Rev. Lett. 111 (2013) 107006.
[204] C. Wang, R. Zhang, F. Wang, H. Luo, L.P. Regnault, P. Dai, et al., Phys. Rev. X 3 (2013) 041036.
[205] N.S. Headings, S.M. Hayden, J. Kulda, N. Hari Babu, D.A. Cardwell, Phys. Rev. B 84 (2011) 104513.
[206] N. Qureshi, P. Steffens, S. Wurmehl, S. Aswartham, B. Büchner, M. Braden, Phys. Rev. B 86 (2012) 060410.
[207] O.J. Lipscombe, L.W. Harriger, P.G. Freeman, M. Enderle, C. Zhang, M. Wang, et al., Phys. Rev. B 82 (2010) 064515.
[208] P. Steffens, C.H. Lee, N. Qureshi, K. Kihou, A. Iyo, H. Eisaki, et al., Phys. Rev. Lett. 110 (2013) 137001.
[209] M. Liu, C. Lester, J. Kulda, X. Lu, H. Luo, M. Wang, et al., Phys. Rev. B 85 (2012) 214516.
[210] C. Zhang, M. Liu, Y. Su, L.-P. Regnault, M. Wang, G. Tan, et al., Phys. Rev. B 87 (2013) 081101.
[211] N. Qureshi, C.H. Lee, K. Kihou, K. Schmalzl, P. Steffens, M. Braden, Phys. Rev. B 90 (2014) 100502.
[212] P. Babkevich, B. Roessli, S.N. Gvasaliya, L.-P. Regnault, P.G. Freeman, E. Pomjakushina, et al., Phys. Rev. B 83 (2011) 180506.
[213] K. Prokeš, A. Hiess, W. Bao, E. Wheeler, S. Landsgesell, D.N. Argyriou, Phys. Rev. B 86 (2012) 064503.
[214] C. Dhital, Z. Yamani, W. Tian, J. Zeretsky, A.S. Sefat, Z. Wang, et al., Phys. Rev. Lett. 108 (2012) 087001.

[215] C. Dhital, T. Hogan, Z. Yamani, R.J. Birgeneau, W. Tian, M. Matsuda, et al., Phys. Rev. B 89 (2014) 214404.
[216] X. Lu, J.T. Park, R. Zhang, H. Luo, A.H. Nevidomskyy, Q. Si, et al., Science 345 (2014) 657.
[217] Q. Zhang, R.M. Fernandes, J. Lamsal, J. Yan, S. Chi, G.S. Tucker, et al., Phys. Rev. Lett. 114 (2015) 057001.
[218] L. de' Medici, G. Giovannetti, M. Capone, Phys. Rev. Lett. 112 (2014) 177001.
[219] H. Ishida, A. Liebsch, Phys. Rev. B 81 (2010) 054513.
[220] T. Misawa, K. Nakamura, M. Imada, Phys. Rev. Lett. 108 (2012) 177007.
[221] M. Nakajima, S. Ishida, T. Tanaka, K. Kihou, Y. Tomioka, C.-H. Lee, et al., J. Phys. Soc. Jpn. 83 (2014) 104703.
[222] F. Hardy, A.E. Böhmer, D. Aoki, P. Burger, T. Wolf, P. Schweiss, et al., Phys. Rev. Lett. 111 (2013) 027002.
[223] T. Dahm, V. Hinkov, S.V. Borisenko, A.A. Kordyuk, V.B. Zabolotnyy, J. Fink, et al., Nat. Phys. 5 (2009) 217.
[224] N. Ni, J.M. Allred, B.C. Chan, R.J. Cava, Proc. Natl. Acad. Sci. U.S.A. 108 (2011) 1019.
[225] S. Kakiya, K. Kudo, Y. Nishikubo, K. Oku, E. Nishibori, H. Sawa, et al., J. Phys. Soc. Jpn. 80 (2011) 093704.
[226] H. Yakita, H. Ogino, T. Okada, A. Yamamoto, K. Kishio, T. Tohei, et al., J. Am. Chem. Soc. 136 (2014) 846.
[227] N. Katayama, K. Kudo, S. Onari, T. Mizukami, K. Sugawara, Y. Sugiyama, et al., J. Phys. Soc. Jpn. 82 (2013) 123702.
[228] J.-Q. Yan, S. Nandi, B. Saparov, P. Čermák, Y. Xiao, Y. Su, et al., Phys. Rev. B 91 (2015) 024501.
[229] N. Katayama, S. Ji, D. Louca, S. Lee, M. Fujita, T.J. Sato, et al., J. Phys. Soc. Jpn. 79 (2010) 113702.
[230] M.G. Kim, D.K. Pratt, G.E. Rustan, W. Tian, J.L. Zarestky, A. Thaler, et al., Phys. Rev. B 83 (2011) 054514.

This page intentionally left blank